Master's thesis

Development of Multi-Pixel Photon Counters and readout electronics

Makoto Taguchi

High Energy Group, Department of Physics,
Graduate School of Science, Kyoto University

February 9, 2007

Abstract

The T2K experiment is a next generation long baseline neutrino oscillation experiment which will start in April 2009. The main goals in the first phase of T2K are the discovery of ν_e appearance and an accurate measurement of ν_μ disappearance. Before neutrinos have a chance to oscillate, the flux and energy spectrum are measured in the near detectors. The scintillators read out by wave length shifting fibers will be used in almost all near detectors. The photosensor which detects the light from the fiber must be compact, low-cost, insensitive to magnetic field and have high photon detection efficiency. Multi-Pixel Photon Counter (MPPC) is a new photodetector produced by Hamamatsu Photonics. It consists of many small avalanche photodiode (APD) pixels which work in Geiger mode. The output from MPPC is summation of the output charge from all APD pixels. MPPC has advantages that match the T2K requirements and is chosen as the photosensor for the T2K near detector. We show the study of MPPC and the readout electronics.

At first we show measurements of the basic performance of latest MPPC samples. At 20°C the gain of $\sim 10^6$ is achieved with the noise rate less than 500 kHz at the 0.5 photo-electron threshold. The photon detection efficiency for green light is two to three times larger than that of a photomultiplier tube. The cross-talk rate is typically 20% and less than 40%. The nonlinearity is about 20% at the 40 (120) injected photoelectrons for a 100 (400) pixel device, respectively. The recovery time is found to be less than 100 ns. The basic performance of MPPC satisfies the requirements for the T2K near detector. We have also checked the response of each micro pixel using a laser injection system. The uniformity within one pixel is found to be $2 \sim 3\%$. The pixel-to-pixel uniformity is also $2 \sim 3\%$. The response of MPPC has a temperature dependence, but we demonstrate that it can be corrected within 3% level by two independent correction methods even if temperature changes by 5°C.

In T2K it is necessary to develop the compact and multi-channel readout electronics in order to handle the large number of readout channels. Moreover the establishment of the test system for mass production of MPPC is also needed. For these purposes we have developed the readout electronics of MPPC using the Trip-t chip produced at Fermilab. Trip-t is an ASIC (Application Specified Integrated Circuit) and has 32 input channels. There are three kinds of outputs for Trip-t; a discriminated digital signal for each input and serialized analog signals corresponding to the amplitude and timing of the injected charge. With the test board that has four inputs, we have observed clearly separated photopeaks of MPPC. We have shown that Trip-t can be used for the readout of MPPC in T2K. Our study will play an important role not only for the T2K experiment but also for wider use of MPPC.

Contents

Chapter 1

INTRODUCTION

The T2K experiment is a next generation long baseline neutrino oscillation experiment which will start in 2009. We need the photosensors which are compact, low-cost, insensitive to magnetic field and have high photon detection efficiency for the near detectors of T2K. Multi-Pixel Photon Counter (MPPC) is a new photodetector manufactured by Hamamatsu Photonics and chosen as the photosensor that match the requirements for the T2K near detectors. However MPPC has not been used yet in a real experiment and it is necessary to check if the performance of MPPC really satisfies the requirements for T2K . For this purpose, we have studied the basic characteristics of MPPC at first.

In T2K it is necessary to develop the readout electronics of MPPC in order to handle the large number ($\sim$ 60,000) of readout channels. Moreover the establishment of the test system for mass production of MPPC is also needed. For these purposes we have developed the readout electronics of MPPC with "Trip-t" chip.

The contents of this thesis are summarized as the following;

- Chapter 2 : T2K experiment

  We briefly explain the overview of T2K in this chapter.

- Chapter 3 $\sim$ 6 : MPPC

  In this part we give an introduction of MPPC (Chapter 3) and report the various measurements of MPPC (Chapter 4 $\sim$ 6).

- Chapter 7 $\sim$ 8 : Readout electronics of MPPC

  In this part the development of the readout electronics of MPPC with the Trip-t chip is reported. We explain Trip-t and show the basic performance of Trip-t in Chapter 7. We show the tests of MPPC with Trip-t in Chapter 8.

- Chapter 9 : Conclusion

  This thesis is concluded in Chapter 9.

Chapter 2

T2K EXPERIMENT

2.1 Neutrino oscillation

Neutrino oscillations arise quite naturally in a model in which the weak eigenstates of the neutrinos ν_l are mixtures of the mass eigenstates ν_i;

$$|\nu_l\rangle = \sum U_{li}|\nu_i\rangle \tag{2.1}$$

The matrix U_{li} is the Maki-Nakagawa-Sakata (MNS) mixing matrix. It is analogous to the Cabibbo-Kobayashi-Masukawa (CKM) matrix which mixes the weak and strong eigenstates of the quarks. The MNS matrix can be written as:

$$U_{ij} = \begin{pmatrix} 1 & 0 & 0 \\ 0 & c_{23} & s_{23} \\ 0 & -s_{23} & c_{23} \end{pmatrix} \begin{pmatrix} c_{13} & 0 & e^{i\delta} \\ 0 & 1 & 0 \\ -e^{-i\delta} & 0 & c_{13} \end{pmatrix} \begin{pmatrix} c_{12} & s_{12} & 0 \\ -s_{12} & c_{12} & 0 \\ 0 & 0 & 1 \end{pmatrix}, \tag{2.2}$$

where $c_{ij} \equiv \cos\theta_{ij}$, $s_{ij} \equiv \sin\theta_{ij}$ with the angles θ_{ij} parameterizing the three possible rotations between the neutrino states and δ is CP violation phase. Pure ν_l are emitted in weak interaction, but ν_i states propagate independently during the flight. If the masses of ν_i are different, they will build up a relative phase difference and neutrino changes the flavor during the flight. We call this phenomenon neutrino oscillation. For the simplest case, where only two of the mass states dominate the oscillation, the survival probability of ν_l is written as;

$$P(\nu_l \to \nu_l) = 1 - \sin^2 2\theta \sin^2\left(\frac{1.27\Delta m^2(\mathrm{eV}^2)L_\nu(\mathrm{km})}{E_\nu(\mathrm{GeV})}\right), \tag{2.3}$$

where θ is the mixing angle of two flavors, L_ν is the flight length, E_ν is the energy of the neutrino and Δm^2 is the mass square difference between two ν_i states. Up to now $\nu_\mu \to \nu_\tau$ oscillation is confirmed by the observation of atmospheric neutrinos [1], the K2K experiment [2] and the MINOS experiment [3] with accelerator neutrinos. The oscillation parameters are $\Delta m^2_{23} = (1.9 \sim 3.0) \times 10^{-3}$ eV^2

and $\sin^2\theta_{23} > 0.9$ with 90% confidence level. $\nu_e \to \nu_x$ ($\nu_e \to \nu_\mu$ and $\nu_e \to \nu_\tau$) oscillation is also confirmed by the observation of solar neutrinos, performed by the SK experiment [4], the SNO experiment [5], and the KamLAND experiment [6] with reactor anti-neutrinos. The oscillation parameters are $\Delta m^2_{12} = (7.4 \sim 8.5) \times 10^{-5}$ eV^2 and $0.33 < \tan^2\theta_{12} < 0.50$ with 90% confidence level. Thus the rotation angles θ_{23} and θ_{12} are measured, but θ_{13} not yet. The strongest constraint of θ_{13} comes from the Chooz reactor $\bar{\nu_e}$ oscillation experiment [7]. The upper limit of $\sin^2 2\theta_{13}$ is 0.1 with 90% confidence level. Therefore the measurement of θ_{13}, which means the discovery of ν_e appearance, is one of the most important issues for future neutrino physics.

2.2 T2K experiment

2.2.1 Introduction

The T2K experiment [8] is a next generation long-baseline neutrino oscillation experiment to study nature of neutrinos. An artificial neutrino beam generated in the J-PARC (Fig. 2.1) 50 GeV high intensity proton synchrotron in Tokai (Ibaraki) is shot toward the 50 kton water Cherenkov detector, Super-Kamiokande, located about 1000 m underground in Kamioka mine (Gifu) and 295 km away from Tokai. The overview of the T2K experiment is shown in Fig. 2.2. The first phase of the T2K experiment is aimed at two main goals - the discovery of $\nu_\mu \to \nu_e$ oscillation with more than an order of magnitude better sensitivity than any previous experiment and an accurate determination of the parameters θ_{23} and Δm^2_{23}.

2.2.2 Neutrino beam line

An overview of the neutrino beam line in T2K is shown in Fig. 2.3. The design intensity of the proton beam is 3.3×10^{14} protons per spill[1] with a repetition rate of 0.3 Hz. The fast extracted beam width is 4.2 μsec and there are 8 bunches in a spill. The bunch length and spacing are each 58 ns and 598 ns. The extracted proton beam hits a target to generate pions. This production target is a graphite cylinder. Three electro-magnetic horns are used to focus the charged pions to the forward direction. The target is put inside of the inner conductor of the first horn to collect and focus as many pions as possible. These horns are driven by a pulsed current of 320 kA synchronized with the beam. The focused pions decay to neutrinos in a 110 m decay tunnel which follows the horns. The decay tunnel is filled with 1 atm Helium gas to reduce pion absorption and tritium production.

[1] The beam obtained by one extraction.

Figure 2.1: Overview of the J-PARC (Japan Proton Accelerator Research Complex) facility. J-PARC consists of the 400 MeV linear accelerator, the 3 GeV proton synchrotron, and the 50 GeV proton synchrotron. It aims to pursue a frontier of science in particle physics, nuclear physics, material physics, life science and nuclear technology.

Figure 2.2: Overview of the T2K experiment. An artificial neutrino beam generated in the J-PARC 50 GeV proton synchrotron in Tokai is shot toward the Super-Kamiokande which is 295 km away from Tokai.

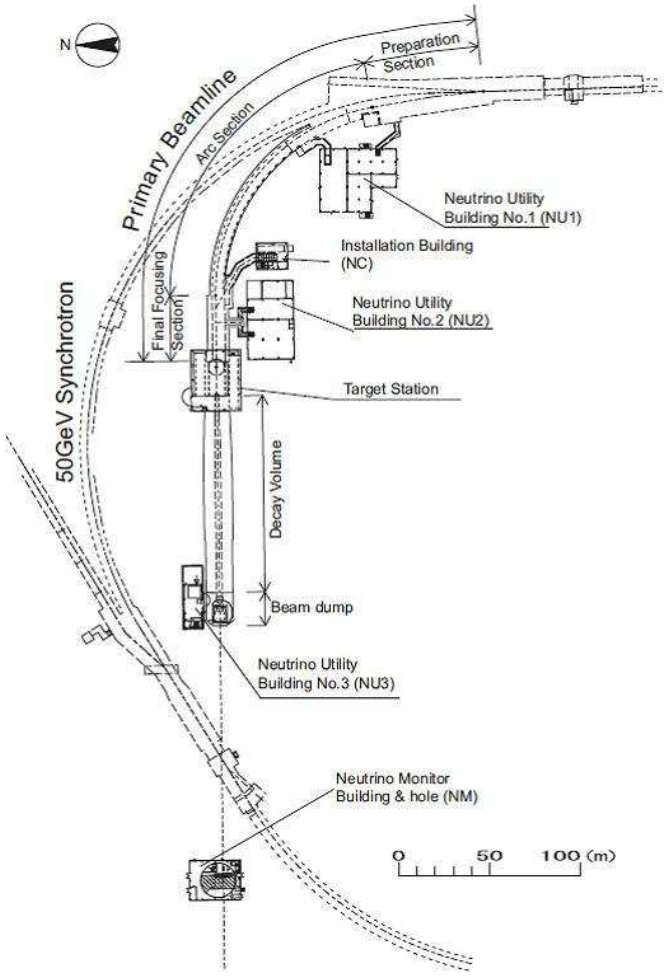

Figure 2.3: Overview of the T2K neutrino beamline. The extracted proton beam from the proton synchrotron hits a graphite target. Three electro-magnetic horns are used to focus the charged pions to the forward direction.

2.2.3 Off-axis beam

A key element of the design of T2K is the off-axis neutrino beam which is directed to the different direction to Super-Kamiokande. The concept of the off-axis beam is illustrated in Fig. 2.4. With a finite decay angle, neutrino energy becomes almost independent of parent pion momentum as a characteristics of the Lorentz boost, which provides the narrow energy spectrum. By selecting the off-axis angle of $2.0° \sim 3.0°$, this narrow peak can be at the energy where the oscillation probability is maximum at Super-Kamiokande. There are two major advantages over a conventional on-axis beam. First, the neutrino flux of an off-axis beam at the oscillation maximum is higher than that of an on-axis beam. Second, there are less high-energy neutrinos which do not contribute to a ν_e appearance signal but produce the background mainly through neutral current π^0 production.

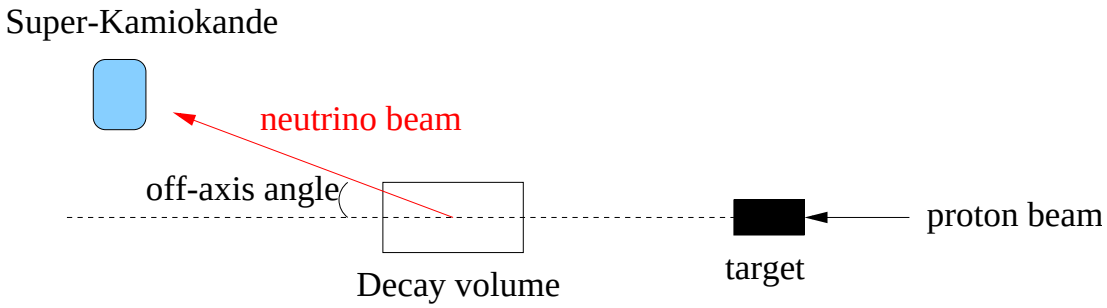

Figure 2.4: Illustration of the concept of the off-axis beam. The neutrino beam is directed to the different direction from that to Super-Kamiokande.

2.2.4 Neutrino monitors

In the T2K experiment, there are two detector systems designed specially for neutrino beam monitoring; One is a muon monitor (MUMON) and another is an on-axis neutrino detector (INGrid). MUMON will be placed downstream of the beam dump and will monitor the intensity, profile and direction of the beam by detecting high energy muons coming through the beam dump. The baseline design of MUMON is a combination of segmented ionization chambers and an array of diamond detectors, as shown in Fig 2.5 [9]. INGrid will monitor the neutrino beam directly with neutrinos. It is sensitive to the neutrinos of the whole energy range, though MUMON is only sensitive to the high energy neutrinos. The INGrid detector is designed to consist of 7 + 7 units which are arranged to form a cross and two diagonal units [10]. For INGrid, the target of neutrino interaction is an iron, and scintillators are used to detect the muon from an interaction. The overview of INGrid is shown in Fig. 2.6.

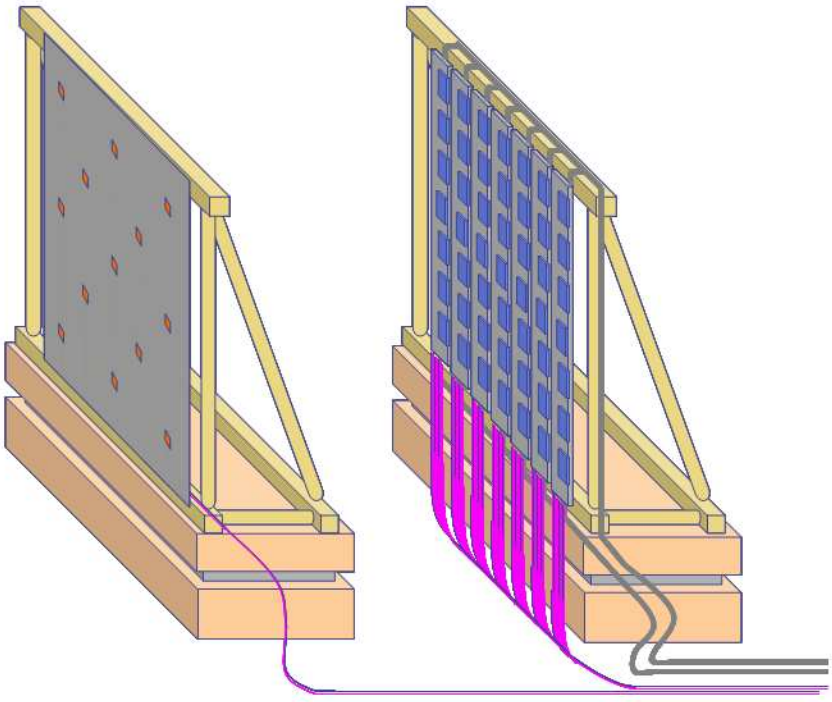

Figure 2.5: A current design of MUMON. The left is an array of diamond detectors and the right are segmented ionization chambers.

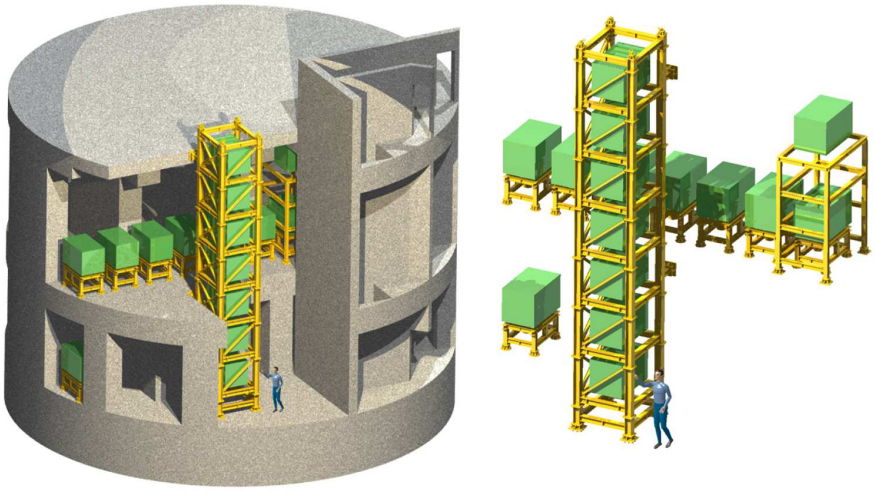

Figure 2.6: Arrangement of the INGrid detector. This detector is designed to consist of 7 + 7 units which are arranged to form a cross and two diagonal units.

2.2.5 Off-axis near detectors

The near detector complex at 280 m from the target (ND280) shown in Fig. 2.7 contains a fine resolution magnetized detector designed to measure the energy spectrum, flux, flavor content, and interaction cross-sections of neutrinos before the neutrinos have a chance to oscillate. This detector sits off-axis in the neutrino beam along a line between the target and the Super-Kamiokande detector, at 280 m from the target. The ND280 detector consists of the following elements illustrated in Fig. 2.8.

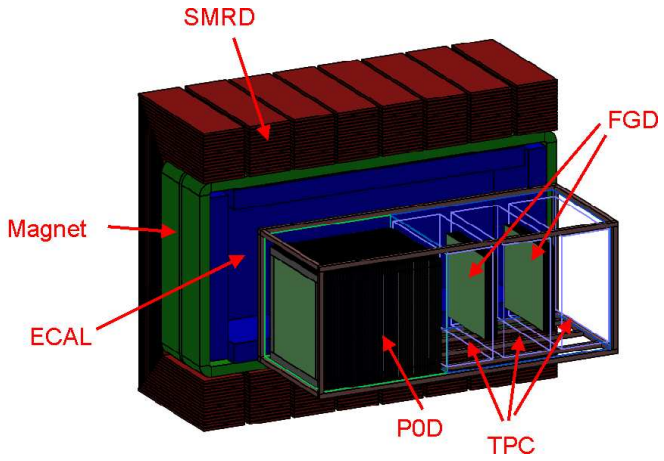

Figure 2.7: Cutaway view of the T2K 280 m near detector. This detector consists of a magnet, Pi-Zero detector (P0D), Fine Grained Detector (FGD), Time Projection Chamber (TPC), Electromagnetic CALorimeter (ECAL) and Side Muon Range Detector (SMRD). A neutrino beam comes from the left.

- Magnet: ND280 uses the magnet built at CERN (European Organization for Nuclear Research) for the UA1 experiment[2]. This will be operated with the magnetic field of 0.2 T to measure the momenta of penetrating charged particles produced by neutrino interactions in the near detector.

- Pi-Zero Detector (P0D): P0D sits at the upstream end of ND280, and is optimized for measuring the rate of neutral current π^0 production. P0D consists of tracking planes composed of scintillating bars alternating with lead foils. The interactive layers of passive water in sections of P0D provide a water target for measuring interactions on oxygen.

- Tracker: Downstream of P0D is a tracking detector optimized for measuring the momenta of charged particles, particularly muons and pions produced

[2]The UA1 experiment was ran at CERN from 1981 until 1993 on the SPS collider. The W and Z bosons were discovered by this experiment.

by charged current interactions. The tracker consists of two detector technologies, Fine Grained Detector (FGD) and Time Projection Chambers (TPC). There are two FGDs for ND280. One FGD consists of layers of segmented scintillator bars and another one consists of layers of segmented scintillator bars alternating with layers of passive water. Each FGD is put between two TPC modules.

- Electromagnetic CALorimeter (ECAL): An electromagnetic calorimeter surrounds P0D and the tracker. ECAL is a segmented Pb-scintillator sandwich detector whose main purpose is to measure γ rays from interactions in the tracker and P0D. The γ rays do not convert in the inner detectors and are critical for the reconstruction of π^0 decays, which is the dominant background for ν_e appearance.

- Side Muon Range Detector (SMRD): Plastic scintillators are instrumented in the air gaps in the sides of the magnet to measure the ranges of muons that exit the sides of ND280. SMRD also can provide a veto for events entering the detector from the outside and a trigger for cosmic-ray muons.

2.2.6 Far detector

The far detector of the T2K experiment is Super-Kamiokande, 50,000 tons water Cherenkov detector which is located about 1,000 m underground of Kamioka Mine near the village of Higashi-Mozumi, Gifu. The detector is a cylindrical shape with the diameter of 39 m and the height of 41 m as shown in Fig. 2.9. The detector is optically separated into two parts, the inner detector (ID) and the outer detector (OD). The size of ID is 36.2 m in height and 33.8 m in diameter. The 11,146 inward-facing 20 inch photomultiplier tubes (PMT) are attached on the wall of ID and the 1,885 outward-facing 8 inch PMTs are attached on the wall of OD. OD is used to identify the cosmic-ray muons which enter from the out of the detector and the particles which exit from the detector.

2.2.7 Photosensors for the near detectors

As we have seen in Subsection 2.2.5, we plan to use scintillators in almost all detectors in ND280 for the detection of neutrinos. The blue light from each scintillator is absorbed by a wave length shifting fiber inserted to the scintillator and the re-emitted green light from the fiber is transported to the photosensor put outside the detector. There are following requirements to the photosensors;

1. Compact size, low cost

2. Insensitive to magnetic field

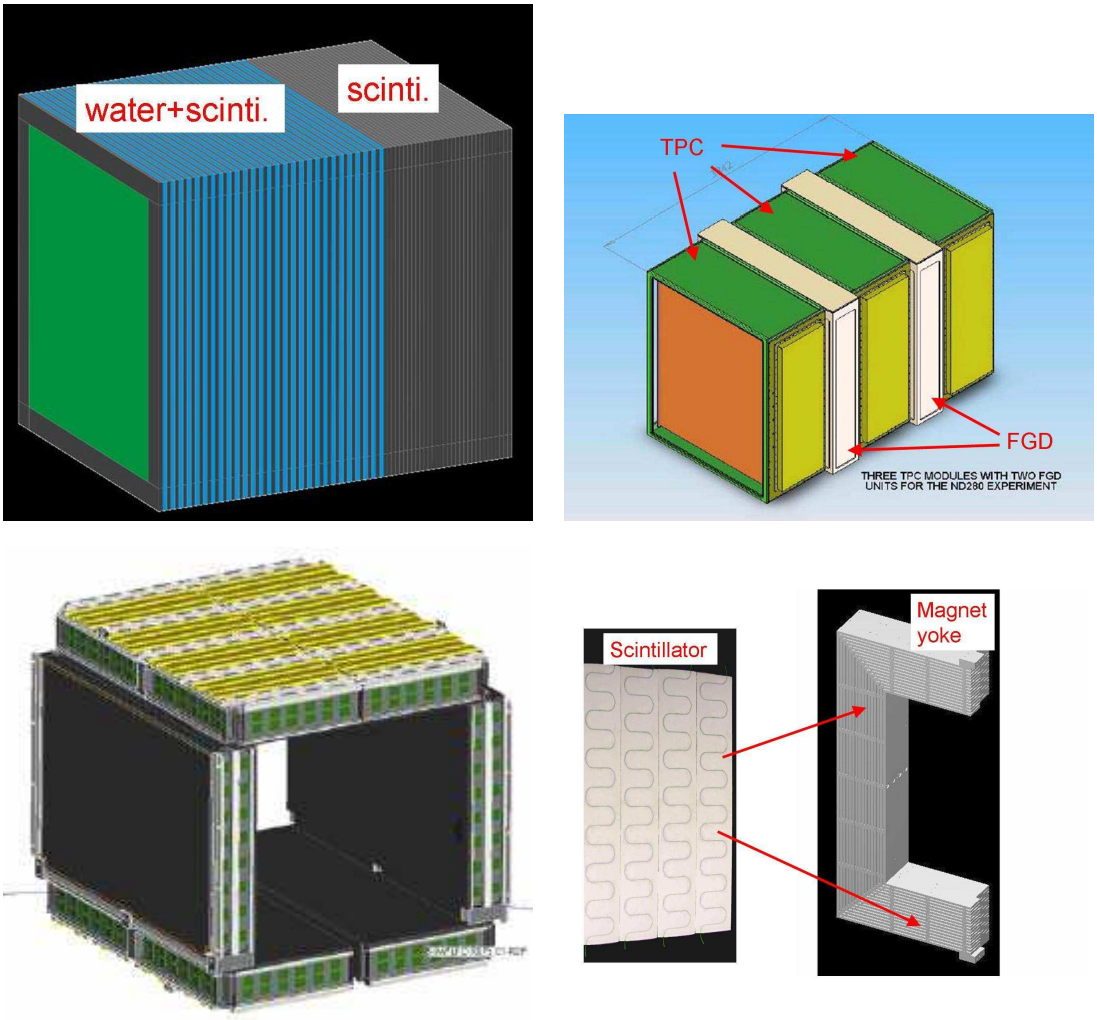

Figure 2.8: Components of ND280, which are P0D (upper left), tracker (upper right), ECAL (lower left) and SMRD (lower right). P0D consists of tracking planes composed of scintillating bars alternating with lead foils. The tracker consists of three Time Projection Chambers (TPC) and two Fine Grained Detectors (FGD). ECAL is a segmented Pb-scintillator sandwich detector. SMRD consists of plastic scintillators which are placed in the air gaps in the sides of the magnet.

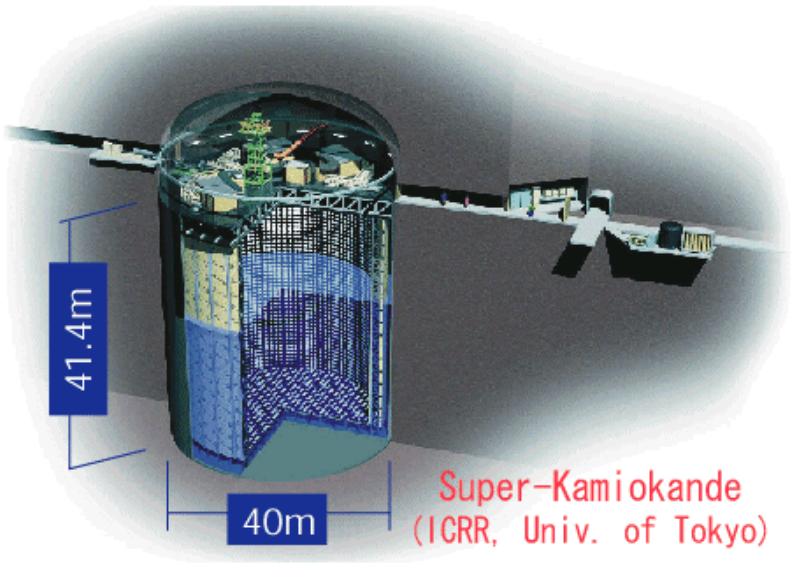

Figure 2.9: Overview of Super-Kamiokande. The tank with the diameter of 39 m and the height of 41 m is filled with 50,000 tons pure water. The 11,146 inward-facing 8 inch photomultiplier tubes (PMT) are attached on the wall of the inner detector.

3. Large light yield (at least as large as that of a photomultiplier tube)

The first requirement comes from that the number of total readout channels is $\sim$ 60,000 and the space for the photosensors is limited, the second one that ND280 is placed under the 0.2 T magnetic field, and third one that large light yield will increase the efficiency for the detection of particles. From the second requirement a general photomultiplier tube cannot be used and MPPC is chosen as the baseline photosensor for ND280. However MPPC is a device under development and has never been used in any real experiment. Therefore it is important to check if the performance of MPPC satisfies to the requirements for ND280. For this purpose we show the study of the basic performance of MPPC after an introduction of this device from the next chapter.

Chapter 3

MULTI-PIXEL PHOTON COUNTERS (MPPC)

3.1 Introduction

Multi-Pixel Photon Counter (MPPC[1]) is a new photodetector manufactured by Hamamatsu Photonics (HPK), Japan. It consists of many small avalanche photodiodes (APD) in an area of typically 1mm^2. Figure 3.1 shows a photograph of MPPC and Figure 3.2 shows a close-up view of an active area inside the package. Figure 3.3 shows the structure of APD pixels for latest MPPC samples, taken by a microscope. One can see that the APD pixels are arranged in order. The size of each pixel is 100 $\times$ 100 μm for the left figure and 50 $\times$ 50 μm for the right one. We explain the operational principle of MPPC in the following section.

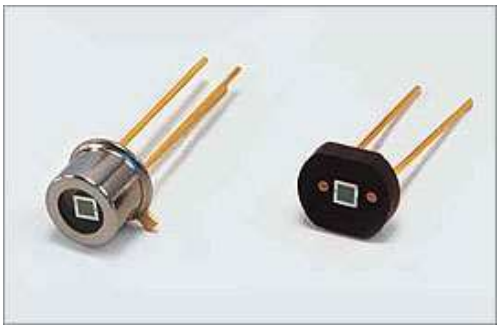

Figure 3.1: Photograph of MPPC.

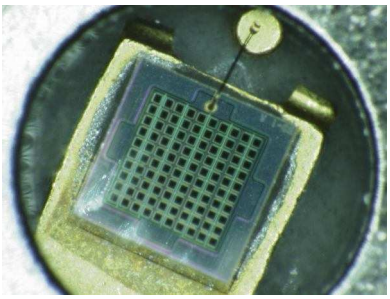

Figure 3.2: Close-up view of an active area inside the package.

[1]MPPC is a trademark of Hamamatsu Photonics. It is one of the products of Si-PM (Silicon Photomultiplier) family which was originally developed in Russia.

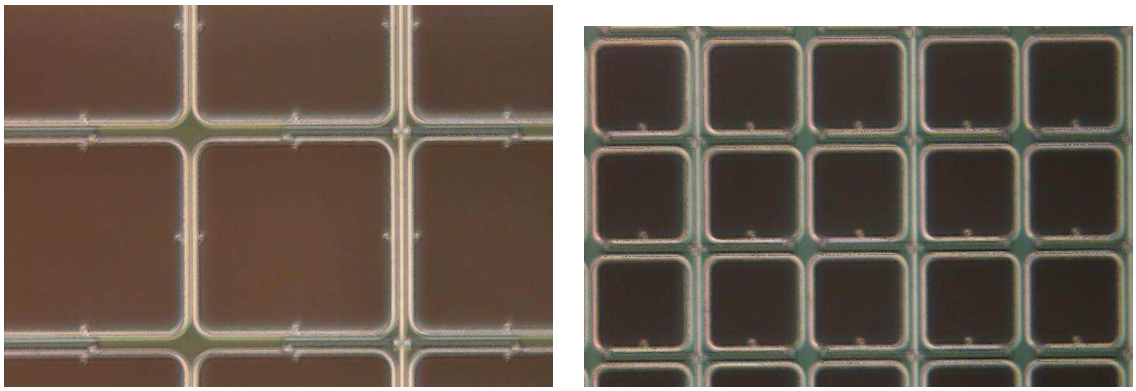

Figure 3.3: Structure of APD pixels for latest MPPC samples. The left (right) figure is for a 100 (400) pixel device and the size of each pixel is 100 × 100 (50 × 50) μm, respectively.

3.2 Operational principle of MPPC

At first we explain the principle of APD which is a component of MPPC. APD is a semiconductor photodetector. In a semiconductor photodetector the formation of a pn-junction creates a special zone, called absorption region, in the interface between the p-type and n-type materials. This is illustrated in Fig. 3.4. Because of the difference in the concentration of electrons and holes between the two materials, there is an initial diffusion of holes towards the n-region and a diffusion of electrons towards the p-region. As a consequence, the diffusing electrons fill up the holes in the p-region while the diffusing holes capture the electrons in the n-region. Since the p-region is injected with extra electrons, it becomes negative while the n-region becomes positive. This creates an electric field across the pn-junction. Because of this electric field, there is a potential difference across the junction. The region of changing potential is called as an absorption region. The incoming photon into the absorption region will create electron-hole pairs which are swept out by the electric field. The current signal corresponding to the movement of the electron-hole pairs is proportional to the number of incoming photons to the semiconductor detector. In general, however, the intrinsic electric field is not intense enough to provide efficient charge collection. In order to obtain good charge collection, we usually apply a reverse bias voltage to the junction. By applying a reverse bias voltage, the absorption region spreads to the whole detector. In an avalanche photodiode a high reverse voltage (100 $\sim$ 200 V) is applied and the multiplication region which has a high electric field is created in the absorption region. The schematic of the structure of APD is shown in Fig. 3.5. The created electron-hole pairs in the absorption region drift by the electric field and cause an "avalanche" multiplication during the drift. The drift length is an order of $\sim$ 100 μm and the movement of the electron-hole pairs is independent

of magnetic field. There are two operational modes in APD;

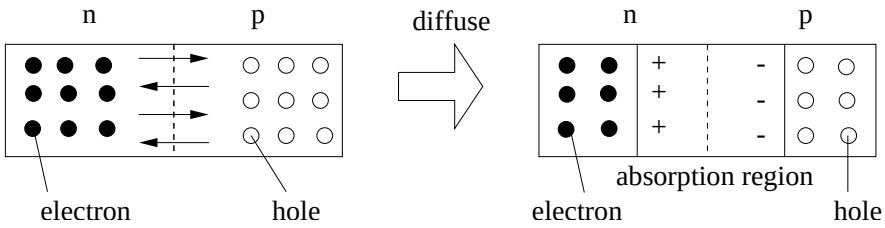

Figure 3.4: Schematic diagram of a pn-junction. Because of an initial diffusion of holes towards the n-region and a diffusion of electrons towards the p-region, an electric field is created across the pn-junction.

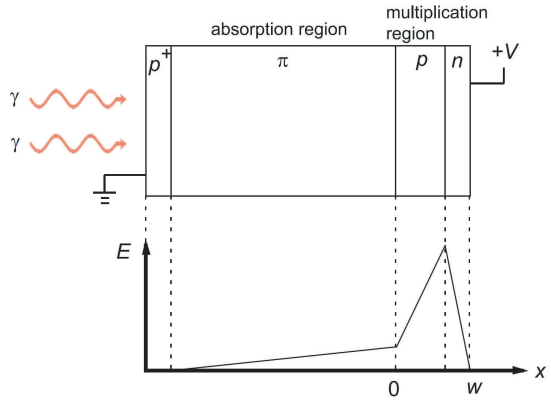

Figure 3.5: Schematic of the structure of an avalanche photodiode. The multiplication region which has a high electric field is created in the absorption region due to a high reverse voltage.

- Normal mode
  - Detector operates below the breakdown voltage (V_{bd}).
  - Avalanche gain is typically $\lesssim$ 100.
  - Detector has linear output charge to the number of injected photons.
- Geiger mode
  - Detector operates above the breakdown voltage (V_{bd}).
  - Avalanche gain is typically $\sim 10^6$.
  - Detector does not have linear output charge to the number of injected photons.

In MPPC, each avalanche photodiode independently works in the Geiger mode with applied voltage of a few volts above the breakdown voltage (V_{bd}). The output charge Q from a single pixel is independent of the number of produced photoelectrons within the pixel, and can be written as

$$\mathrm{Q} = \mathrm{C}(\mathrm{V} - V_{bd}), \tag{3.1}$$

where V is the applied voltage and C is the capacitance of the pixel. The typical value of C is several hundreds fC and the typical value of (V$-V_{bd}$) is one volt. Therefore Q is several hundreds fC and the gain of MPPC, which is defined as Q divided by the charge of an electron, becomes about 10^6. As the Geiger multiplication develops, the generated charge within a pixel causes a voltage drop to an externally attached silicon resistor and the effective voltage applied to the photodiode decreases. The Geiger multiplication stops when the effective voltage is below the breakdown voltage. The time that all the generated charge take to go through the resistor is expressed as C $\times$ R, where R is the resistance of the resistor. This time approximately corresponds to signal width.

Next we explain the operational principle of MPPC. The readout line of MPPC is common to all APD pixels and the output from MPPC is summation of the output charge from all APD pixels. If the response of each pixel is well uniform, the total charge from MPPC is quantized to multiples of Q and proportional to the number of pixels fired by a Geiger discharge as shown in Eq. 3.2.

$$Q_{total} = N_{fired} \times \mathrm{Q}, \tag{3.2}$$

where Q_{total} is the output charge of MPPC and N_{fired} is the number of fired pixels. The number of fired pixels is proportional to the number of injected photons if the number of photons is small compared to the total number of pixels. Thus, MPPC has an excellent photon counting capability.

As explained above, MPPC is an attractive device that achieves a high gain with a linear response to the number of injected photons by arranging many Geiger-mode APD pixels in a small 1 mm $\times$ 1 mm region.

3.3 Application of MPPC

Because MPPC is a new photodetector recently developed, it has not been used yet actually. However in high energy physics MPPC is one of the promising devices as the replacement of general photomultiplier tubes (PMT) [11]. Table 3.1 shows the characteristics of MPPC compared to that of PMT. MPPC has the following advantages;

1. Gain : The MPPC gain is $\sim 10^6$ and comparable to that of a PMT because of the Geiger multiplication.

2. Applied voltage : The applied voltage of MPPC is less than 100 V and it is easy to handle a device.

3. Magnetic field : MPPC is insensitive to magnetic field because of the characteristics of a semiconductor.

4. Photon detection efficiency : Quantum Efficiency (QE) of an avalanche photodiode is typically 70%, but there is an inactive region within one pixel of MPPC. The fraction of the active area to the total area of one pixel is typically 50 $\sim$ 70%. Including the geometrical fraction and a Geiger probability, the photon detection efficiency of MPPC is 30 $\sim$ 45%. This is two to three higher than that of a PMT.

The detailed characteristics of MPPC is shown in Chapter 4.

One of the disadvantages of MPPC is the small size of the device. However HPK is now working to produce a more larger device (3×3 or 5×5 mm^2). MPPC is going to be used in the T2K experiment and the ILC (International Linear Collider) experiment[12] in high energy physics. Moreover the use of MPPC in the medical region such as PET (Positron Emission Tomography) will be possible [13]. Especially MPPC is used in the T2K experiment which will start in April 2009 "at first in the world".

	MPPC	PMT
Gain	$10^5 \sim 10^6$	$10^6 \sim 10^7$
Applied voltage	60 $\sim$ 70 V	1000 $\sim$ 2000 V
Active area	1 mm $\times$ 1 mm	$\sim$ 10 cm
Magnetic field	insensitive	sensitive
photon detection efficiency	30 $\sim$ 45 %	$\sim$ 15 %

Table 3.1: Comparison of characteristics of MPPC to that of PMT.

3.4 History of MPPC samples

We have developed MPPC with Hamamatsu Photonics since 2005. Table 3.2 shows the history of MPPC samples. In Chapter 4 and 8 we show the result with the T2K-100U-m type and the T2K-11-050C type (the latest samples). In Chapter 5 and 6 we show the result with the 311-53-1A type and the 311-32-1A type.

Version	Serial number (100 pixel)	Serial number (400 pixel)	Time
1	21-53-1A	1-32-21	Apr. 2005
2	311-53-1A	311-32-1A	Jan. 2006
3	T2K-11-100C	T2K-11-050C	Oct. 2006
4	T2K-100U-m	–	Oct. 2006

Table 3.2: History of MPPC samples.

3.5 Measurement of MPPC

The measurement of MPPC is described in Chapter 4, 5 and 6. The contents of these chapters are summarized below;

- Chapter 4 : Basic performance

  In this chapter we show measurements of basic performance of MPPC. At last we compare the measured basic performance of MPPC to the requirements for T2K.

- Chapter 5 : Laser scan

  In this chapter we show the test with a laser injection system. With this test we check the response of each micro pixel in MPPC.

- Chapter 6 : Correction of MPPC signal

  In this chapter we show the correction methods of MPPC signal using cosmic-ray muons. Finally we evaluate the correction precision and check if it satisfies the T2K requirement.

Chapter 4

BASIC PERFORMANCE OF MPPC

In this chapter we report the basic performance of MPPC.

4.1 Test samples

The main characteristics of the test samples are summarized in Table 4.1. These are the latest samples provided in Oct. 2006. The device-by-device variation of three 400 pixel devices is also tested. We have not measured the device-by-device variation of the latest 100 pixel devices, but have shown the device-by-device variation of the old 100 pixel samples in Appendix B.

Serial number	Number of pixels	Pitch (μm)	Operating voltage (V)	Signal width (ns)
T2K-100U-m	100	100	70 V	40
T2K-11-050C	400	50	70 V	10

Table 4.1: Summary of the test samples.

4.2 Test items

The following is the list of the test items.

- Raw signal $\cdots$ Section 4.3
- Gain $\cdots$ Section 4.4
- Noise rate $\cdots$ Section 4.5

- Photon detection efficiency (PDE) $\cdots$ Section 4.6
- Cross-talk rate $\cdots$ Section 4.7
- Linearity $\cdots$ Section 4.8
- Recovery time $\cdots$ Section 4.9

The temperature and voltage dependence of gain, noise rate, cross-talk rate, and PDE are measured. Here we define the temperature coefficient of each basic parameter as the following.

$$\frac{dP}{dT} = \frac{2}{P(V,T_1)+P(V,T_2)}\frac{P(V,T_1)-P(V,T_2)}{T_1-T_2}, \tag{4.1}$$

where dP/dT is the temperature coefficient of a basic parameter P and P(V,$T_{1(2)}$) is the value of P at the applied voltage of V and the temperature of $T_{1(2)}$, respectively. We take T_1 to be 20°C and T_2 to be 25°C. We evaluate the temperature coefficient at the applied voltage of 69.4 V (70.0V) for a 100 (400) pixel device, respectively.

We also define the voltage coefficient of each basic parameter as the following.

$$\frac{dP}{dV} = \frac{2}{P(V_i,T)+P(V_{i+1},T)}\frac{P(V_{i+1},T)-P(V_i,T)}{V_{i+1}-V_i}, \tag{4.2}$$

where dP/dV is the voltage coefficient of a basic parameter P and P($V_{i(i+1)}$,T) is the value of P at the applied voltage of $V_{i(i+1)}$ and the temperature of T. We evaluate the voltage coefficient at the applied voltage of 69.4 V (70.0 V) for a 100 (400) pixel device and the temperature of 20°C.

The device-by-device variation of three 400 pixel devices is defined as the following equation;

$$\text{variation} = (P_{max}-P_{min})\frac{3}{P_1+P_2+P_3}, \tag{4.3}$$

where P_1, P_2, and P_3 are the basic parameters of each device and $P_{max(min)}$ is the maximum (minimum) value of a basic parameter P among three devices.

The instruments for the measurements of the basic performance are summarized below;

- Blue LED: NICHIA NSPB500S

  The range of emission wavelength is 450∼480 nm in FWHM, as shown in Fig. 4.1.

- CAMAC 12-bit Charge Sensitive ADC C009

  The dynamic range is $0 \sim -1200$ pC.

- Bias voltage supply : YOKOGAWA GS610

  The maximum output voltage is 110 V and the maximum output current is 3.2 A. The voltage resolution is 0.0001 V.

- Temperature chamber: ETAC HIFLEX FL211C

  The temperature range is $-20°\text{C} \sim +100$ °C and the temperature resolution is 0.1°C.

- Amplifier : REPIC RPN-090

  The gain of one channel is 10 with ±2% precision. We use two channels in order to obtain the gain of 100.

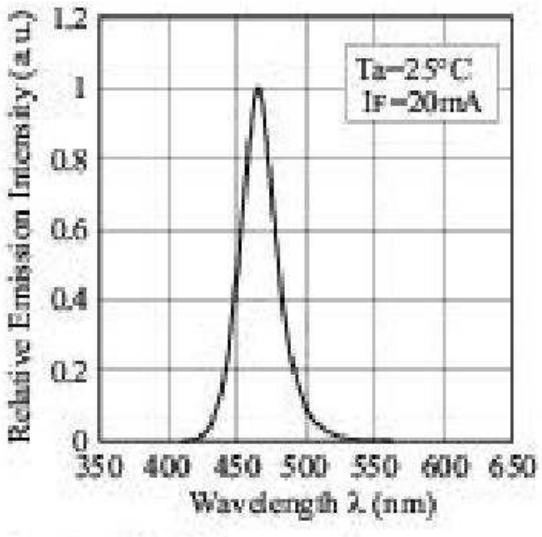

Figure 4.1: Emission spectrum of the blue LED, NICHIA NSPB500S.

4.3 Raw signal

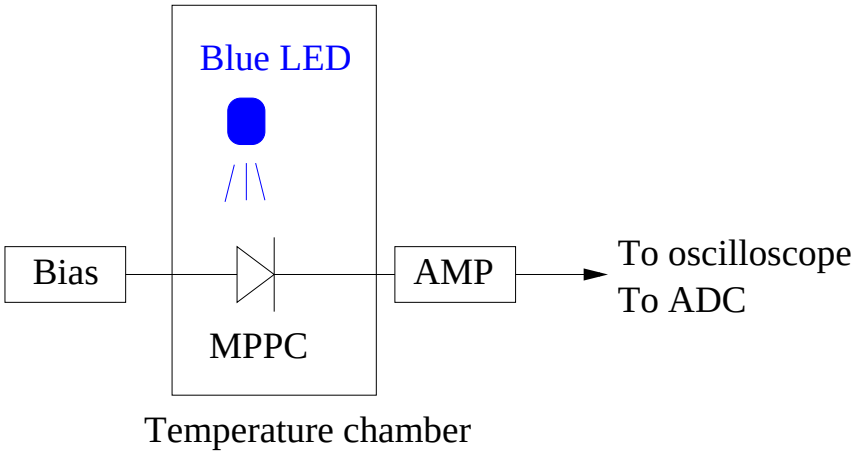

Figure 4.2: Setup for the observation of raw signal of MPPC. MPPC is illuminated by pulsed light from a blue LED and the output from MPPC is amplified by a factor of 100 with an amplifier.

The setup for the observation of raw signal of MPPC is shown in Fig. 4.2. MPPC is illuminated by pulsed light from a blue LED at low intensity and the output from MPPC is amplified by a factor of 100 with an amplifier. Figure 4.3 and 4.4 show the raw signals of 100 and 400 pixel devices taken with an oscilloscope and output charge read out by an analog-to-digital converter (ADC). The responses for multiple triggers are overlaid in Fig. 4.3. One can see excellently separated signals corresponding to one, two, and three fired pixels. This is because that the response of each pixel is well uniform. These observations demonstrate the excellent photon counting capability of MPPC.

4.4 Gain

The gain is measured by illuminating MPPC with light from a blue LED. From the value of ADC counts between the pedestal and the 1 photo-electron (p.e.) peaks, we calculate the charge of a single fired pixel, Q. The gain is defined as Q divided by the charge of an electron. Figure 4.5 shows the measured gain of 100 (left) and 400 (right) pixel devices as a function of the applied voltage. The measurement is performed inside a temperature-controlled chamber and the data at 15, 20, and 25°C are shown.

At 20°C the measured gain is $1.0 \times 10^6 \sim 3.0 \times 10^6$ for the 100 pixel device and $6.0 \times 10^5 \sim 1.2 \times 10^6$ for the 400 pixel device. The gain linearly depends on the applied voltage as expected from Eq. 3.1. MPPC operates in the Geiger mode

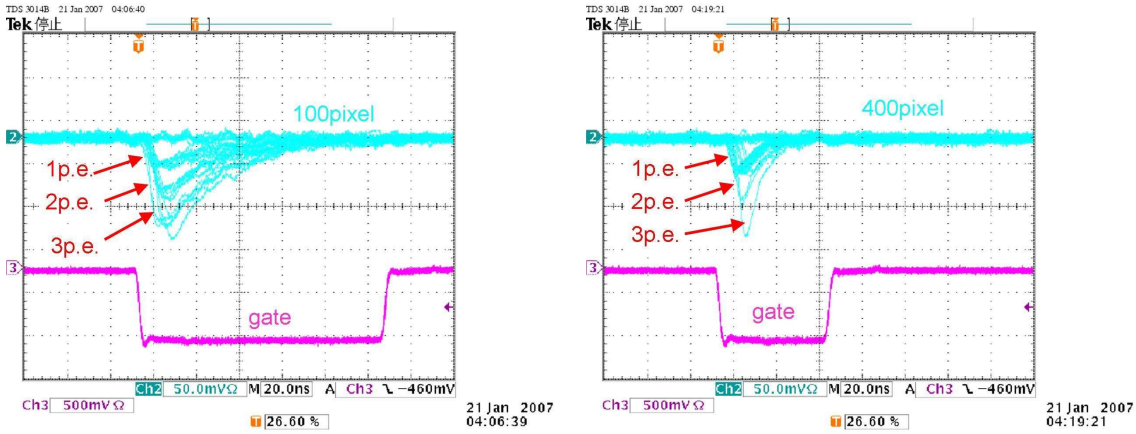

Figure 4.3: Raw signals of 100 (left) and 400 (right) pixel devices taken with an oscilloscope. A pink line in each figure shows a gate signal to the ADC.

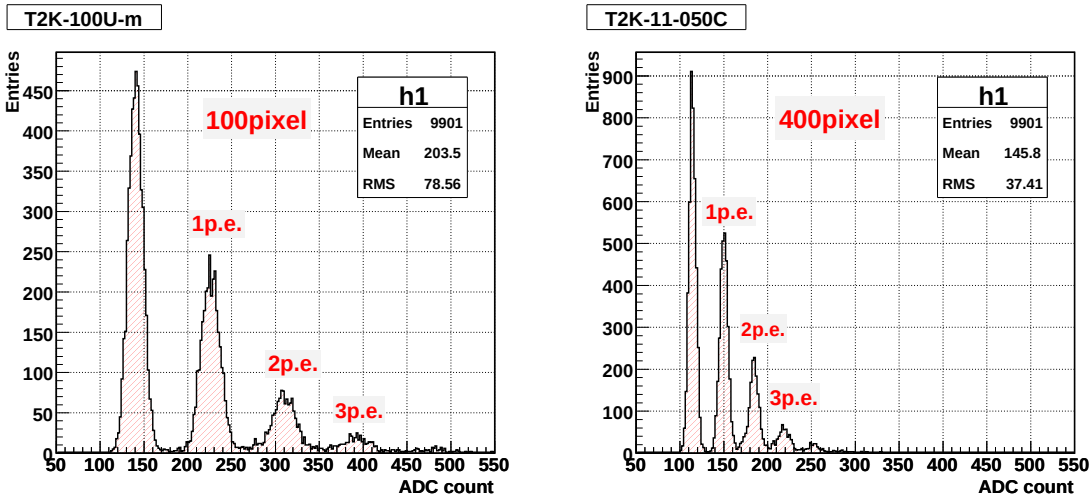

Figure 4.4: ADC distributions of 100 (left) and 400 (right) pixel devices. The leftmost peak in each figure is the pedestal.

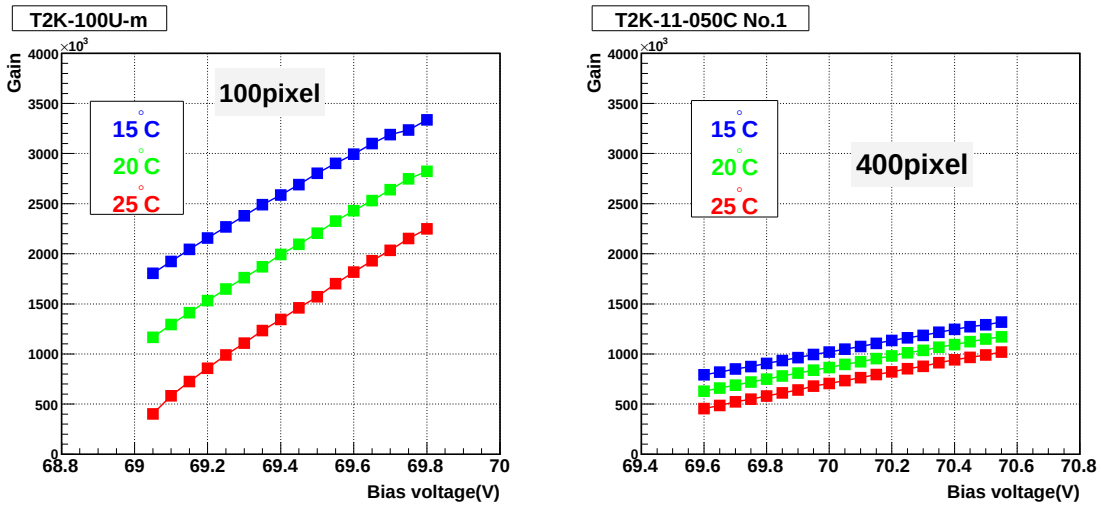

Figure 4.5: Measured gain for 100 (left) and 400 (right) pixel devices as a function of the applied voltage. Blue, green, and red points correspond to the data at 15, 20 and 25°C, respectively.

above the breakdown voltage (V_{bd}). The breakdown voltage is derived by linearly extrapolating the gain-voltage curve in Fig. 4.5 to the point where gain becomes zero. The breakdown voltage decreases with lower temperature, resulting in larger gain at a fixed voltage. The voltage coefficient is +15 (+8)%/0.1 V for the 100 (400) pixel device, respectively. The temperature coefficient is −2 (−3)%/°C for the 100 (400) pixel device, respectively.

Next Fig. 4.6 shows the measured gain for 100 and 400 pixel devices as a function of the difference between the applied voltage and the breakdown voltage, $V - V_{bd}$ ($\equiv \Delta V$). One can see that gain at the same ΔV takes the same value independently from the temperature, hence gain is a function of only ΔV.

The device-by-device gain variation as a function of the applied voltage and ΔV is also measured for 400 pixel devices at 20°C. The result is shown in Fig. 4.7. The device-by-device variation at the same applied voltage is about 15%. However each device has the same gain if we compare at the same ΔV. This result implies that the device-by-device gain variation results from the device-by-device variation of V_{bd}.

Finally the breakdown voltage V_{bd} for 100 and 400 pixel devices as a function of the temperature is shown in Fig. 4.8. For the 400 pixel devices we show the results of three samples. One can see that V_{bd} increases linearly with the temperature, which is consistent with the description in [15]. Moreover we find that the slope of the V_{bd} - temperature relation of each 400 pixel device is same within the error.

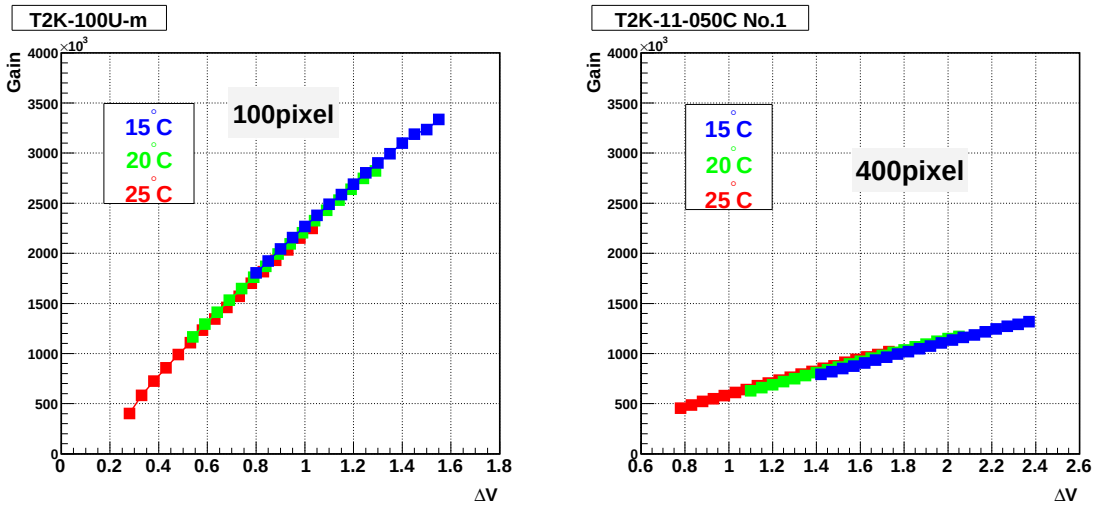

Figure 4.6: Measured gain for 100 (left) and 400 (right) pixel devices as a function of ΔV. Blue, green and red points correspond to the data at 15, 20, and 25°C, respectively.

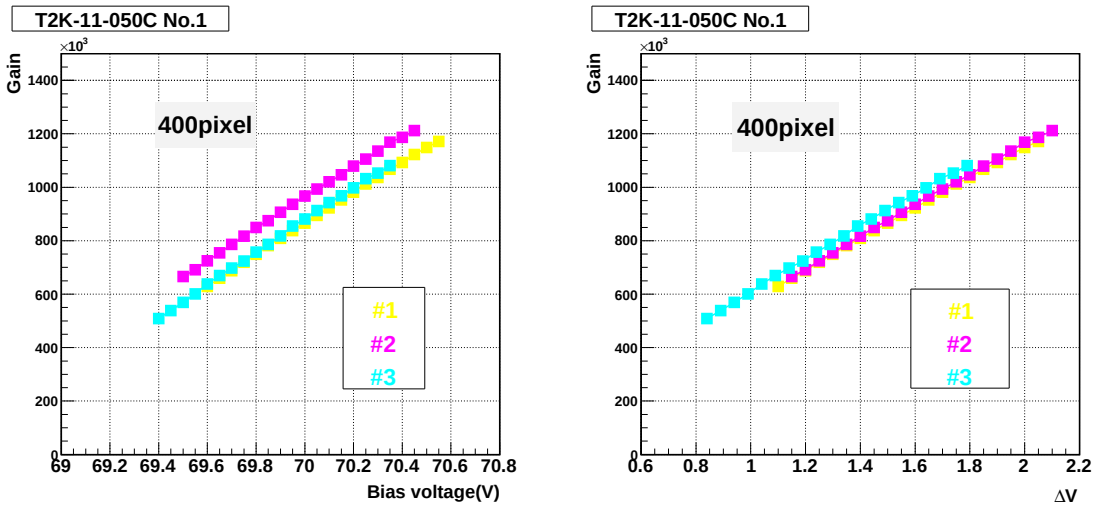

Figure 4.7: Device-by-device gain variation for 400 pixel devices at 20°C as a function of the applied voltage (left) and ΔV (right). Different colors correspond to the different samples of the same type of MPPC.

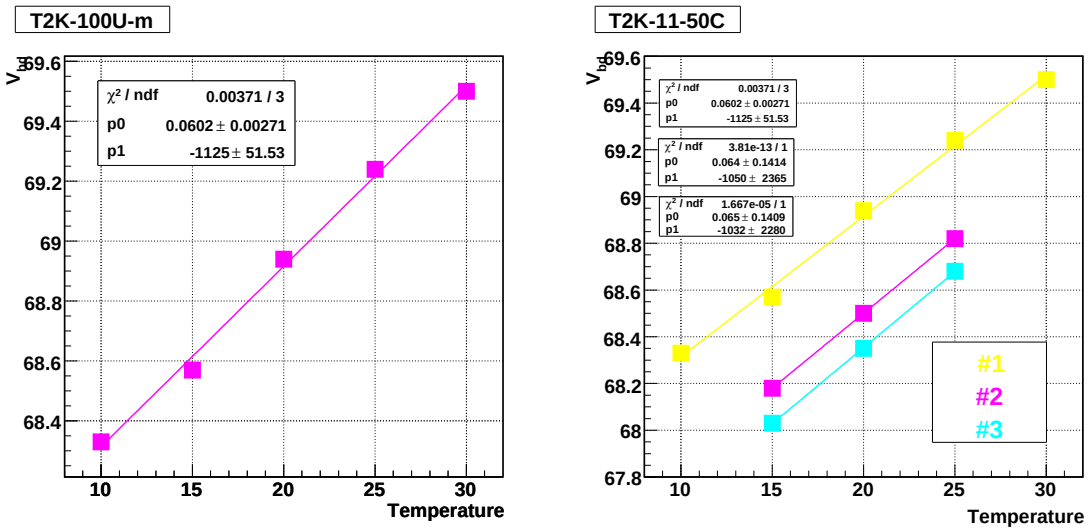

Figure 4.8: Breakdown voltage for 100 (left) and 400 (right) pixel devices as a function of the temperature. In the right figure different colors corresponds to the different samples of the same type of MPPC. The linearly fitted line is also showed.

4.5 Noise rate

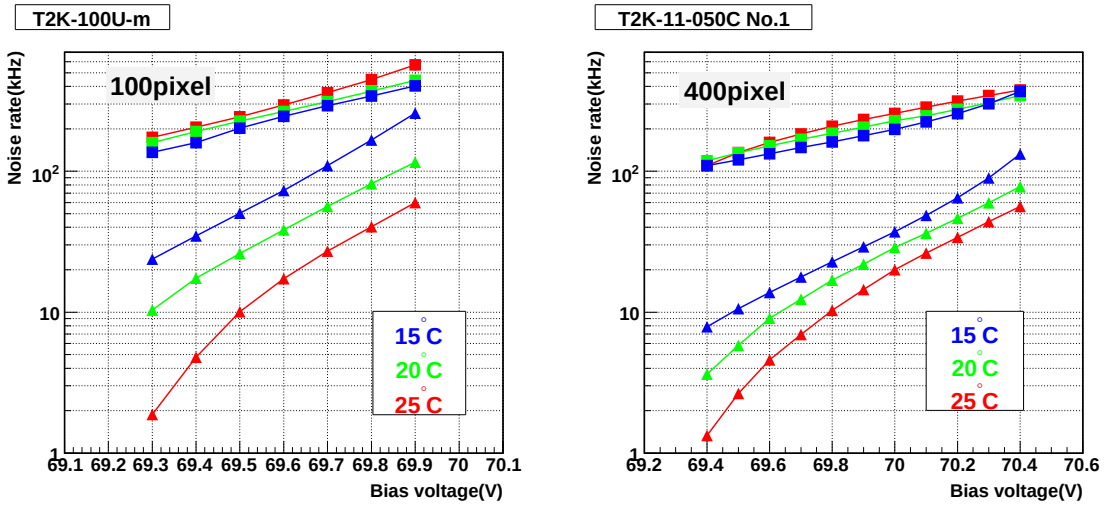

Figure 4.9: Measured noise rate of 100 (left) and 400 (right) pixel devices as a function of the applied voltage. Blue, green, and red points correspond to the data at 15, 20, and 25°C, respectively. Rectangular and triangle points represent the rate at the thresholds of 0.5 and 1.5 p.e., respectively.

A Geiger discharge can be triggered by not only incoming photons but also thermally generated free carriers. Because the thermal generation occurs randomly and independently from each pixel, MPPC emits dark noise with typically 1 p.e. pulse height. The noise rate of MPPC is several hundreds kHz and much higher than that of an usual photomultiplier tube. Hence it is important to reduce the noise rate in the development of MPPC and the noise rate is one of the important basic parameters of MPPC which should be measured. The noise rate of MPPC is measured by counting the rate above the 0.5 p.e. and 1.5 p.e. thresholds without external light input. The results at 15, 20 and 25 °C are shown in Fig. 4.9.

The measured noise rate at the 0.5 p.e. threshold is 100 $\sim$ 500 kHz. However, it decreases by about an order of magnitude if the threshold is set to 1.5 p.e. The noise rate measured at the 0.5 p.e. threshold deceases as the temperature becomes lower, while the noise rate measured at the 1.5 p.e. threshold shows the opposite behaviour. This is because that cross-talk rate at the same bias voltage increases as the temperature becomes lower, as shown in Fig. 4.16. The voltage coefficient is about +15 (+10)%/0.1 V for the 100 (400) pixel device, respectively. The temperature coefficient is about +3%/°C for both devices.

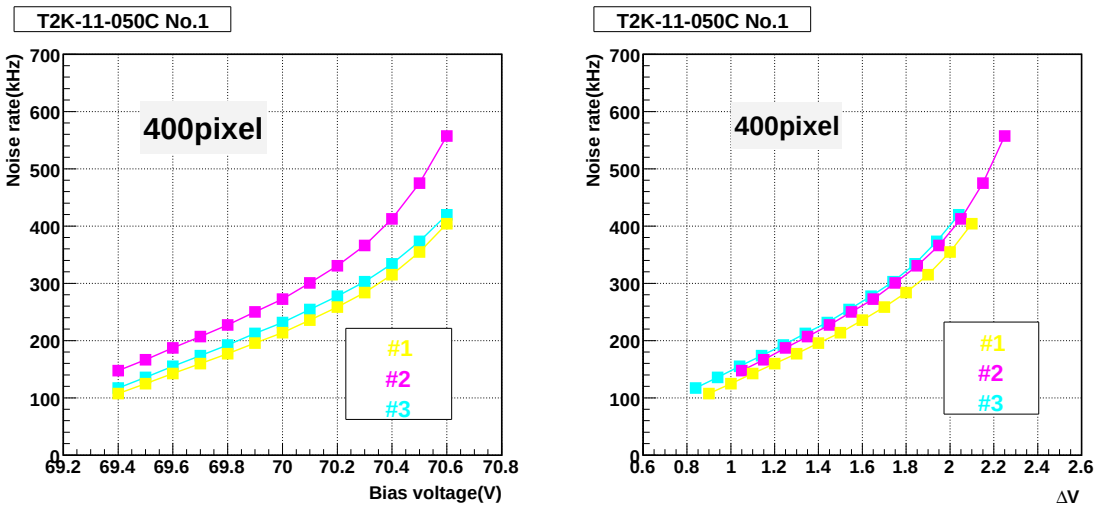

Figure 4.10: Device-by-device variation of noise rate measured at the 0.5 p.e. threshold for 400 pixel devices. The left figure is as a function of the applied voltage and the right one as a function of ΔV. This is measured at 20°C. Different colors correspond to the different samples of the same type of MPPC.

The device-by-device variation of noise rate at the 0.5 p.e. threshold for 400 pixel devices is also shown in Fig. 4.10. The left figure is as a function of the applied voltage and the right as a function of ΔV. This is measured at 20°C. The device-by-device variation at the same applied voltage is about 20%, but

the variation at the same ΔV becomes a few %. This result means that the device-by-device variation of noise rate is mainly due to the variation of V_{bd}.

4.6 Photon Detection Efficiency (PDE)

The photon detection efficiency (PDE) of MPPC is written as a product of three parameters:

$$\mathrm{PDE} = \epsilon_{geom} \times \mathrm{QE} \times \epsilon_{Geiger} \tag{4.4}$$

The meaning of each parameter is as follows.

- ϵ_{geom} : Geometrical fraction of the active area at the surface of MPPC. Generally the active area becomes smaller as the number of pixels becomes larger.
- QE : Quantum efficiency of an avalanche photodiode. This depends on the wavelength of incoming photon to MPPC.
- ϵ_{Geiger} : Probability of generating a Geiger discharge when a photoelectron is produced in the active area. This depends on the applied voltage.

Because it is difficult to know the absolute light intensity which is injected to MPPC, we have measured the PDE of MPPC relative to that of the PMT, Hamamatsu H8643. The specification of the PMT is summarized in Table 4.2.

Model	Hamamatsu H8643
Size	31 mm
Active Diameter	20 mm
Cathode Type	Bialkali
Quantum Efficiency	15% at λ = 450 nm
Typical Gain	5.7×10^6

Table 4.2: Specification of the PMT used at the measurement of PDE.

4.6.1 Setup

The setup for the measurement of PDE is shown in Fig. 4.11. With this setup, MPPC and the PMT are illuminated with green light from a fiber, Kuraray Y11, through a slit with the 1mm diameter. Because the active area of MPPC is 1 mm $\times$ 1 mm, all the light from the slit is injected to MPPC. MPPC and the PMT are each moved around the slit in two dimensions and the position with the maximum light yield is found. We calculate the obtained number of photoelectrons at the

maximum light yield position for MPPC and the PMT. The PDE of MPPC relative to that of the PMT is defined as the following;

$$\text{PDE(MPPC)/QE(PMT)} = \frac{\text{p.e.(MPPC)}}{\text{p.e.(PMT)}}, \tag{4.5}$$

where p.e.(MPPC) is the number of photoelectrons for MPPC and p.e.(PMT) is that for the PMT. In order to avoid the effect of cross-talk, the number of photoelectrons for MPPC is derived from the fraction of pedestal (= 0 p.e.) events to the total number of triggers, assuming a Poisson distribution. For the PMT, the number of photoelectrons is calculated by dividing the mean output charge by the charge corresponding to 1 p.e.

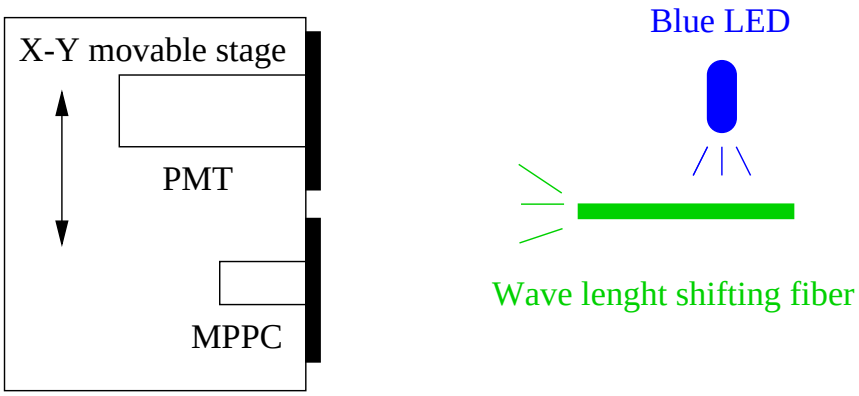

Figure 4.11: Setup for measuring PDE. MPPC and the PMT are illuminated with green light from a fiber. They are each moved around a slit in two dimensions and the position with the maximum light yield is found.

4.6.2 Results

The measured PDE as a function of the applied voltage is shown in Fig. 4.12. The left (right) figure is for a 100 (400) pixel device. The data at 15, 20, and 25°C are shown in these figures. The PDE of MPPC is about or more than twice higher than that of the PMT. Especially for the 100 pixel device, the PDE is almost three times higher than that of the PMT. This is a great improvement from the old samples, as shown in Appendix A. The PDE becomes lower as the temperature becomes higher. This is also explained by the fact that the breakdown voltage becomes higher as temperature becomes higher. The voltage coefficient is about +20 (+6)%/0.1 V for the 100 (400) pixel device, respectively. The temperature coefficient is about −5%/°C for both devices.

The measured PDE of 100 and 400 pixel devices as a function of ΔV is also shown in Fig. 4.13. From these figures, one can see that PDE at the same ΔV

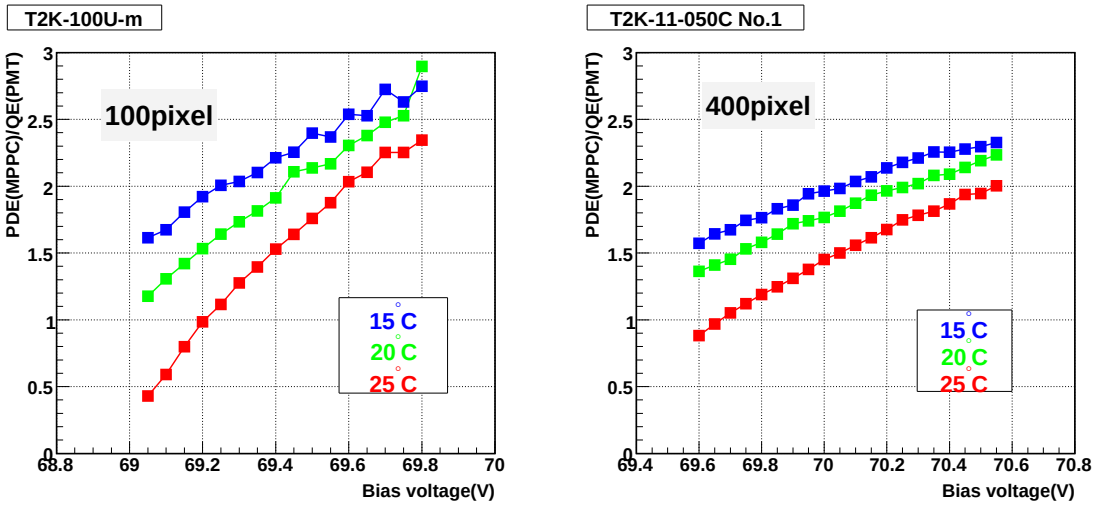

Figure 4.12: Measured PDE as a function of the applied voltage. The left (right) figure is for a 100 (400) pixel device. Blue, green, and red points correspond to the data at 15, 20 and 25°C, respectively.

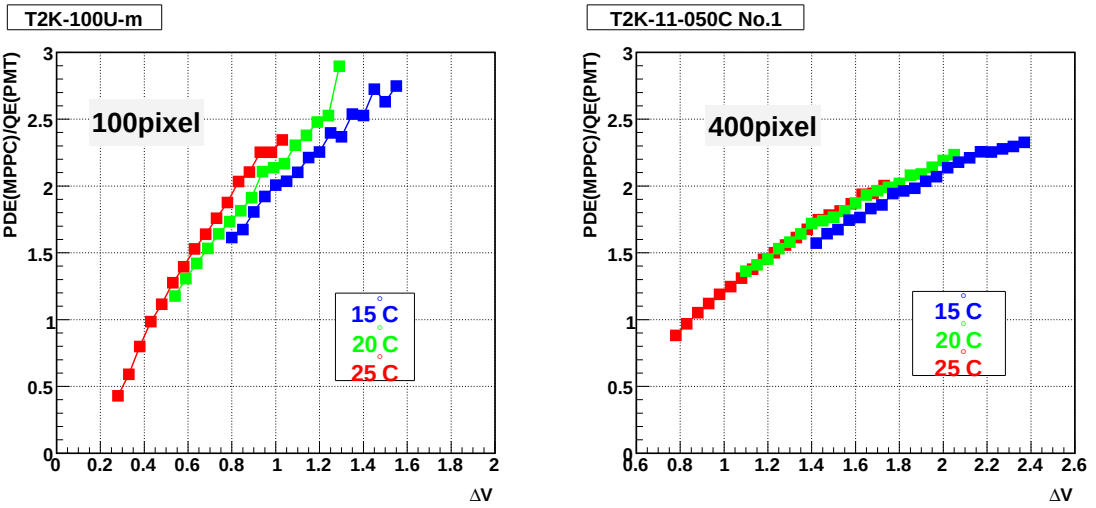

Figure 4.13: Measured PDE of 100 (left) and 400 (right) pixel devices as a function of ΔV. Blue, green and red points correspond to the data at 15, 20, and 25°C, respectively.

takes the same value independently from the temperature. Consequently we can conclude that PDE is a function of only ΔV.

The device-by-device variation of PDE for 400 pixel devices as a function of the applied voltage and ΔV is shown in Fig. 4.14. This is measured at 20°C. The device-by-device variation of PDE at the same bias voltage is found to be about 6%. However each device has the same PDE at the same ΔV. This result means that the device-by-device variation of PDE results from the device-by-device variation of ΔV as is in the same case of gain and noise rate.

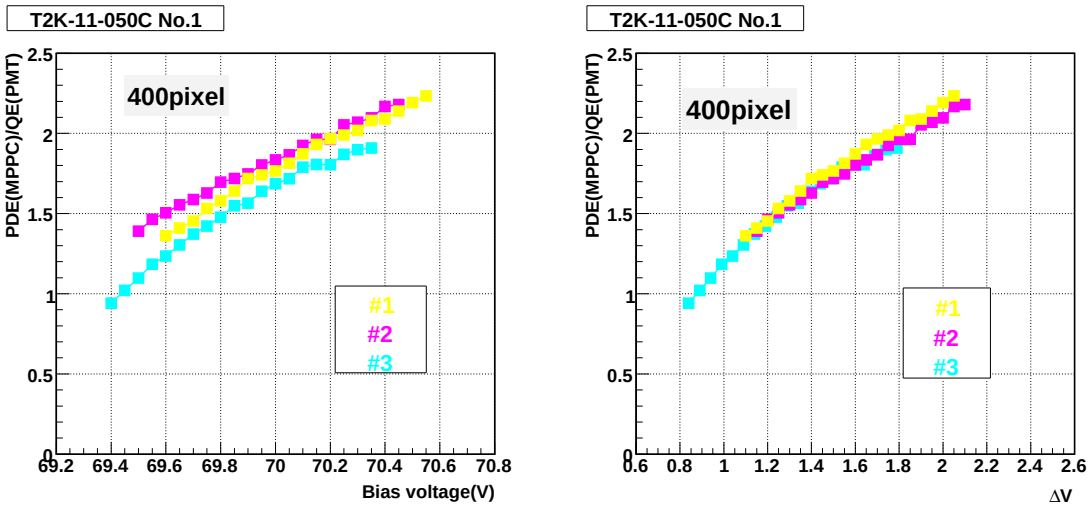

Figure 4.14: Device-by-device variation of PDE for 400 pixel devices at 20°C as a function of the applied voltage (left) and ΔV (right). Different colors correspond to the different samples of the same type of MPPC.

At last in this section we discuss the absolute value of the breakdown probability , ϵ_{Geiger} in Eq. 4.4. We assume that the QE of the PMT for green light is 15% and that of the APD is 70%. We can estimate ϵ_{geom} from the measurement with a laser injection system as shown in Fig. 5.14; 72 (58)% for a 100 (400) pixel device, respectively. Using these values, we calculate ϵ_{Geiger} for 100 and 400 pixel devices as a function of the applied voltage. The results are shown in Fig. 4.15. From these figures we see ϵ_{Geiger} almost reaches 100% and MPPC works in the Geiger mode efficiently.

4.7 Interpixel cross-talk rate

The cross-talk between neighboring pixels has been observed. The origin of the cross-talk is presumed that the optical photons emitted in an avalanche enter the neighboring pixels and generate another Geiger discharge[14]. The probability of cross-talk is estimated by the following method.

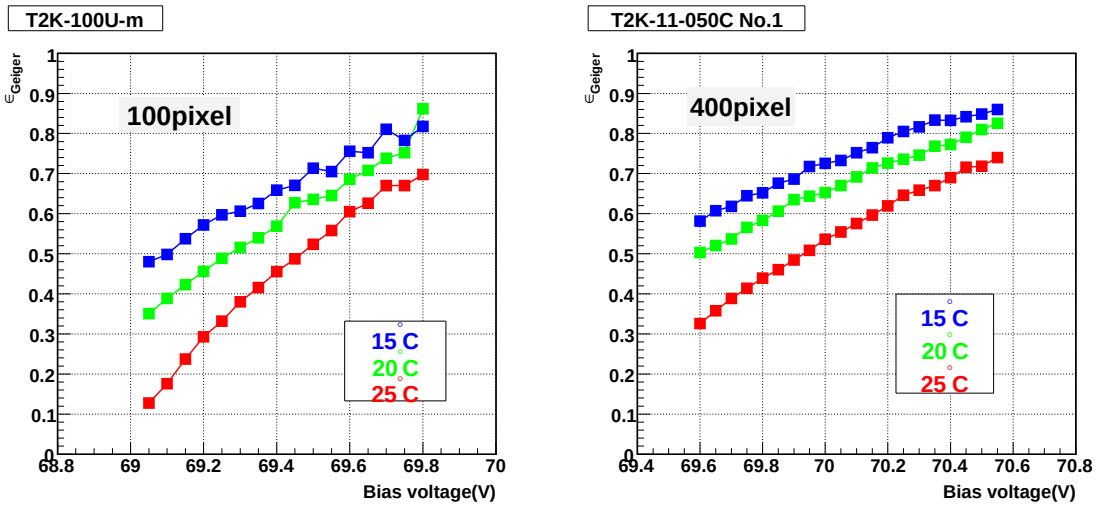

Figure 4.15: Calculated ϵ_{Geiger} of 100 (left) and 400 (right) devices as a function of the applied voltage. Blue, green and red points correspond to the data at 15, 20 and 25 °C, respectively.

1. MPPC is illuminated by a blue LED with low intensity.
2. Fraction of pedestal events is calculated from the ADC distribution.
3. Fraction of 1 p.e. events is estimated from the fraction of the pedestal events assuming a Poisson distribution.
4. Compare the estimated fraction of 1 p.e. events to the actually observed fraction of 1 p.e. events.

Because cross-talk only occurs when a Geiger discharge happens in a certain pixel, the fraction of pedestal events is independent of cross-talk. Therefore the fraction of 1 p.e. events estimated from the fraction of pedestal events is the value when there is no cross-talk. If there is cross-talk, the observed fraction of 1 p.e. events must be smaller than the estimated fraction of 1 p.e. events. This difference is attributed to cross-talk.

The cross-talk rate estimated by the above method is written as;

$$(\text{Cross} - \text{talk rate}) = 1 - \frac{f_{observed}}{f_{estimated}}, \tag{4.6}$$

where $f_{observed}$ is the observed fraction of 1 p.e. events and $f_{estimated}$ is the estimated fraction of 1 p.e. events.

The effect of accidental coincidence of random noise has not been subtracted, however this effect is roughly estimated as follows;

$$100 \text{ ns} \times 300 \text{ kHz} \times 300 \text{ kHz} = 9 \text{ kHz}, \tag{4.7}$$

where we assume that the gate width is 100 ns and the noise rate at the 0.5 p.e. threshold is 300 kHz. The effect of accidental coincidence of random noise is 3% (= 9/300), while the measured cross-talk rate is found to be 10 $\sim$ 40 %. Hence we can neglect this effect.

4.7.1 Results

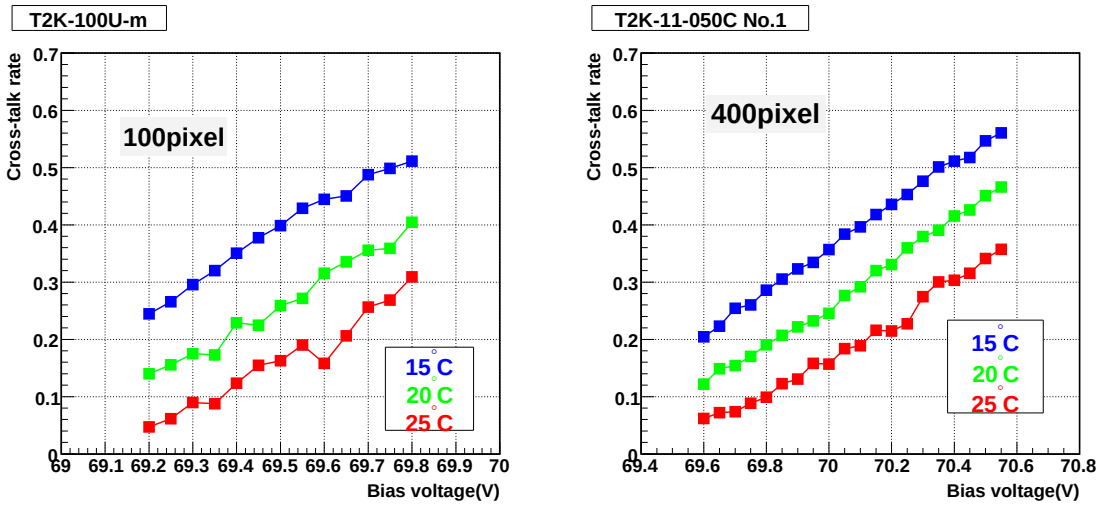

Figure 4.16: Cross-talk rate of 100 (left) and 400 (right) pixel devices as a function of the applied voltage. Blue, green, and red points correspond to the data at 15, 20, and 25°C, respectively.

Figure 4.16 shows the cross-talk rate of 100 (left) and 400 (right) pixel devices as a function of the applied voltage. The measured cross-talk rate is 0.1 $\sim$ 0.4, which increases as the applied voltage increases. The cross-talk rate at the same bias voltage seems to be higher as temperature becomes lower. This is explained by the fact that the breakdown voltage becomes lower as temperature becomes lower. The voltage coefficient is +10 (+20)%/0.1 V for the 100 (400) pixel device. The temperature coefficient is about −12 (−9)%/°C for the 100 (400) pixel device. The measured cross-talk rate is within the acceptable level for T2K. However it has been increased from the samples in the previous production cycle. This is shown quantitatively in Appendix A. For applications that require good linearity with wide dynamic range (e.g. ILC calorimeters), the large cross-talk rate may limit the performance of the device. Reduction of cross-talk rate is one of the improvement items in the next production cycle.

Fig. 4.17 shows the measured cross-talk rate of 100 (left) and 400 (right) pixel devices as a function of ΔV. From these figures, one can see cross-talk rate at the same ΔV takes the same value independently from the temperature. Therefore we can conclude that cross-talk rate is a function of only ΔV.

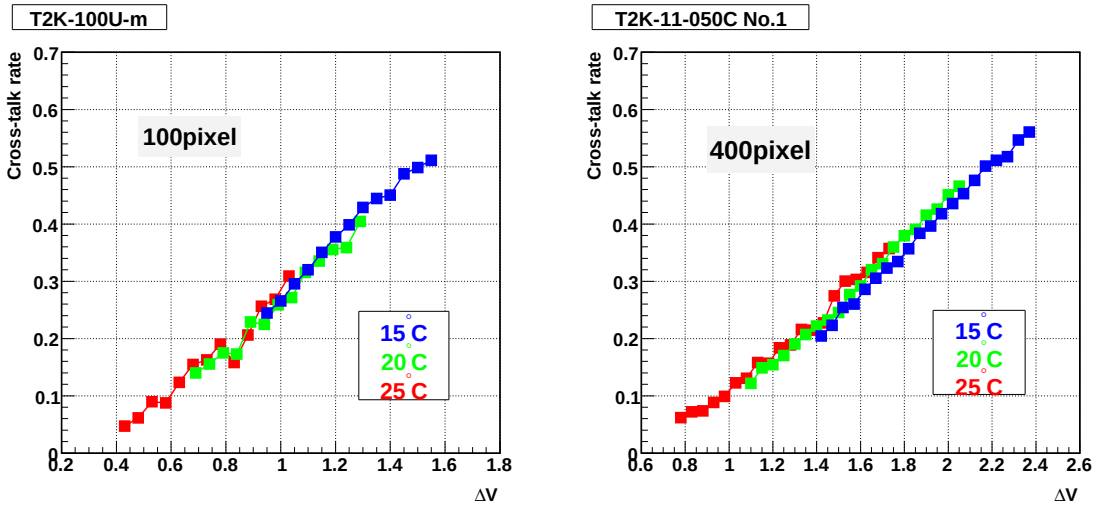

Figure 4.17: Cross-talk rate of 100 (left) and 400 (right) pixel devices as a function of ΔV. Blue, green, and red points correspond to the data at 15, 20, and 25°C, respectively.

Next we show in Fig. 4.18 the device-by-device variation of cross-talk rate for 400 pixel devices as a function of the bias voltage and ΔV. This is measured at 20 °C. The device-by-device variation of cross-talk rate at the same applied voltage is found to be 25%. However each device has the same cross-talk rate at the same ΔV. This result also means that the device-by-device variation of cross-talk rate comes from the device-by-device variation of ΔV.

Next, we assume that cross-talk rate is described by the following equation:

$$(\text{Cross} - \text{talk rate}) = f_{geom} \times P_{photon} \times \text{QE} \times \epsilon_{Geiger} \tag{4.8}$$

The meaning of each parameter is the following.

- f_{geom} : Factor contributing to cross-talk determined by the geometry of a device, such as optical isolation between pixels, the distance between neighbouring pixels, and etc.
- P_{photon} : Probability that photons are generated during a Geiger discharge in one pixel
- QE : Quantum efficiency of an avalanche photodiode

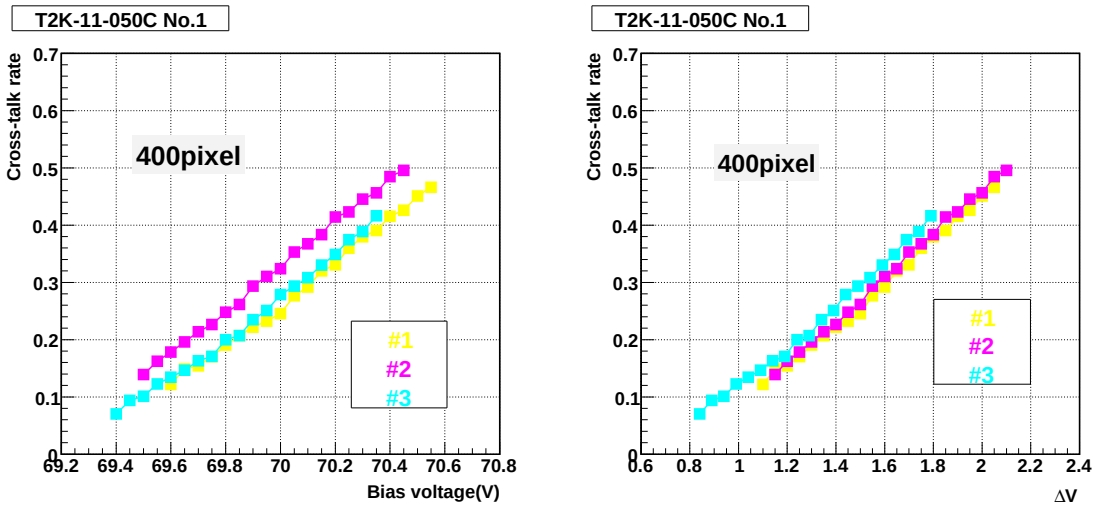

Figure 4.18: Device-by-device variation of cross-talk rate for 400 pixel devices at 20°C as a function of the applied voltage (left) and ΔV (right). Different colors correspond to the different samples of the same type of MPPC.

- ϵ_{Geiger} : Probability of generating a Geiger discharge

At first we discuss the parameter P_{photon}. From Eq. 4.8 we can see the ratio of cross-talk rate to ϵ_{Geiger} should be proportional to P_{photon}. Figure 4.19 shows the ratio of cross-talk rate to ϵ_{Geiger} as a function of ΔV, calculated with the measured cross-talk rate shown in Fig. 4.17 and the estimated ϵ_{Geiger} shown in Fig. 4.15. The left (right) figure is for a 100 (400) pixel device. From these figures P_{photon} is found to be proportional to ΔV, or gain. We assume that QE is independent of ΔV. This conclusion is consistent with the description in [14] that the number of photons emitted during a Geiger discharge is proportional to the number of generated carriers, or gain.

Next we discuss the parameter f_{geom} of the 100 and 400 pixel devices. We can see from the above discussion that P_{photon} is proportional to gain, where the proportionality constant for the 100 pixel device is the same as that for the 400 pixel one. Assuming the QEs of 100 and 400 pixel devices are same, therefore, f_{geom} is expressed by the following formula:

$$f_{geom} \propto \frac{(\mathrm{cross-talk\ rate})}{\epsilon_{Geiger} \times \mathrm{gain}}, \tag{4.9}$$

where its proportionality constant is also the same for both 100 and 400 pixel devices. We know the value of ϵ_{Geiger} from Fig. 4.15, cross-talk rate from Fig. 4.17, and gain from Fig. 4.6. Using these values we can calculate f_{geom} for the 100 and 400 pixel devices as a function of ΔV, as shown in Fig. 4.20. The calculated f_{geom} is almost independent from ΔV, as expected. f_{geom} for the 100

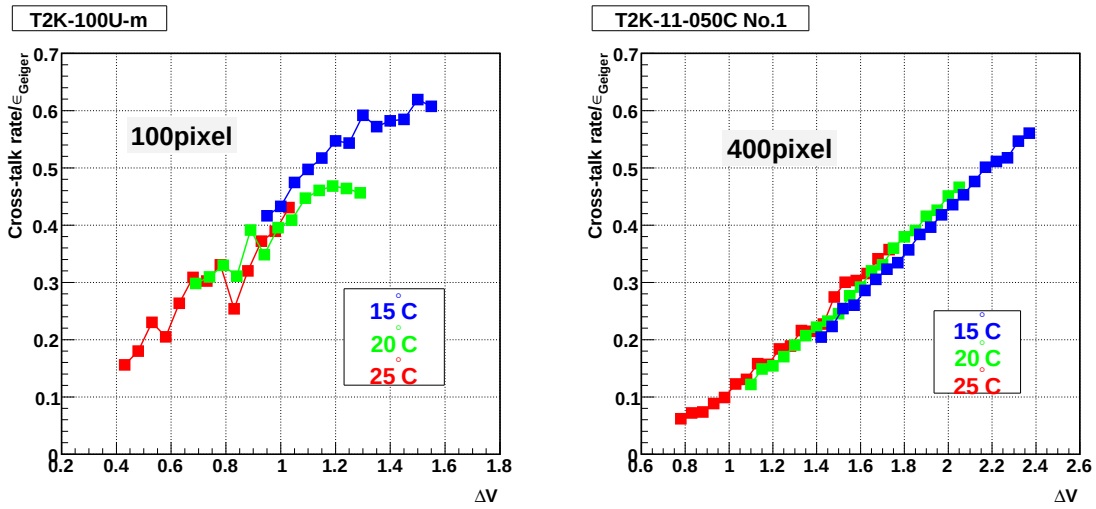

Figure 4.19: Ratio of the cross-talk rate to ϵ_{Geiger} as a function of ΔV. The left figure is for a 100 pixel device, and the right one is for a 400 pixel device. Blue, green and red points correspond to the data at 15, 20 and 25°C, respectively.

pixel device is about a half of that for the 400 pixel device. This is explained as the following. The photons generated during a Geiger discharge in one pixel suffer more attenuation as they pass through longer distance. The pixel pitch of the 100 pixel device (100 μm) is longer than that of the 400 pixel device (50 μm). Therefore it is reasonable that the cross-talk rate for the 100 pixel device is lower than that for the 400 pixel device.

4.8 Linearity

The linearity of the MPPC response to the large amount of light is intrinsically limited by the finite number of micropixels. Figure 4.21 shows the number of fired pixels of 100 and 400 pixel devices as a function of light intensity at 20°C. The number of injected photoelectrons is estimated by the p.e. detected by a monitor PMT. We keep the linearity of the PMT by changing the applied voltage of the PMT and repeating the same measurement. The red curve shows the expected response calculated with the number of pixels and the separately measured cross-talk rate, and described by the following equation:

$$N_{fired} = N_0 \times (1 - \exp(\frac{\mathrm{x}(1+\mathrm{c})}{N_0})), \tag{4.10}$$

where

- N_{fired} : Number of fired pixels

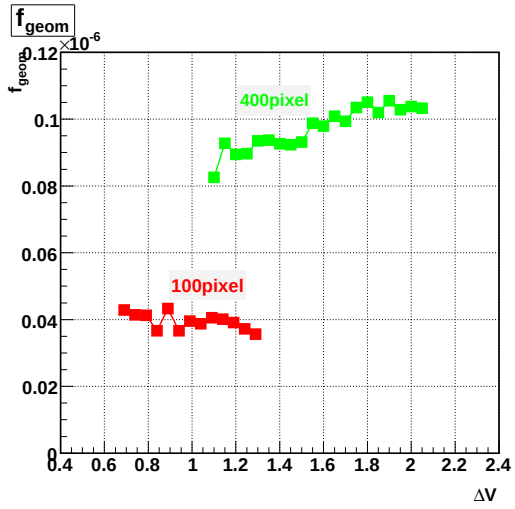

Figure 4.20: Calculated f_{geom} using the estimated ϵ_{Geiger}, the measured cross-talk rate, and gain. Red points correspond to a 100 pixel device and green ones a 400 pixel device. This is measured at 20°C.

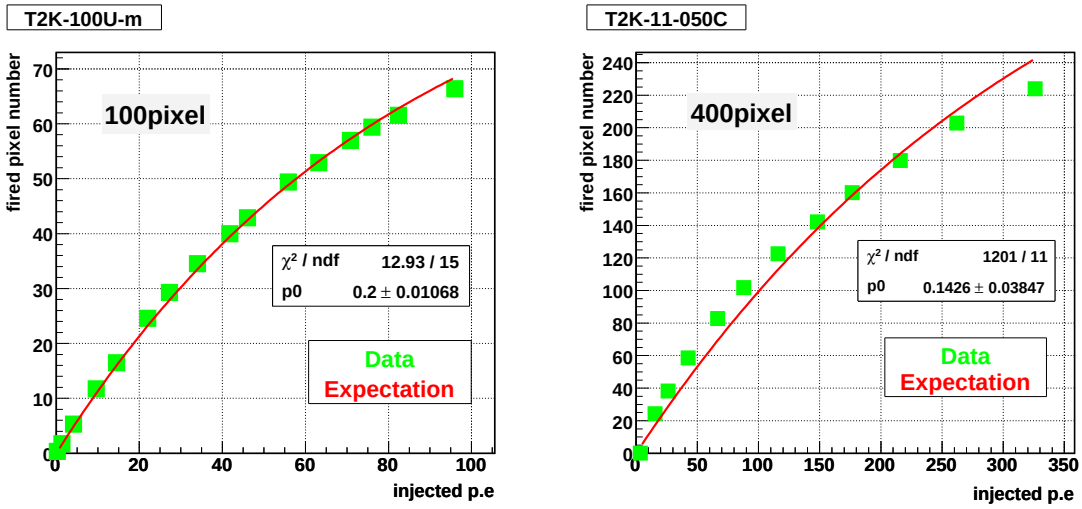

Figure 4.21: Response of 100 (left) and 400 (right) pixel devices as a function of light intensity at 20°C. Green points correspond to data and the red curve to the expected response calculated with the number of pixels and the measured cross-talk rate.

- N_0 : Number of pixels
- x : Number of injected photoelectrons
- c : Cross-talk rate

The derivation of this equation is explained in Appendix C. Fig. 4.22 shows the deviation from the expected curve for the 100 (left) and 400 (right) pixel devices. The deviation from the expected curve is calculated as;

$$\frac{(\text{data}) - (\text{expectation})}{(\text{data})} \times 100(\%) \tag{4.11}$$

The deviation is found to be within 5 (20)% for the 100 (400) pixel device, respectively. Thus the MPPC response to the large amount of light is well understood.

Figure 4.23 shows the deviation from the linearly fitted line in the low injected photoelectrons at 20°C for the 100 (left) and 400 (right) pixel devices. The deviation from the linear line is calculated as;

$$\frac{(\text{data}) - (\text{linear line})}{(\text{data})} \times 100(\%) \tag{4.12}$$

The nonlinearity is 20% at the 40 (120) injected photoelectrons for the 100 (400) pixel device, respectively.

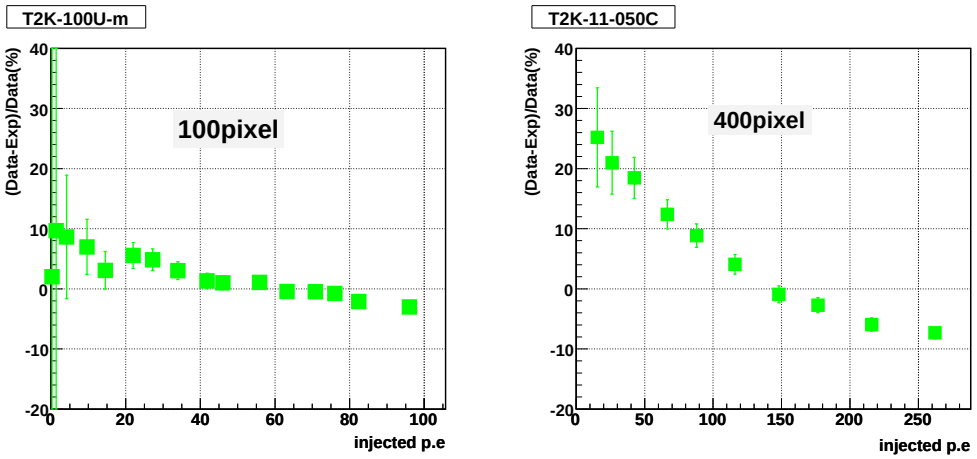

Figure 4.22: Deviation from the expected curve calculated with the number of pixels and the separately measured cross-talk rate for 100 (left) and 400 (right) pixel devices. The deviation is found to be within 5 (20)% for the 100 (400) pixel device, respectively.

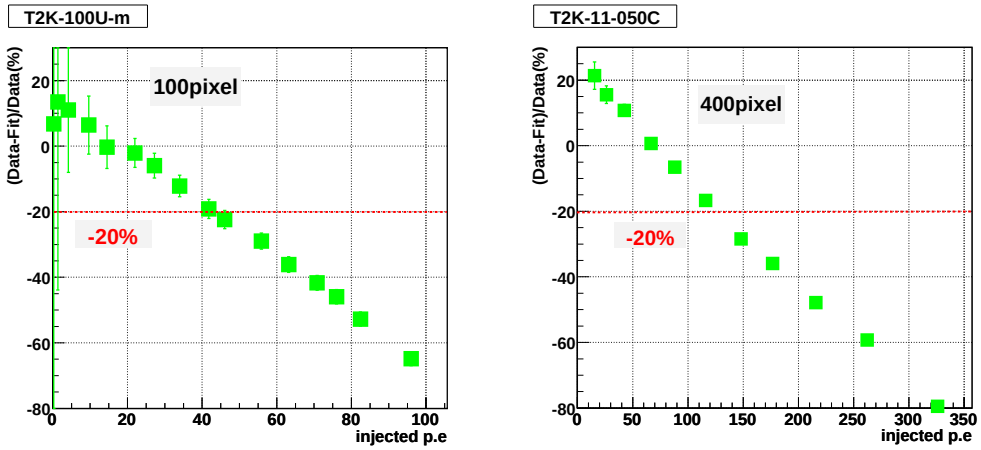

Figure 4.23: Deviation from the linearly fitted line for 100 (left) and 400 (right) pixel devices at 20°C. A red line shows the 20% nonlinearity. The nonlinearity is 20% at the 40 (120) injected photoelectrons for the 100 (400) pixel device, respectively.

4.9 Recovery time

The use of MPPC at high counting rate is limited due to the finite time taken to quench an avalanche and then reset the applied voltage to its initial value. In order to study this recovery time we fire all pixels of MPPC by the light from one LED (LED1) and check the response to the light from another LED (LED2) with changing the time difference between the LED1 and the LED2. We tested both 100 and 400 pixel devices. The results are shown in Fig. 4.24. The signal size for the LED2 corresponds to the charge when all pixels are fired and does not change even if we change the time difference from 1 μs to 100 ns. From this result we can see that all pixels are recovered 100 ns after all pixels are fired and the recovery time is $<$ 100 ns for both 100 and 400 pixel devices. The recovery time is comparable to the signal width[1]. This recovery time is not a problem at the event rate expected in T2K.

[1]Russian MRS APD has $\sim 1\mu$s recovery time though its signal width is $\sim$ 5 ns [16].

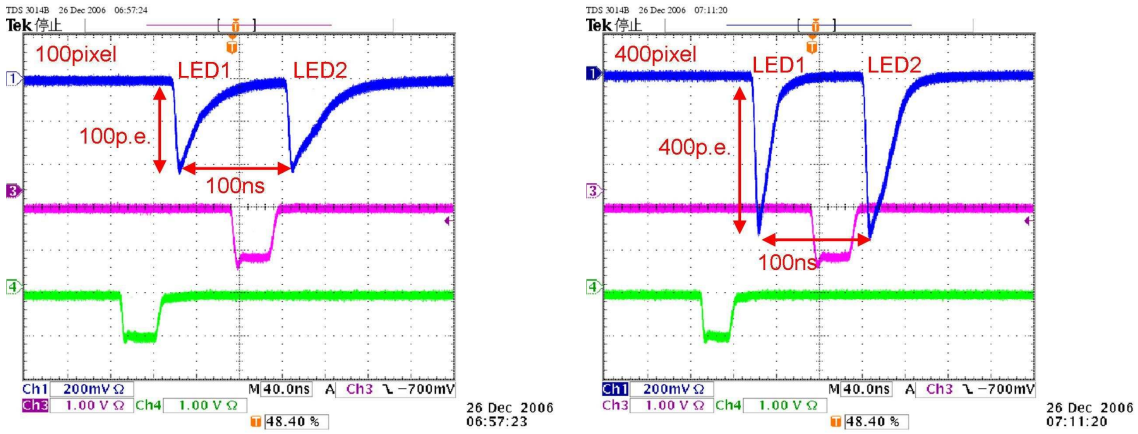

Figure 4.24: Response of 100 pixel (left) and 400 pixel (right) devices to the light from the LED2 when all pixels are fired by the light from the LED1. All pixels are recovered 100 ns after all pixels are fired. A green line shows a trigger to the LED1 and a pink one to the LED2.

4.10 Summary and discussion

We summarize the basic performance of the latest MPPC samples at 20°C in Table 4.3.

Number of pixels	100	400
Gain	$1.0 \times 10^6 \sim 3.0 \times 10^6$	$5.0 \times 10^5 \sim 1.0 \times 10^6$
Noise rate at the 0.5 p.e. th. (kHz)	$100 \sim 500$	$100 \sim 500$
Noise rate at the 1.5 p.e. th. (kHz)	$10 \sim 100$	$10 \sim 100$
Cross-talk rate	$0.1 \sim 0.4$	$0.1 \sim 0.4$
PDE (%)	$20 \sim 45$	$20 \sim 30$
Nonlinearity	20% at 40 p.e.	20% at 120 p.e.
Recovery time	< 100 ns	< 100 ns

Table 4.3: Summary of the basic performance of the latest MPPC samples at 20°C.

We also summarize the voltage and temperature coefficient of each basic parameter of the latest MPPC samples in Table 4.4.

	dP/dV (%/0.1 V)		dP/dT (%/°C)	
Number of pixels	100 pixel	400 pixel	100 pixel	400 pixel
Gain	+15	+8	−2	−3
Noise rate	+15	+10	+3	+3
PDE	+20	+6	−5	−5
Cross-talk rate	+10	+20	−12	−9

Table 4.4: Summary of the voltage (dP/dV) and temperature (dP/dT) coefficient of each basic parameter of the latest MPPC samples.

On the other hand the requirements to MPPC from each detector in ND280 are summarized in Table 4.5. There are some remarks for Table 4.5.

- Requirement to the number of pixels associates with the linearity problem. FGD, P0D and ECAL must be able to detect protons and high energy γ rays which will produce ∼100 p.e. signal. On the other hand the main target of INGrid and SMRD is a muon which will produce $\sim$ 20 p.e. signal.
- Requirements to gain and noise rate come from the readout electronics of MPPC.

Although we have not measured the timing resolution of MPPC now, there is a report that it is several hundreds psec [17]. Comparing the values in Table 4.3

Detector	FGD	P0D	ECAL	SMRD	INGrid
Number of MPPC	9216	15-20 k	8-10 k	∼21 k	∼ 7k
Number of pixels	> 400	> 400	> 400	< 600	~ 100
Gain	$\sim 10^6$	$\sim 10^6$	$\sim 10^6$	$\sim 10^6$	$\sim 10^6$
Noise rate at the 0.5 p.e. th. (kHz)	< 1000	< 1000	< 1000	< 1000	< 1000
Noise rate at the 1.5 (2.5) p.e. th. (kHz)	< 50	< 50	< 50	< 50	< 50
PDE (%)	> 15	> 15	> 15	> 15	> 15
Timing resolution (ns)	$2 \sim 3$	$2 \sim 3$	$2 \sim 3$	$2 \sim 3$	$2 \sim 3$

Table 4.5: List of the requirements to MPPC from each detector in ND280. The explanation of each detector is shown in Subsection 2.2.5.

and 4.5, we can say the performance of MPPC is satisfactory for all T2K near detectors. The range of bias voltage where the requirements for T2K are satisfied is found to be 0.7 V (0.8 V) for a 100 (400) pixel device, respectively. The upper limit is determined by the requirement to 1.5 p.e. threshold noise rate and the lower one is determined by the requirement to PDE. The latest samples achieve enough high PDE, as shown in Fig. 4.15. Thus it is necessary to reduce 1.5 p.e. threshold noise rate, in other words, cross-talk rate, in order to broaden the range of bias voltage where the requirements for T2K are satisfied. Furthermore, we have found the following two issues about the basic performance of MPPC.

- Gain, PDE, and cross-talk rate are all functions of only ΔV.
- Device-by-device variation of all the basic parameters (gain, noise rate, PDE and cross-talk rate) comes from the device-by-device variation of the breakdown voltage. Here we have shown the result only at 20°C, but we have obtained the same result at 15°C and 25°C.

From above results we see it is important to reduce the variation of the breakdown voltage in order to reduce the device-by-device variation of the basic performance of MPPC in mass production.

Chapter 5

TEST WITH A LASER INJECTION SYSTEM

In order to check the response of each micro APD pixel, we have tested MPPC with a pulsed laser system of KEK Detector Technology Project[18]. In this chapter we show the result about the old MPPC samples provided in Jan. 2006. The basic parameters of the laser system are following:

- Wavelength : 532 nm (green)
- Pulse energy : $1 \sim 3$ μJ
- Pulse repetition rate : 8 kHz
- Pulse width : < 2 ns
- Minimum spot size : a few μm

The setup for the laser test is shown in Fig. 5.1. MPPC is placed on an X-Y movable stage that can be controlled with 0.02 μm precision. The alignment of a laser spot to a pixel is possible because the laser spot is visible, as shown in Fig. 5.2. The light intensity of the laser is attenuated by 10^6 with three neutral density filters and adjusted to a few photons by a monitor PMT before testing MPPC. The trigger synchronized with the laser output is provided by the signal of the Si PIN photodiode (Hamamatsu S3590-08) which detects the laser light before the attenuation. The scan by the X-Y movable stage and data acquisition are totally automated and the time for the measurement is typically 30 minutes. The typical ADC distribution with injecting a laser spot to one pixel of a 100 pixel device is shown in Fig. 5.3.

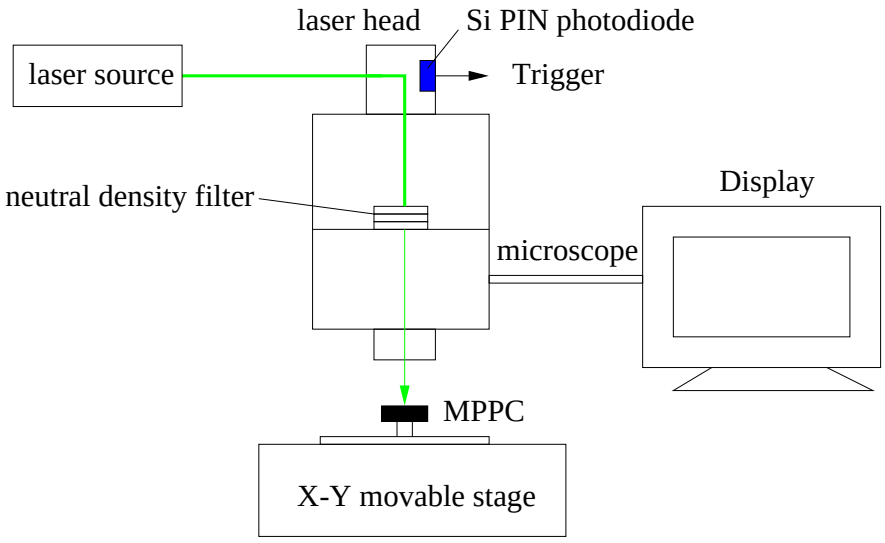

Figure 5.1: Setup of the laser test. MPPC is placed on an X-Y movable stage. The laser intensity is attenuated by 10^6 with three neutral density filters. The trigger synchronized with the laser output is provided by a Si PIN photodiode.

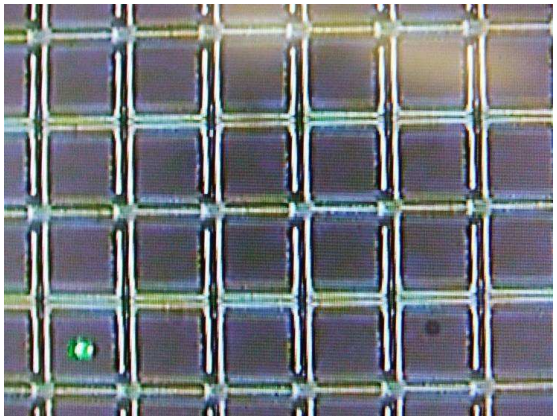

Figure 5.2: Close-up view of APD pixels. One can see a green laser spot in the lower left pixel.

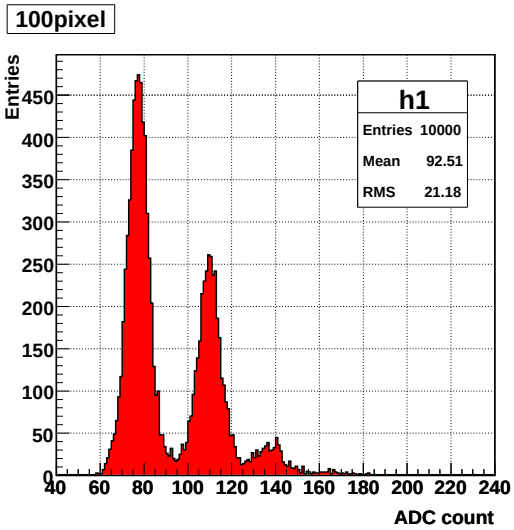

Figure 5.3: ADC distribution of a 100 pixel MPPC with injecting a laser onto one pixel.

The measured items are:

- Uniformity of gain, efficiency and cross-talk rate inside one pixel ··· Section 5.1
- Pixel-to-pixel uniformity of gain, efficiency and cross-talk rate ··· Section 5.2
- Measurement of the active area inside one pixel ··· Section 5.3

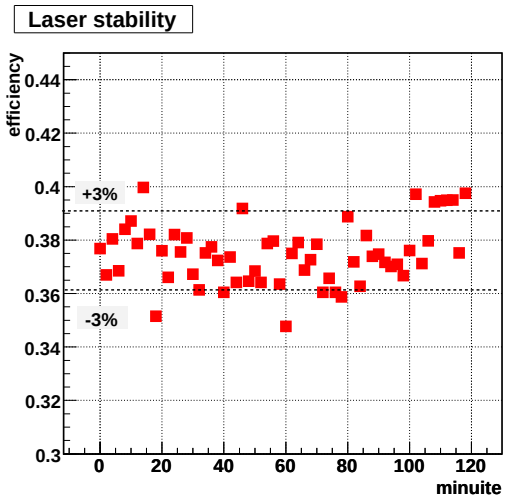

Figure 5.4: Time variation of efficiency for a 100 pixel MPPC. The efficiency is calculated from the fraction of events with more than 0.5 p.e. to the total events in the ADC distribution.

Before the laser test, we have checked the stability of laser intensity during two hours by injecting the laser onto the same one pixel of MPPC and monitoring the time variation of efficiency. The efficiency is calculated from the fraction of events with more than 0.5 p.e. to the total events in the ADC distribution. The time variation of efficiency is shown in Fig. 5.4. From this figure the laser intensity is found to be stable within 3% level.

5.1 Uniformity inside one pixel

We can only measure the total response of all pixels in the test of basic performance described in Chapter 4. For the old sample which was delivered in Apr. 2005, we observed that gain around the edge of a pixel was much higher than that around the center of the pixel [19]. Therefore it is important to check if the response within one pixel is uniform for the new samples. For this purpose the

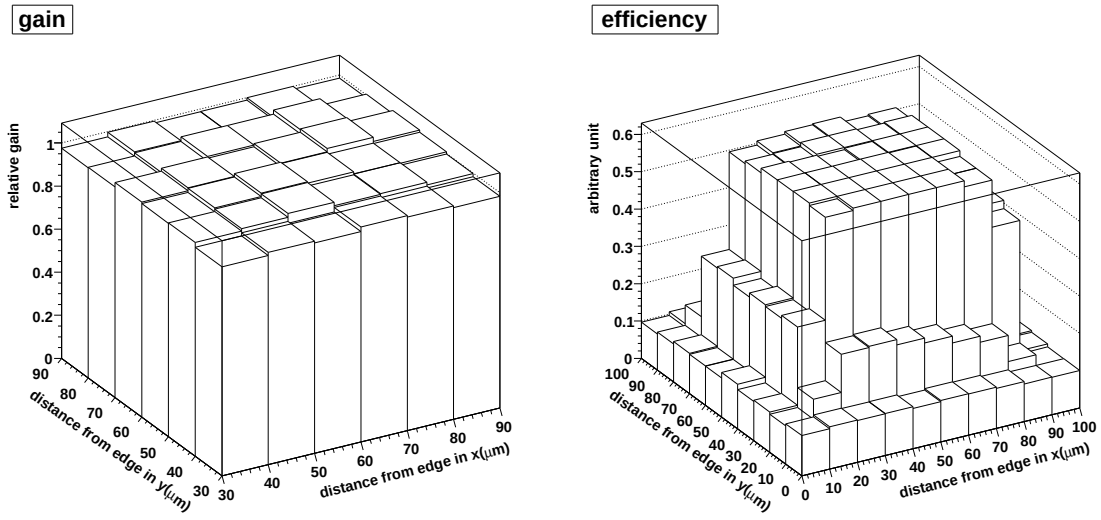

Figure 5.5: Uniformity of gain (left) and efficiency (right) inside one pixel for a 100 pixel device.

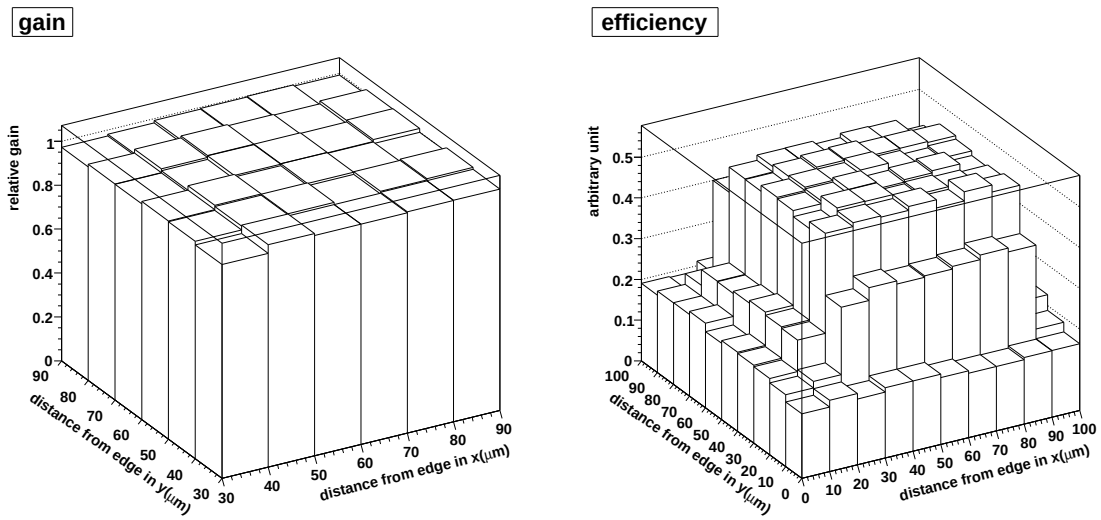

Figure 5.6: Uniformity of gain (left) and efficiency (right) inside one pixel for a 400 pixel device.

light spot is injected onto a pixel and the area within a pixel is scanned with 10 μm pitch. We have tested a few pixels, but show the result of only one pixel.

Figure 5.5 (100 pixel) and 5.6 (400 pixel) show the uniformity of gain and efficiency within one pixel. The efficiency is calculated from the fraction of events more than 0.5 p.e. to the total events in the ADC distribution. The gain is shown only in the active area of a pixel and normalized so that the average over all scanned points is unity. The gain of the 100 and 400 pixel devices is found to be uniform within 2.0% and 1.6% in RMS/mean, respectively. The efficiency of the 100 and 400 pixel devices in the active area of the micropixel is found to be uniform within 2.0% and 1.7%, respectively.

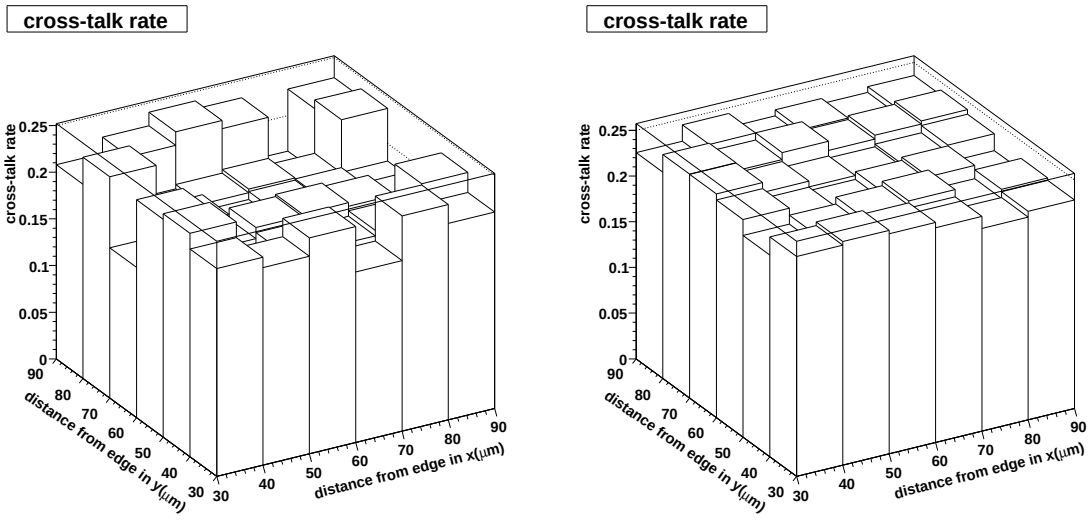

Figure 5.7: Cross-talk rate distribution within one pixel for 100 (left) and 400 (right) pixel devices.

Figure 5.7 shows the cross-talk rate distribution of 100 and 400 pixel devices in the active area of a pixel. The cross-talk rate in this measurement is calculated as the fraction of events with more than 1.5 p.e. to that with 0.5 p.e. The contribution of accidental coincidence of two independent thermal noises is estimated from the random triggered data, and subtracted.

One can see from Fig. 5.7 that the cross-talk rate around the edge of the pixel is larger than that around the center of the pixel. It is qualitatively explained by the fact that cross-talk rate depends on the distance between the point where optical photons are generated and the neighbouring pixel.

5.2 Pixel-to-pixel uniformity

We have observed that the breakdown voltage was different in each pixel for the old sample which was delivered in Apr. 2005 [19]. If the breakdown voltage is different in each pixel, some pixels may not work in the Geiger mode at a certain voltage and the effective number of pixels becomes small. Therefore it is necessary to check if the response of each pixel is uniform. For this purpose the pixel-to-pixel uniformity of gain, efficiency, and cross-talk rate are studied by injecting light in the center of each pixel. The results about the measurements of gain and efficiency are shown in Fig. 5.8 and Fig. 5.9. The efficiency is defined as the fraction of events more than 0.5 p.e. to the total events in the ADC distribution and is normalized so that the average over all pixels is 1.0. The gain is also normalized so that the average over all pixels is 1.0.

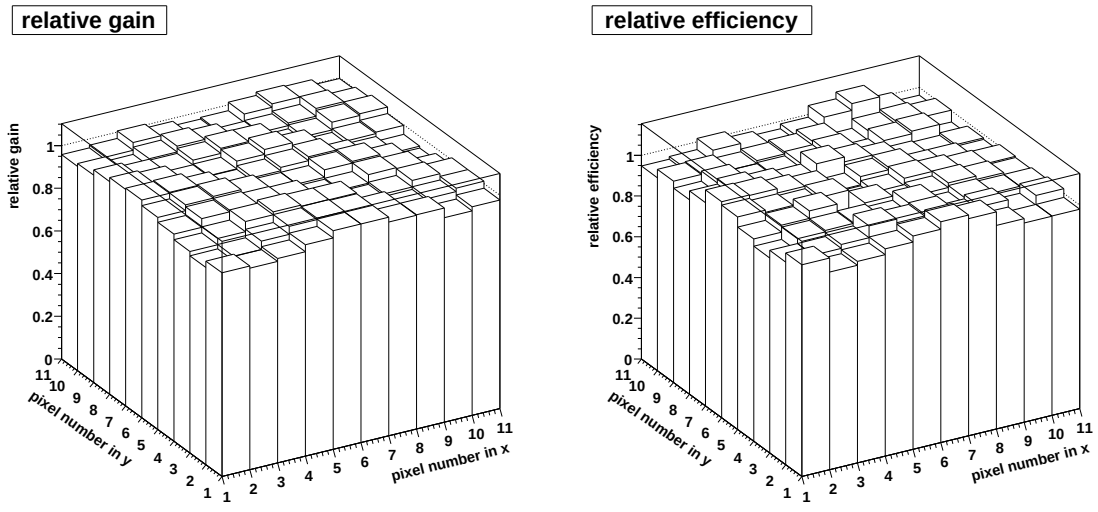

Figure 5.8: Pixel-to-pixel uniformity of gain (left) and efficiency (right) for a 100 pixel device.

The one dimension histograms of the pixel-to-pixel uniformity of gain and efficiency for a 100 (400) pixel device are also shown in Fig. 5.10 (5.11), respectively. From these figures the gain and efficiency are found to be uniform within 2.5% and 3.3% for the 100 pixel device, and 2.8% and 4.2% for the 400 pixel device in RMS/mean, respectively. The response of each pixel is quite uniform.

Figure 5.12 shows the pixel-to-pixel uniformity of cross-talk rate for 100 and 400 pixel devices. One can see from this figure that the cross-talk rate of the pixels at the edge of device is lower than that of the pixels around the center of device. It is qualitatively explained by the assumption that the cross-talk rate depends on the number of neighboring pixels.

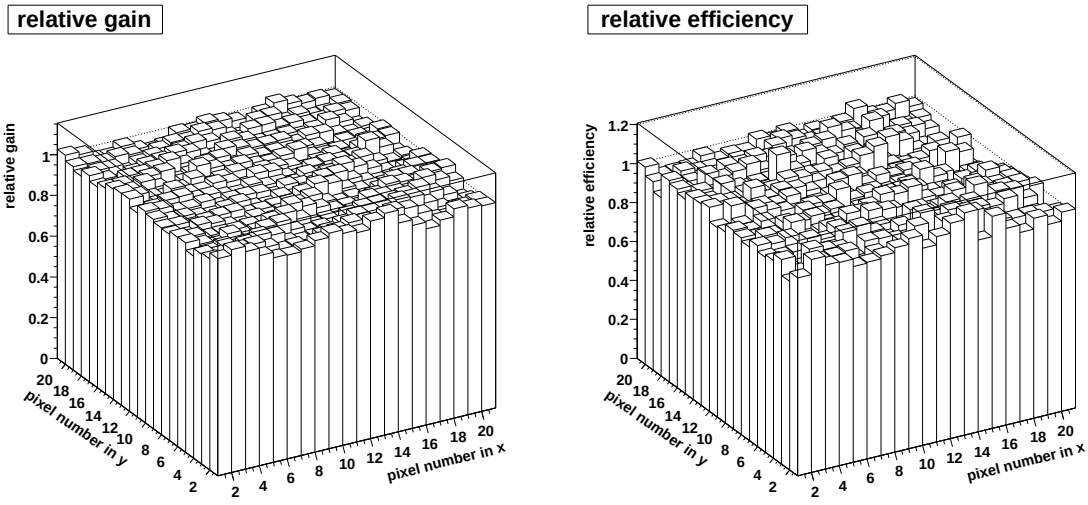

Figure 5.9: Pixel-to-pixel uniformity of gain (left) and efficiency (right) for a 400 pixel device.

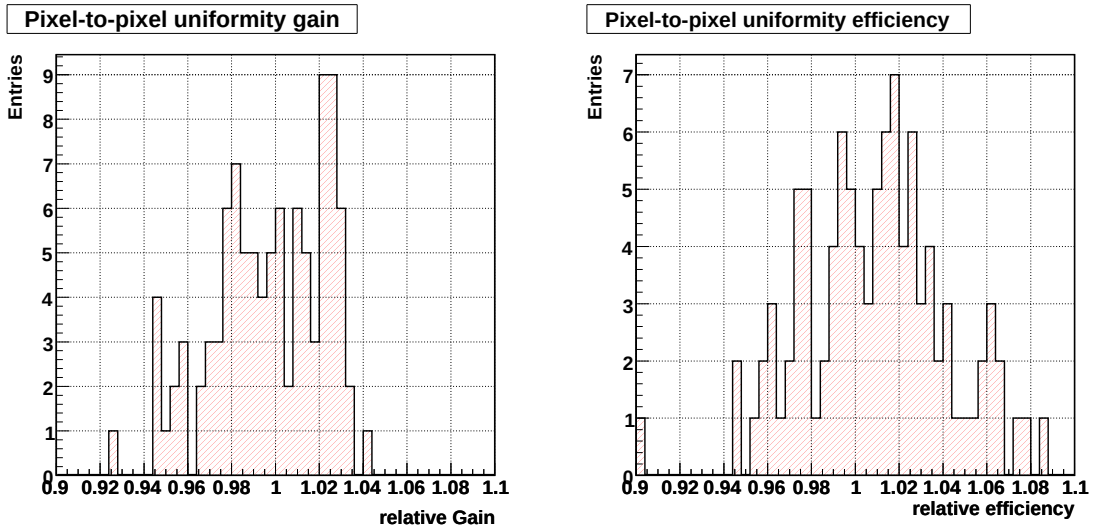

Figure 5.10: One dimension histograms of the pixel-to-pixel uniformity of gain (left) and efficiency (right) for a 100 pixel device.

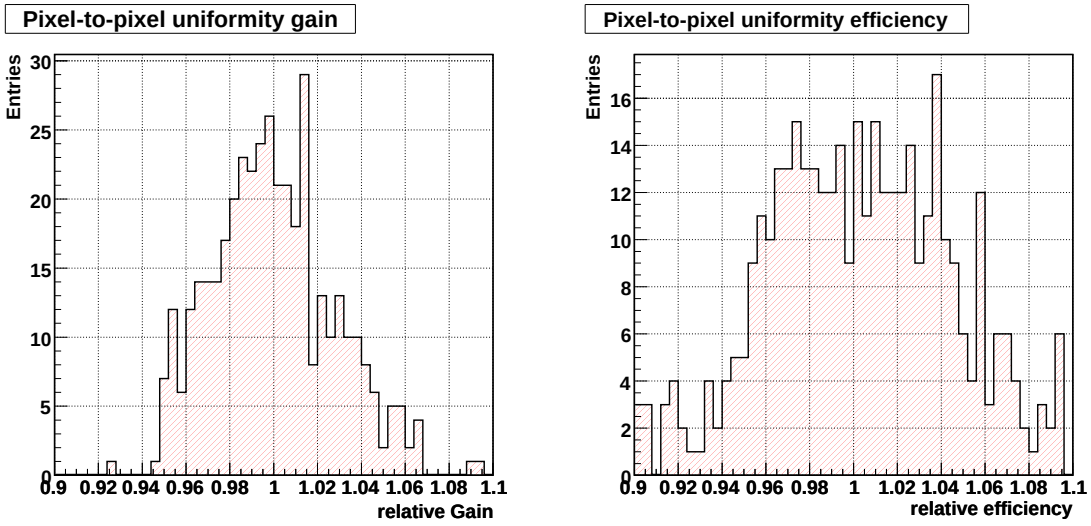

Figure 5.11: One dimension histograms of the pixel-to-pixel uniformity of gain (left) and efficiency (right) for a 400 pixel device.

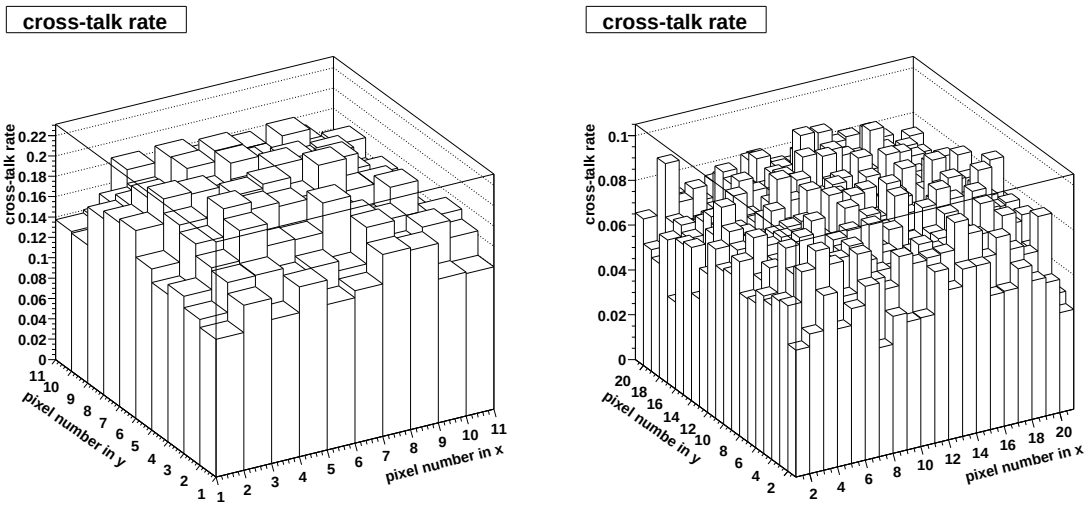

Figure 5.12: Pixel-to-pixel uniformity of cross-talk rate for 100 (left) and 400 (right) pixel devices.

5.3 Measurement of the active area inside one pixel

Next, we have measured the efficiency of 100 and 400 pixel devices by scanning the laser with 0.1 μm pitch in one dimension and estimated the fraction of the active area to the total area, which is defined as ϵ_{geom} in Eq. 4.4. The definition of efficiency is the same as that described in Section 5.1. The results are shown in Fig. 5.13. The active region is defined as the region from the center of the rise-up of the efficiency to the center of the fall-down of the efficiency. From these figures the fraction of the active area is found to be 49 (55)% for the 100 (400) pixel device, respectively. Here we assume the shape of the active area is a square. These values are consistent with that estimated from the picture taken by a microscope.

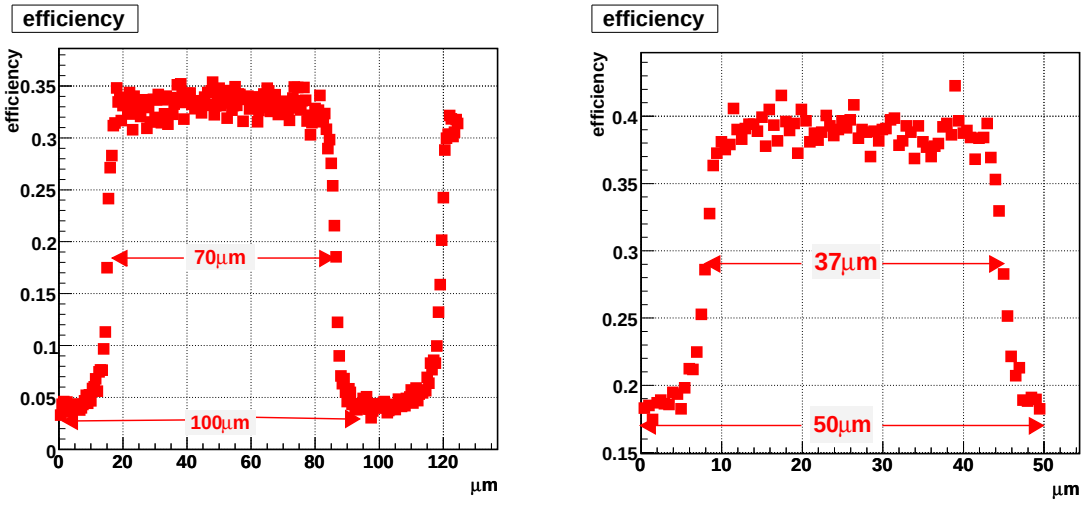

Figure 5.13: Efficiency of old 100 (left) and 400 (right) pixel devices measured by scanning the laser in one dimension.

We also show in Fig. 5.14 the measured efficiency of "latest" 100 and 400 pixel devices. One can see a slope of the measured efficiency in the active region within a pixel, but this is supposed to be due to a short-term instability of the laser intensity. The fraction of the active area is found to be 72 (58)% for the 100 (400) pixel device. For the old samples the 100 pixel device has smaller geometrical efficiency than the 400 pixel one. For the latest samples, however, the 100 pixel device have larger geometrical efficiency than the 400 pixel one. This results in a great improvement of PDE for the latest 100 pixel device.

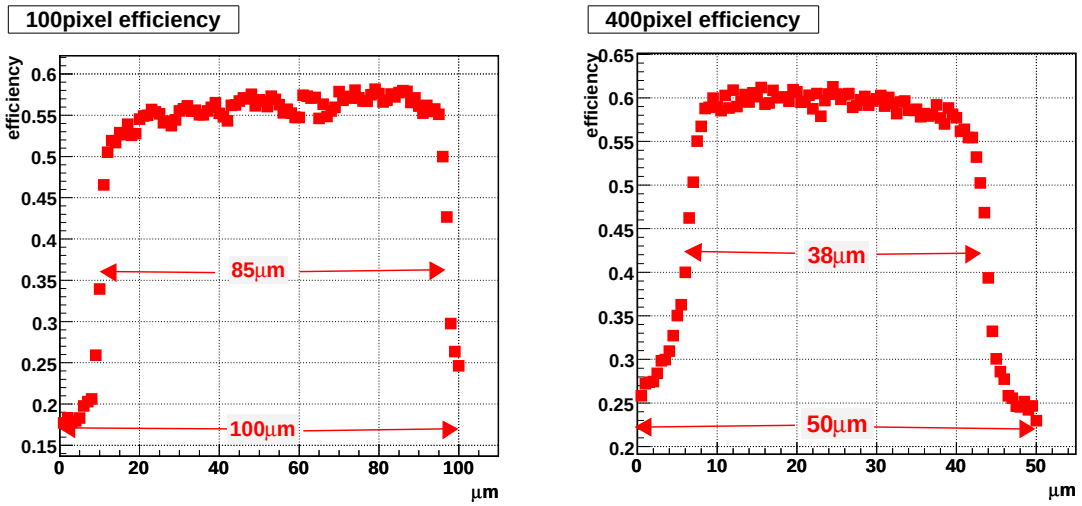

Figure 5.14: Efficiency of latest 100 (left) and 400 (right) pixel devices measured by scanning the laser in one dimension.

5.4 Summary and discussion

In this chapter we have shown the test with the laser injection system. We summarize the uniformity of gain and efficiency in Table 5.1.

Uniformity within one pixel		
Number of pixels	gain (RMS/mean)	efficiency (RMS/mean)
100	2.0%	2.0%
400	1.6%	1.7%
Pixel to pixel uniformity		
100	2.5%	3.3%
400	2.8%	4.2%

Table 5.1: Summary of the test with the laser injection system.

As for cross-talk rate, we have found two things:

- Cross-talk rate around the edge of the pixels is larger than that around the center of the pixels.
- Cross-talk rate of the pixels at the edge of device is smaller than that of the pixels around the center of device.

Moreover we have measured the fraction of the active area to the total area. For the old samples, it is 46% for a 100 pixel deivce and 55% for a 400 pixel one. For the latest samples, it is 72% for a 100 pixel device and 58% for a 400 pixel one.

Thus the latest 100 pixel sample has larger geometrical efficiency than that of the latest 400 pixel one.

Chapter 6

STUDY OF CORRECTION METHODS

6.1 Motivation

In this chapter we show the study of correction methods. The basic parameters of MPPC, which are gain, PDE and cross-talk rate, are all sensitive to temperature as described in Chapter 4. Because we do not know how much stability of the temperature is guaranteed in T2K now, it is necessary to study how to correct MPPC signal aiming at the real use at T2K. For the test of correction methods, we have traced MPPC signal for a Minimum Ionizing Particle (MIP) with the setup shown in Fig. 6.2. ADC counts for MIP are written as the following formula;

$$\text{ADC counts for MIP} \propto \text{gain}(\mathrm{V},\mathrm{T}) \times \text{PDE}(\mathrm{V},\mathrm{T}) \times \frac{1}{1-(\text{cross}-\text{talk rate}(\mathrm{V},\mathrm{T}))}, \tag{6.1}$$

where V is the applied voltage and T is the temperature. In this formula the term about the cross-talk rate is explained as follows [19]:

Assuming cross-talk occurs continuously with the same probability, a 1 p.e. signal looks larger by a factor of;

$$1 + \mathrm{c} + \mathrm{c}^2 + \mathrm{c}^3 + \cdots = \frac{1}{1-\mathrm{c}}, \tag{6.2}$$

where c is the cross-talk rate.

We can see from Formula 6.1 we have to monitor the variation of gain, PDE, and cross-talk rate in order to correct MPPC signal for MIP. We have evaluated the correction precision by two methods shown below, changing temperature intentionally between 20° and 25°C. In this test we have used the old samples delivered in Jan. 2006.

6.2 Correction method A

In this correction method, only gain (1 p.e. ADC counts) is monitored with illuminating MPPC by LED with low intensity. As for PDE and cross-talk rate, we know both of them are the function of only ΔV as discussed in Section 4.6 and 4.7. Because we can calculate the variation of ΔV by monitoring 1 p.e. ADC counts, it is possible to monitor PDE and cross-talk rate indirectly using the PDE - ΔV relation and the cross-talk rate - ΔV relation measured in advance. Finally we evaluate the correction precision by the variation of the calibration constant which is defined as;

$$\text{calibration constant} = \frac{\text{ADC counts for MIP}}{\text{1 p.e. ADC counts} \times \text{PDE} \times \frac{1}{1-(\text{cross-talk rate})}} \tag{6.3}$$

6.3 Correction method B

In this correction method MPPC is illuminated by LED with the similar intensity as MIP light yield. The light intensity of LED is monitored by the Si PIN photodiode (Hamamatsu S3590-08) whose temperature dependence is about $-0.05\%/^{\circ}$C and negligibly small. Because ADC counts for LED are also written as Formula 6.1, we can correct gain, PDE, and cross-talk rate together by taking the ratio of ADC counts for MIP to ADC count for LED. Finally we have evaluated the correction precision by the variation of the calibration constant which is defined as:

$$\text{calibration constant} = \frac{\text{ADC counts for MIP}}{\text{ADC counts for LED}} \tag{6.4}$$

The concepts of both correction methods are illustrated in Fig. 6.1.

6.4 Setup

We show the setup for the study of correction methods in Fig. 6.2. The extruded scintillators used in the K2K SciBar detector[20], 1.3 $\times$ 2.5 $\times$ 20 cm^3 in size, are put in four layers. A Kuraray Y11 wave length shifting fiber with the 1mm diameter is inserted into a hole at the center of the scintillator. The fibers are connected to four MPPCs (two are 400 and two are 100 pixel devices). The MPPC1 (100 pixel) and MPPC3 (400 pixel) are the devices whose temperature dependence of gain, PDE, and cross-talk rate are pre-measured. Figure 6.4 shows the drawing of the coupling part of the fiber and the MPPC. The transparent alignment fixture, "cookie" and the active area of the MPPC are aligned by eyes, and the cookie and the plate which is adjusted to be the same height as the

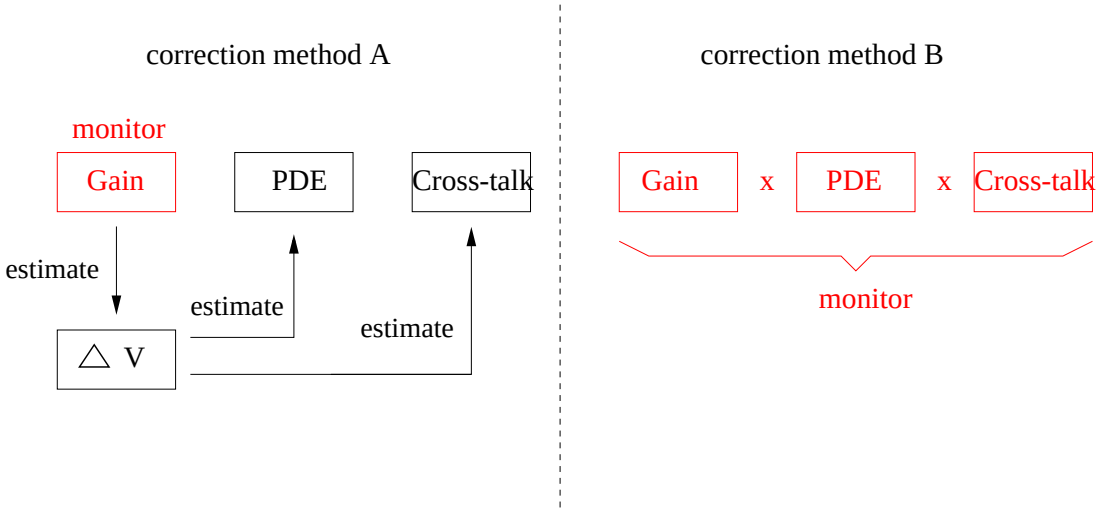

Figure 6.1: Illustration of the concepts of the correction method A (left) and B (right). In the correction method A, we derive the variation of cross-talk rate and PDE by monitoring only gain using the ΔV dependence measured in advance. In the correction method B, we correct gain, cross-talk rate and PDE at once by taking the ratio of ADC counts for cosmic-ray muons to that for LED.

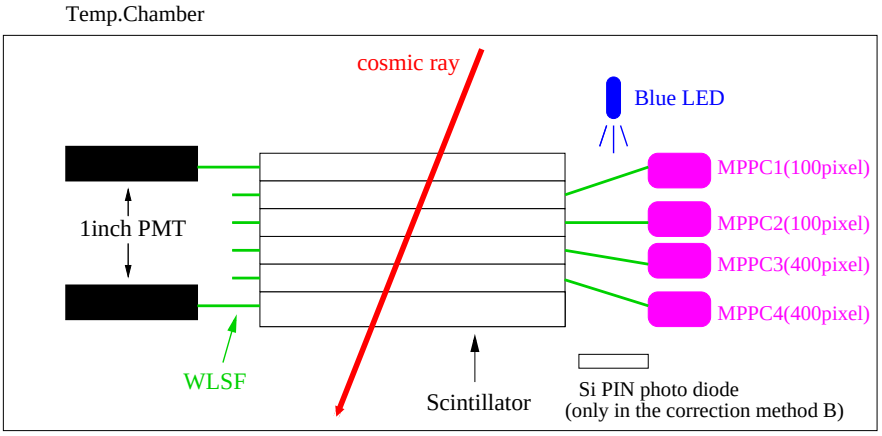

Figure 6.2: Schematic of the setup for the study of correction methods. The extruded scintillators are put in four layers. The inserted fibers into the scintillators are connected to four MPPCs. The setup is put into a temperature-controlled chamber and the temperature is intentionally changed between 20°C and 25°C every 12 hours.

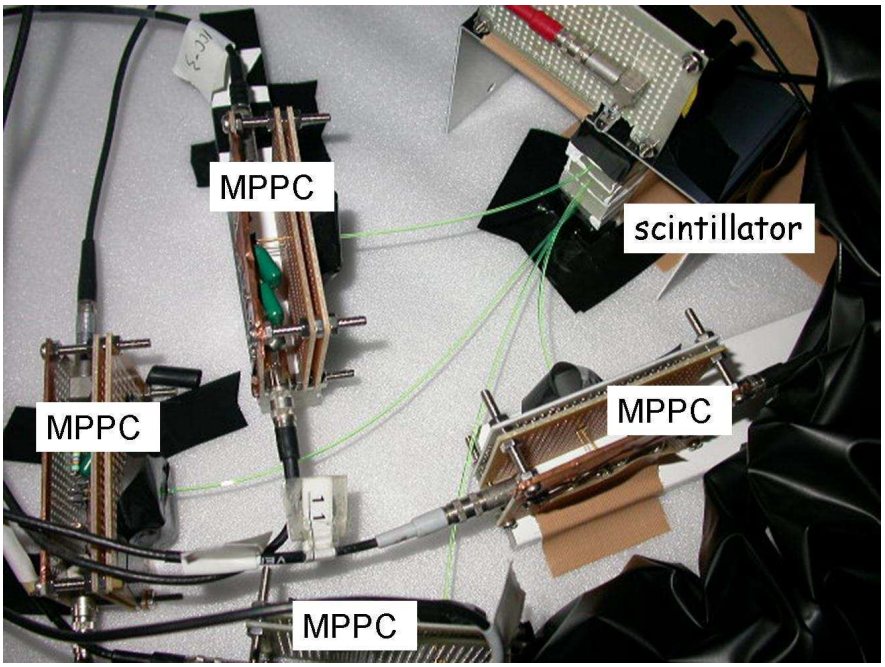

Figure 6.3: Photograph of the setup for the study of correction methods.

MPPC are glued by optical cement. This method is rather crude and the loss of light yield due to the misalignment of the fiber to the MPPC is actually observed. However this misalignment is not a problem because an interesting matter in this measurement is a relative change of light yield for cosmic-ray muons. The size of the trigger counters are same as that of the tested scintillator, but the diameter of the inserted fibers is 1.5 mm. The fibers are connected to 1 inch PMTs. This setup is put in the temperature-controlled chamber and the temperature is changed intensionally between 20°C and 25°C during the test. The photograph of the setup is shown in Fig. 6.3.

The diagram of the data acquisition system for this measurement is shown in Fig. 6.5. There are three independent triggers in this setup, which are the LED, pedestal, and cosmic triggers. The LED and pedestal triggers are generated in turn with a rate of 1 Hz. The cosmic trigger is made by the coincidence of the signals from the two trigger counters. In order to identify the type of triggers, each trigger signal goes to a time-to-digital converter (TDC). The rate of the cosmic trigger is about 0.1 Hz.

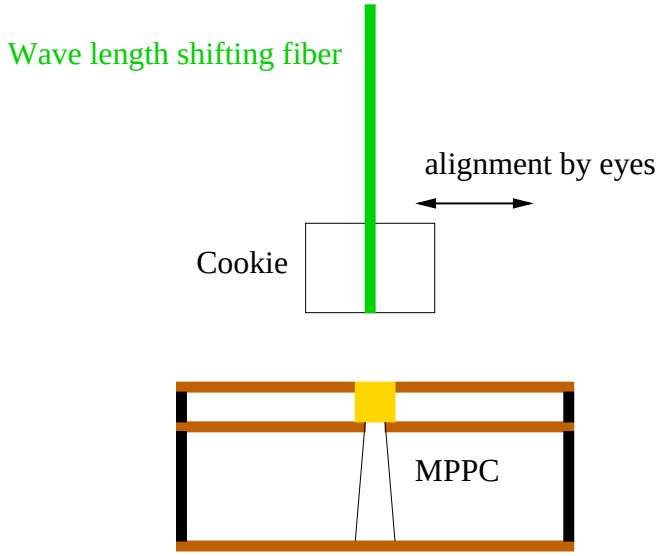

Figure 6.4: Drawing of the coupling part of the MPPC and the wave length shifting fiber. The active area of the MPPC and the fiber which is fixed with a cookie are aligned by eyes and glued by optical cement.

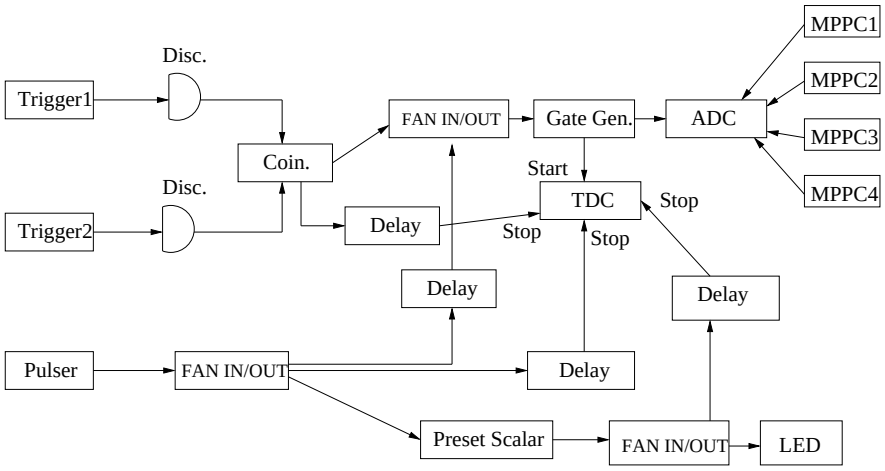

Figure 6.5: Diagram of the data acquisition system for the study of correction methods.

6.5 Results

6.5.1 Light yield distribution

Figure 6.6 shows light yield distributions of four MPPCs for MIP at 20°C. The upper two figures correspond to the 100 pixel devices and lower two correspond to the 400 pixel devices. The same bias voltage is applied to four MPPCs. The light yield shown in the lower left figure (MPPC3), is much smaller than that of the others. The low light yield of the MPPC3 is due to the misalignment of the fiber to the MPPC because the PDE of MPPC3 is found to be about the same as that of the others by a pre-measurement. ADC counts for MIP are defined as the peak ADC counts of the light yield distribution which is calculated from the Gaussian fitting around the peak.

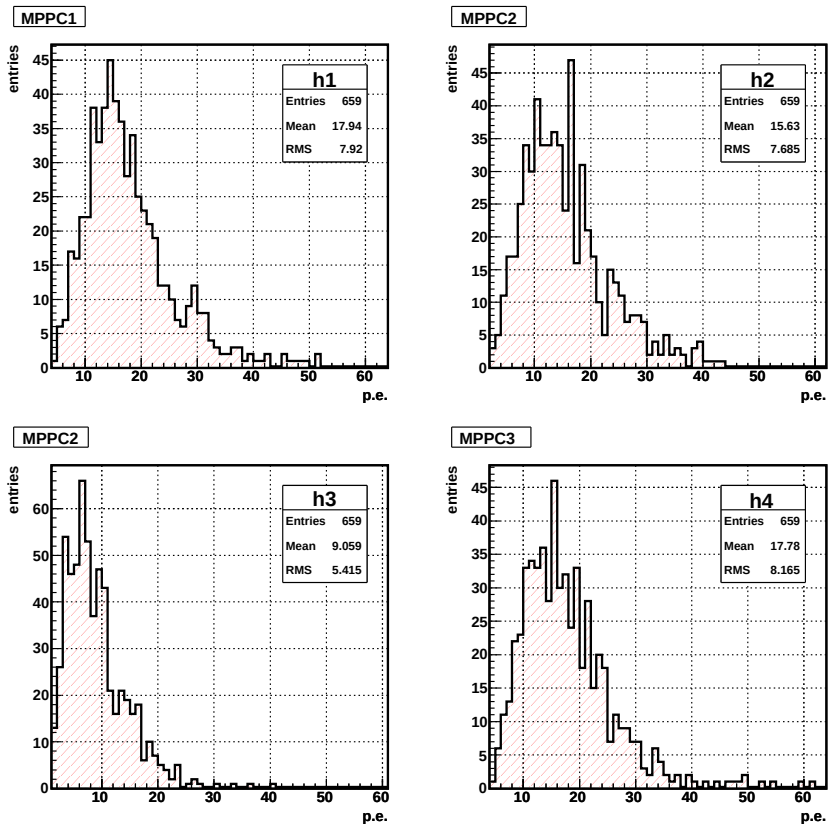

Figure 6.6: Light yield distributions of four MPPCs for MIP at 20°C. The upper (lower) two figures correspond to the 100 (400) pixel devices.

6.5.2 Results with correction method A

In this subsection we discuss the correction method A. We show the time variation of 1 p.e. ADC counts (blue points) and ADC counts for MIP (red points) in Fig. 6.7. We can see from Fig. 6.7 that the time variation of 1 p.e. ADC counts and ADC counts for MIP are similar.

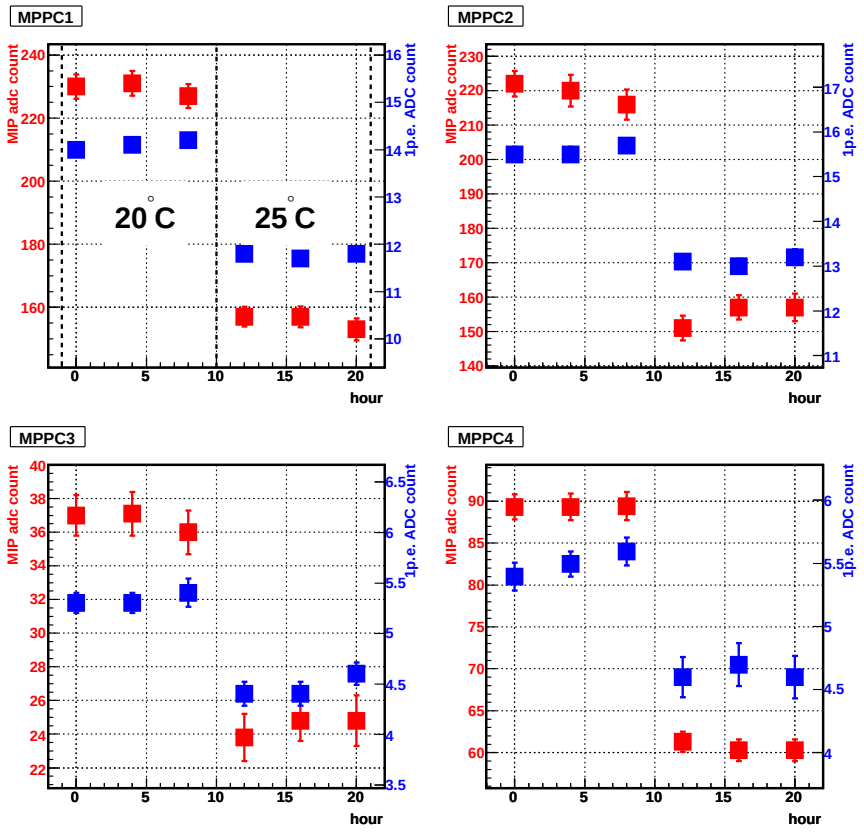

Figure 6.7: Time variation of 1p.e. ADC counts (blue points) and ADC counts for MIP (red points). The upper (lower) two figures correspond to the 100 (400) pixel devices.

In order to correct the variation of PDE and cross-talk rate, we show in Fig. 6.8 the time variation of ΔV calculated from the time variation of 1 p.e. ADC counts shown in Fig. 6.7 and the pre-measured gain - ΔV relation.

Next, Fig. 6.9 shows the time variation of PDE which is calculated from the estimated variation of ΔV shown in Fig. 6.8 and the pre-measured PDE - ΔV relation. Fig. 6.10 also shows the time variation of cross-talk rate, which is calculated from the estimated variation of ΔV shown in Fig. 6.8 and the pre-measured cross-talk rate - ΔV relation. The same correction functions for PDE and cross-talk rate as the MPPC1 and MPPC3 are applied to the MPPC2 and

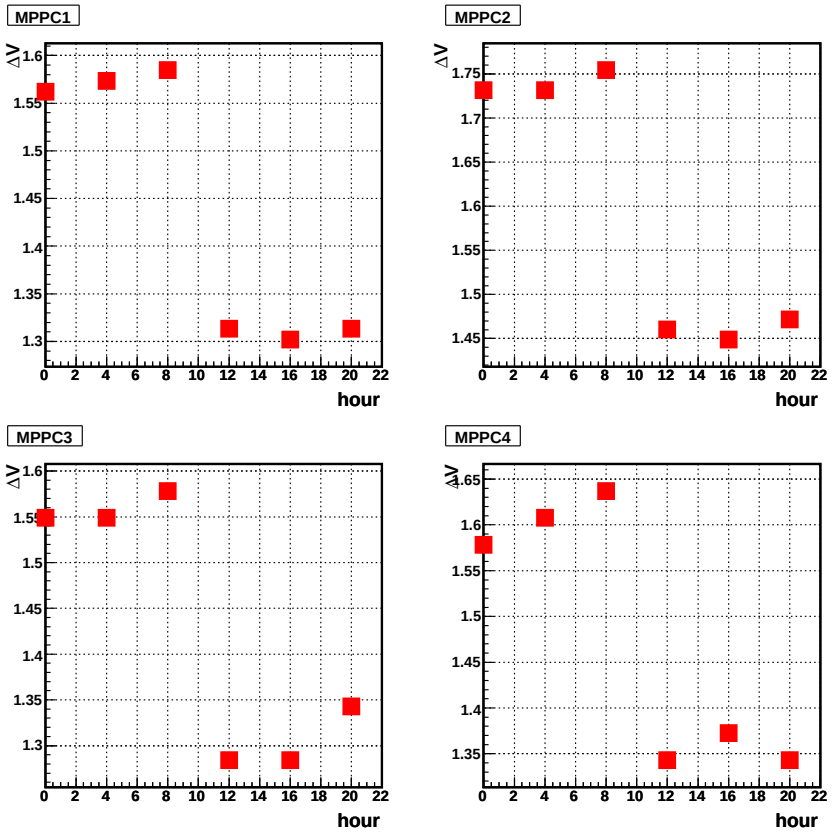

Figure 6.8: Time variation of ΔV calculated from the time variation of 1 p.e. ADC counts shown in Fig. 6.7 and the pre-measured gain - ΔV relation. The upper (lower) two figures correspond to the 100 (400) pixel devices.

MPPC4, respectively.

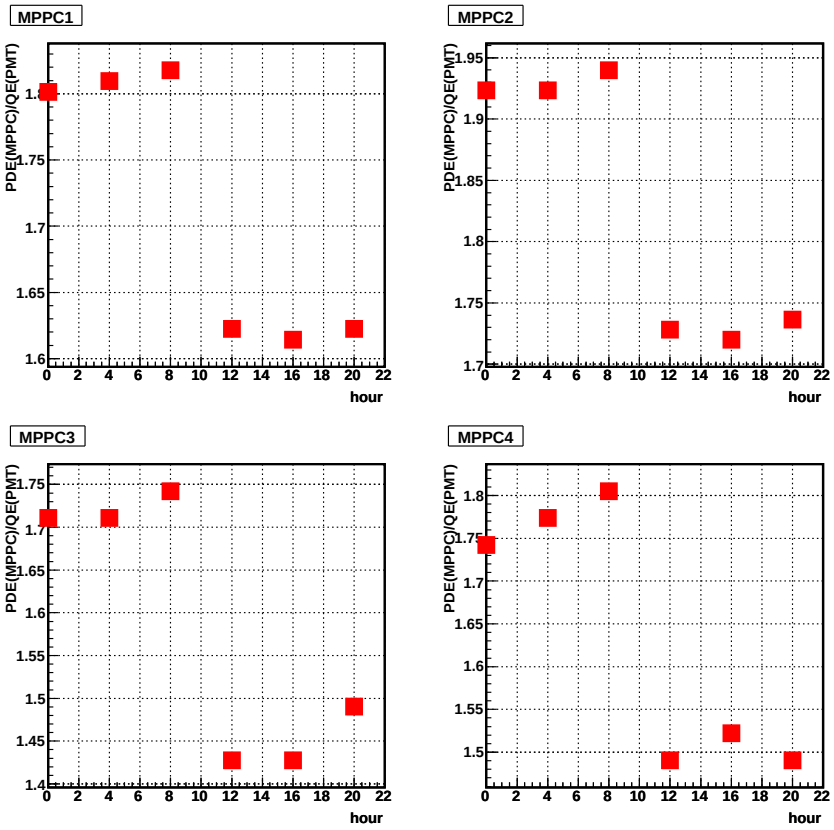

Figure 6.9: Time variation of PDE calculated from the time variation of ΔV shown in Fig. 6.8 and the pre-measured PDE - ΔV relation. The upper (lower) two figures correspond to the 100 (400) pixel devices.

Using the time variation of 1 p.e. ADC counts shown in Fig. 6.7 and the estimated correction factors for PDE and cross-talk rate shown in Fig. 6.9 and 6.10, the time variation of the calibration constant is shown in Fig. 6.11.

The $\pm$3% deviation lines from the mean are also shown in Fig. 6.11. We can see from this figure the detector response is well corrected within about 3% precision after the corrections of gain, PDE, and cross-talk rate. Table 6.1 shows the time variation of light yield for MIP (RMS/mean) after the corrections of only gain, gain + PDE, and gain + PDE + cross-talk rate. The variation becomes the smallest after the corrections of all of the gain, PDE and cross-talk rate for all MPPCs. From this result we can see the corrections of PDE and cross-talk rate by monitoring the variation of gain are successful.

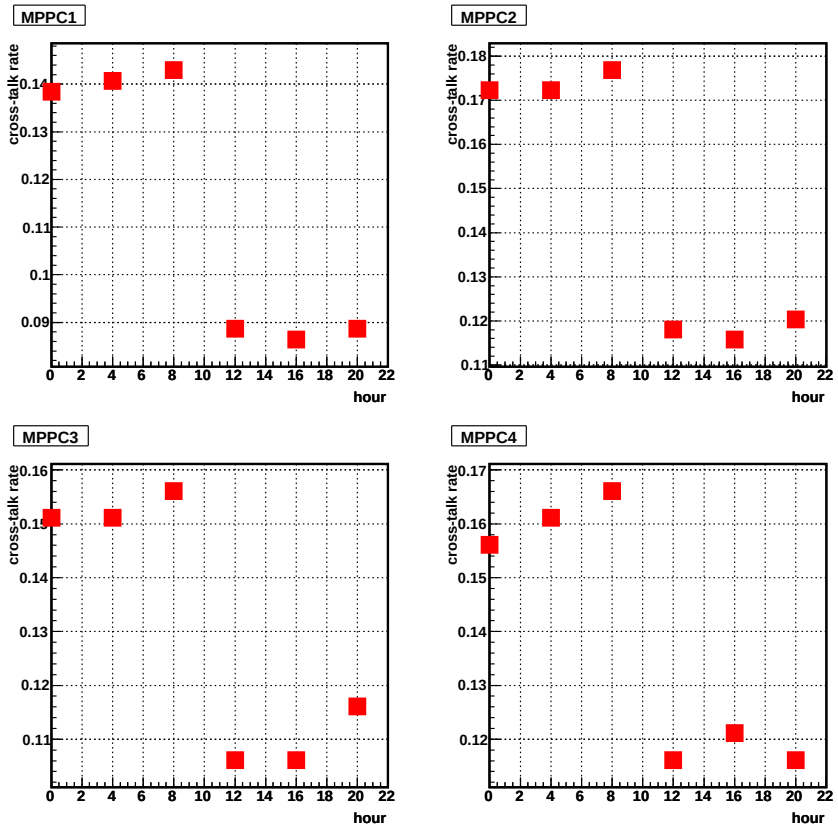

Figure 6.10: Time variation of cross-talk rate calculated from the time variation of ΔV shown in Fig. 6.8 and the pre-measured cross-talk rate - ΔV relation. The upper (lower) two figures correspond to the 100 (400) pixel devices.

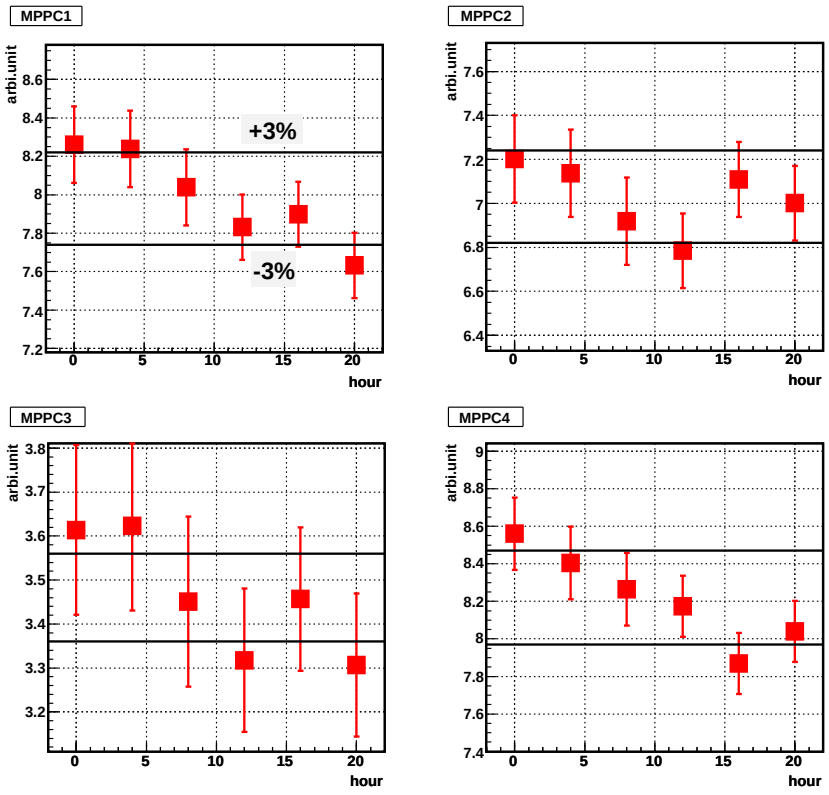

Figure 6.11: Time variation of the calibration constant calculated from the measured time variation of 1 p.e. ADC counts shown in Fig. 6.7 and the estimated correction factors for PDE and cross-talk rate shown in Fig. 6.9 and 6.10. The upper (lower) two figures correspond to the 100 (400) pixel devices. The ±3% deviation lines from the mean are also showed. The errors of 1 p.e. ADC counts and ADC count for MIP are considered for error bars.

	MPPC1(100)	MPPC2(100)	MPPC3(400)	MPPC4(400)
No correction	19.1%	17.3%	19.0%	19.1%
Gain	10.4%	8.8%	11.5%	10.8%
Gain, PDE	5.0%	3.8%	4.4%	3.7%
Gain, PDE, cross-talk	2.5%	2.3%	3.8%	3.1%

Table 6.1: Time variation of light yield for MIP (RMS/mean) after the corrections of gain, gain + PDE, and gain + PDE + cross-talk rate.

6.5.3 Results with correction method B

In this section we discuss the correction method B. The test of the correction method B has been done independently from that of the correction method A. We show the time variation of ADC counts for MIP in Fig. 6.12 and ADC counts for LED in Fig. 6.13. ADC counts for LED are corrected by the variation of the light intensity of LED measured by the Si PIN photodiode. The time variation of the calibration constant calculated from these figures is shown in Fig. 6.14. The $\pm 3\%$ deviation lines from the mean are also shown. We can see from this figure the detector response is also well corrected within about 3% precision with the correction method B.

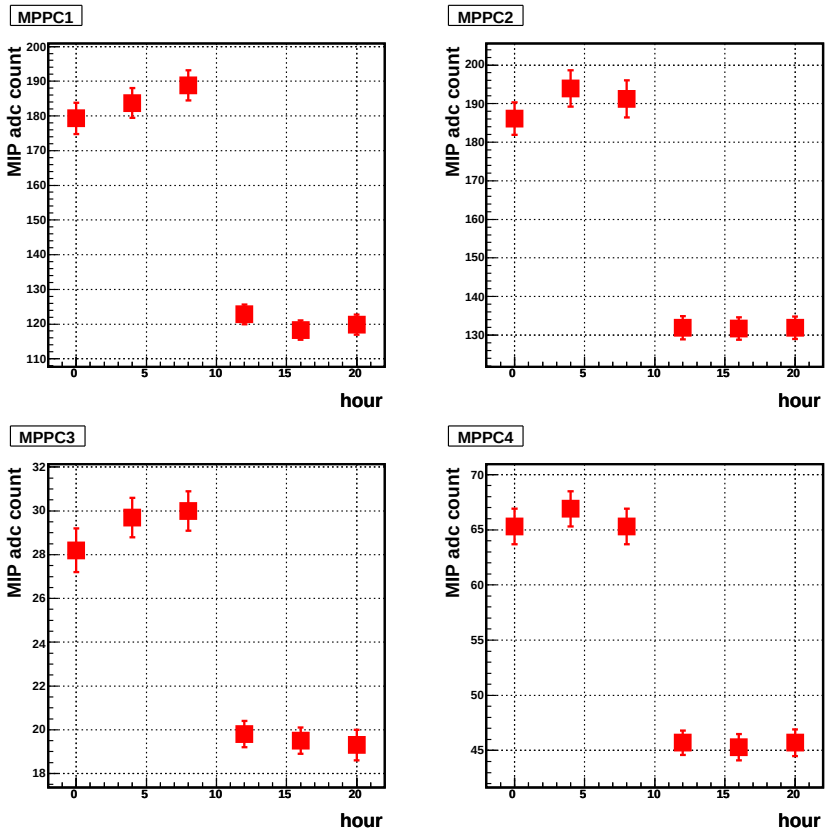

Figure 6.12: Time variation of ADC counts for MIP. The upper (lower) two figures correspond to the 100 (400) pixel devices.

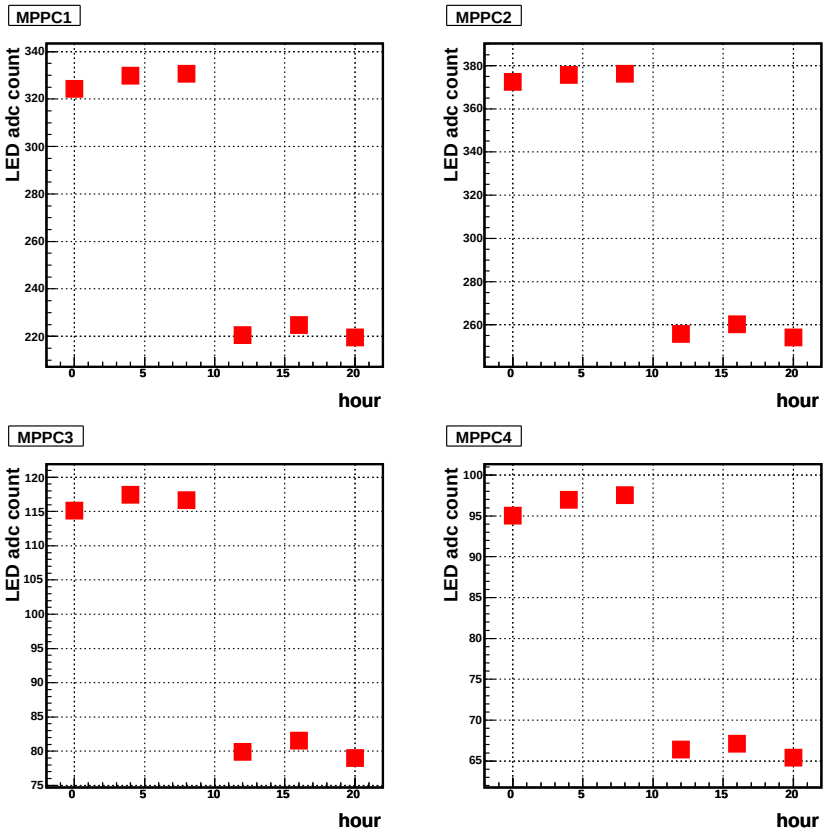

Figure 6.13: Time variation of ADC counts for LED. The upper (lower) two figures correspond to the 100 (400) pixel devices.

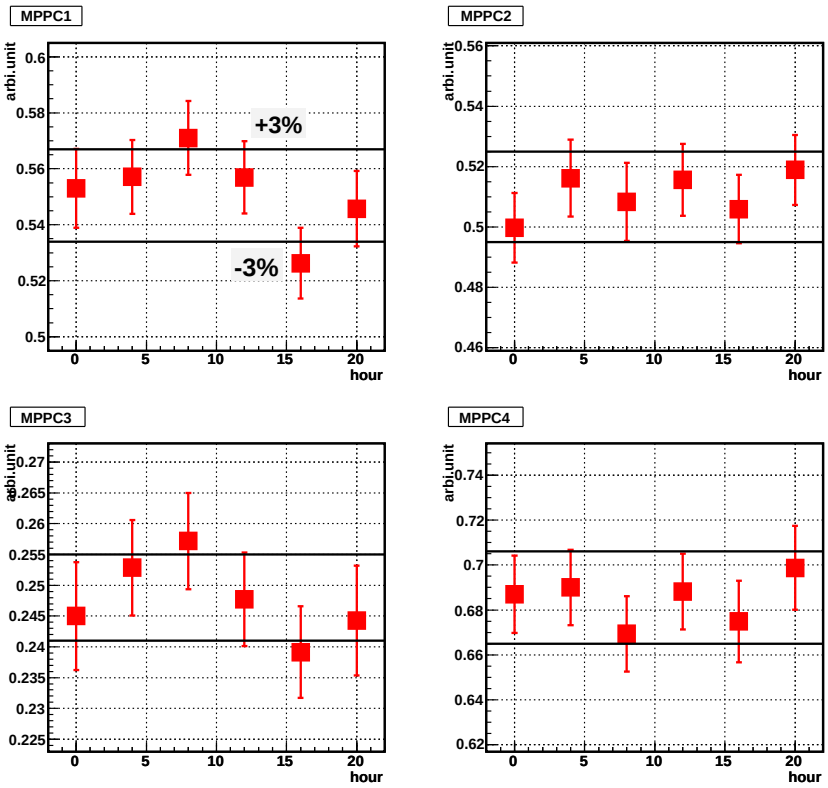

Figure 6.14: Time variation of the calibration constant calculated from the time variation of ADC counts for MIP and ADC counts for LED shown in Fig. 6.12 and Fig. 6.13, respectively. The upper (lower) two figures correspond to the 100 (400) pixel devices. The ±3% deviation lines from the mean are also showed. The error bars are calculated from the errors of ADC counts for MIP and ADC counts for LED.

6.6 Summary and discussion

Correction method	MPPC1(100)	MPPC2(100)	MPPC3(400)	MPPC4(400)
A	2.5%	2.3%	3.8%	3.1%
B	2.5%	1.3%	2.4%	1.4%

Table 6.2: Correction precision for each device in RMS/mean.

Table 6.2 shows the correction precision for each device in RMS/mean. The correction precision is found to be within about $\pm 3\%$ after the corrections of gain, PDE, and cross-talk rate for all MPPCs even if the temperature changes by 5°C (The correction precision is better for the method B). This level of the correction precision is satisfactory for T2K. The number of tested samples is limited, however the test with the much larger number of samples will be done in the near future. Here we want to mention the following:

- Correction method A
  - In order to correct the variation of PDE and cross-talk rate, it is necessary to measure gain - ΔV, PDE - ΔV, and cross-talk rate - ΔV relation in advance. These relations are measured by changing only bias voltage. We do not have to measure the temperature dependence, but long term stability of these relations need to be studied.
  - We have shown that we can apply the same correction functions for PDE and cross-talk rate to the same type of MPPC. The sampling measurement may be enough for the same type of MPPC. This is because the device-by-device variation of a basic parameter comes from the device-by-device variation of the breakdown voltage, as shown in Chapter 4.
  - We have monitored gain with illuminating MPPC by LED, but it is also possible to monitor the gain with noise distribution taken by a random-trigger. In that case the construction of the setup will be simpler.
- Correction method B
  - We have to guarantee the stability of LED light intensity and distribute the light from LED to MPPC. In this case the construction of the setup will be more complicated than the correction method A.

The choice of correction methods will depend on each sub-detector in ND280. Of course it will be possible to use both correction methods for redundancy.

Chapter 7

TRIP-T

From this chapter we present the study of the readout electronics of MPPC using Trip-t.

7.1 Introduction

Trip-t[1] (Figure. 7.1) is an ASIC (Application Specific Integrated Circuit) which was developed at Fermilab. The number of input channels of Trip-t is 32. The injected charge to each channel is amplified by front-end amplifiers and stored in a pipeline before readout. The depth of the pipeline is programmable from 1 to 48. Next the stored signals are serialized to one channel by a multiplexer which is located at the last stage of Trip-t. Using one Trip-t, we can reduce the number of readout channels from 32 to 1. There are three kinds of outputs for Trip-t.

- A_OUT : Serialized analog signal of 32 channel inputs that is proportional to the amplitude of input charge.
- T_OUT : Serialized analog signal of 32 channel inputs that is proportional to the time between the firing of a discriminator and the closing of a time-gate.
- D_OUT : Discriminated digital signal for each input.

Simply speaking, A_OUT corresponds to the amplitude of input charge, T_OUT corresponds to the timing of input charge and D_OUT corresponds to the digital information of input charge. There are fourteen parameters which determine the operation status of Trip-t and they can be controlled by programming the registers. We explain the programming of registers in Appendix E. Trip-t has been used for the VLPC (Visible Light Photon Counter) detector[2] at the DØ experiment [21] and will be used at the MINERνA experiment [22].

[1] Trip-t is the abbreviation of TRIgger and Pipeline with Timing.

[2] VLPC is a silicon photodiode for detecting the light from a fiber. It operates near the temperature of 6.5 K.

The specification of the Trip-t chip is shown in Table 7.1. Trip-t does not almost have the dynamic range for positive charge. We study the performance of Trip-t with the test board shown in Fig. 7.2. The number of input channels for this test board is five, one for the gain calibration of Trip-t and four for MPPCs. These inputs can be seen at the left side of the board. The connector at the right side of the board is used for injecting the control signals of Trip-t from a digital wave generator.

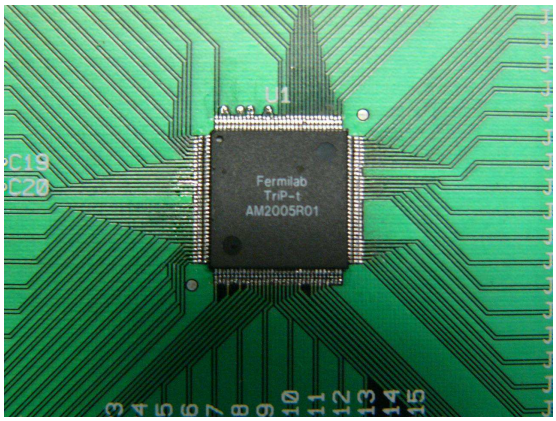

Figure 7.1: Photograph of the Trip-t chip. The size of the chip is 14 mm $\times$ 14 mm and there are 128 pins in total.

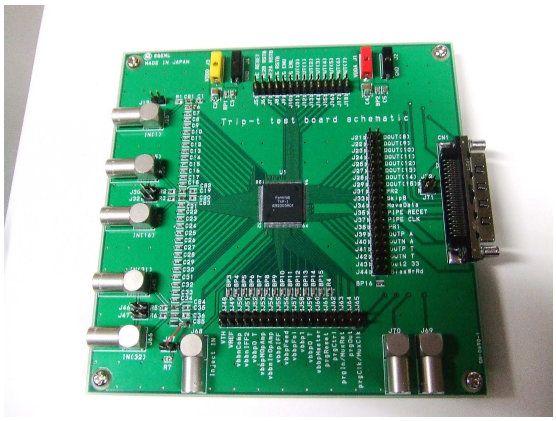

Figure 7.2: Photograph of the test board. The number of inputs are five, one for the gain calibration of Trip-t and four for the readout of MPPCs.

This chapter consists of the following sections;

- Section 7.2 :

  In this part we give a detail description of Trip-t.

Power supplies	VDDD (digital) = +2.5 V, VDDA (analog) = +2.5 V
Dynamic range	−100 fC (with the highest gain), −3,000 fC (with the lowest gain)
Power consumption	< 10 mW per channel
Size	14 mm × 14 mm

Table 7.1: Specification of the Trip-t chip.

- Section 7.3 :

  In this section we show the basic performance of Trip-t measured with our test board.

- Section 7.4 :

  In this section we summarize the contents of this chapter.

7.2 Schematic of Trip-t

We show the simplified functional diagram of Trip-t in Fig. 7.3. Trip-t mainly consists of three parts, which are a front end, an analog pipeline, and a multiplexer. In the following subsections we explain each part in detail.

7.2.1 Front end

The front end part plays roles of

- amplifying injected signal and shaping it, which the analog pipeline samples
- generating discriminated signals with the programmable threshold value

Figure. 7.4 shows the simplified schematic of the front end part. At the first stage the injected signal is amplified at the preamp by one or four times, which can be selected by programing the register GAIN (preamp gain). The feedback resistor of the preamp is changed by the register IFF. Next the amplified signal goes to the opamp A whose gain is also changed by the register GAIN, like ×1, ×2, ×4 ⋯ ×16 (opamp gain). Hereafter we denote the gain setting of the preamp gain ×1 and the opamp gain ×4 as (×1,×4), for example. This amplified signal is sent to the analog pipeline and results in A_OUT finally. The signal amplified at the preamp also goes to the fixed gain (×10) opamp B, and discriminated by a comparator. The threshold value is changed by the register V_TH. One of the discriminated signal results in D_OUT and the other goes to the next opamp. The switch of this opamp is controlled by the "PIPE_CLK" signal. The time difference between the discriminated signal and the rising edge of "PIPE_CLK"

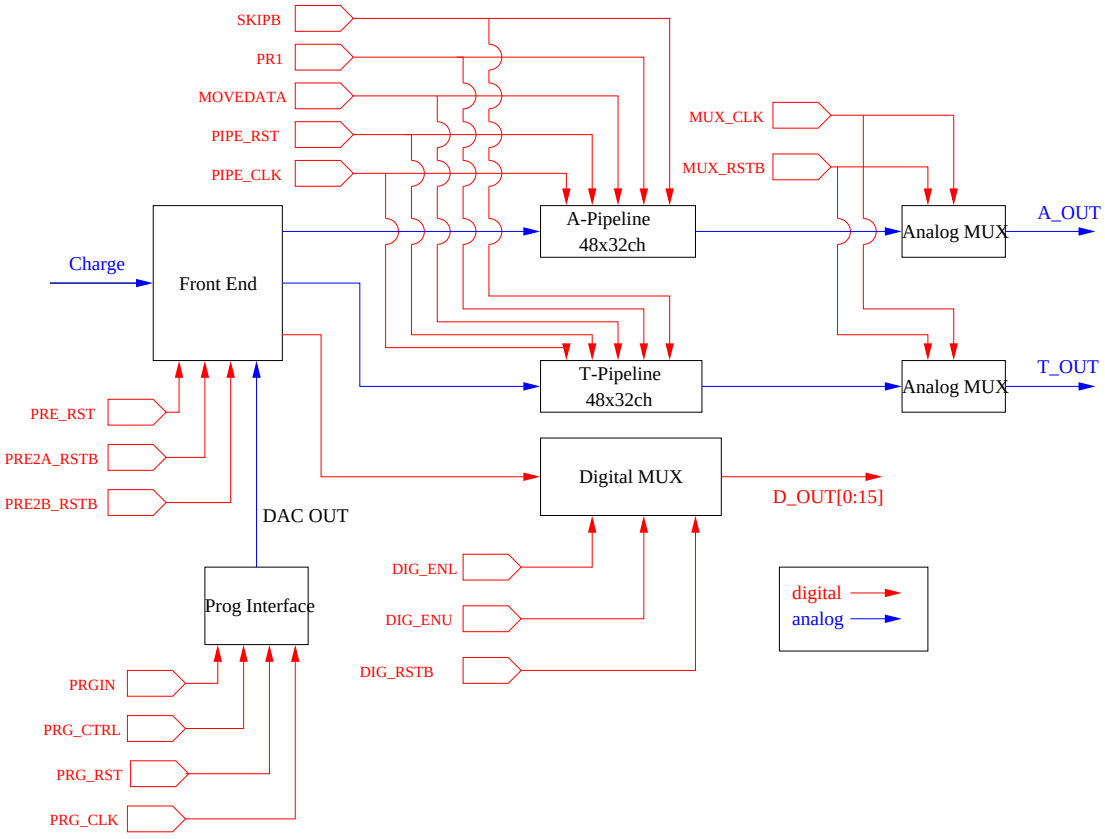

Figure 7.3: Simplified functional diagram of Trip-t. A Red arrow shows a digital signal, and a blue one shows an analog signal. The meaning of each control signal in this figure is shown in Table E.1.

is converted to the charge information and sent to the analog pipeline. This corresponds to T_OUT.

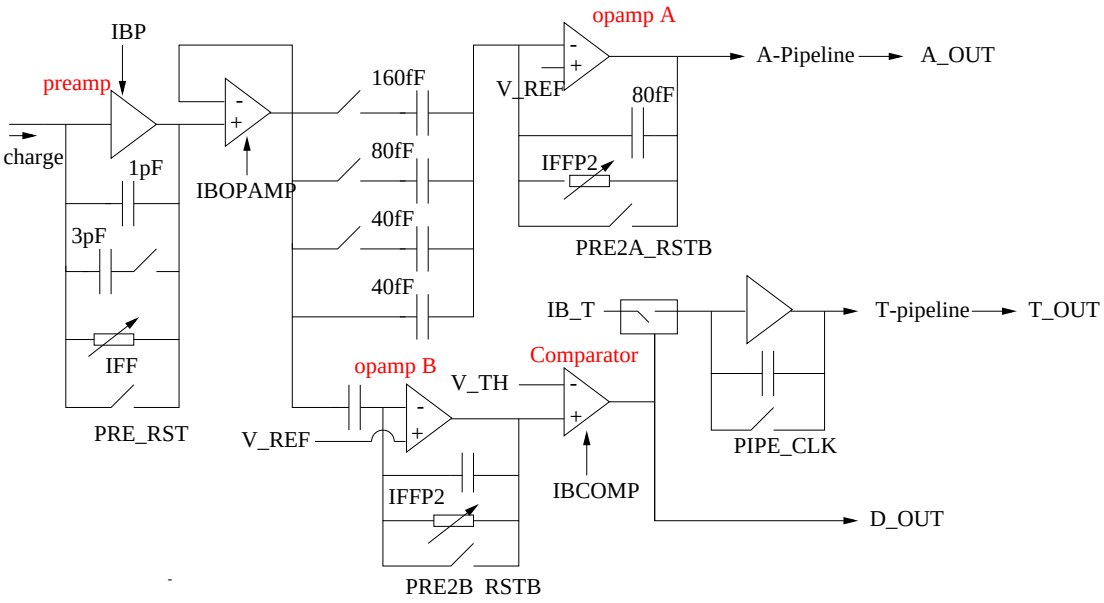

Figure 7.4: Simplified schematic of the front end part. The gain of the preamp and the opamp is adjustable by programming the registers.

7.2.2 Analog pipeline

Trip-t has the analog pipeline with the depth programmable from 1 to 48 for each input. We can store signal in each pipeline cell before the readout. The schematic of the analog pipeline is shown in Fig. 7.5. The pipeline is controlled by "PIPE_CLK". A given cell is reset while "PIPE_CLK" is high, takes the first sample of output from the front end when the clock goes low, and takes the second sample when the clock goes back high, which also advances the pipeline to the next cell.

7.2.3 Multiplexer

The 32 channel signals stored in the pipeline are read out by an analog multiplexer. This readout is clocked by "MUX_CLK". The number of clocks is 34. The first clock corresponds to the internal channel which has no external access to the input, the 2 $\sim$ 33 th clocks the channels of interest, and the 34 th clock the test channel. At the rising edges of "MUX_CLK", the stored charge in each pipeline cell is converted to the voltage information and serialized to one channel, which results in A_OUT or T_OUT. The schematic of the multiplexer is shown in Fig. 7.6.

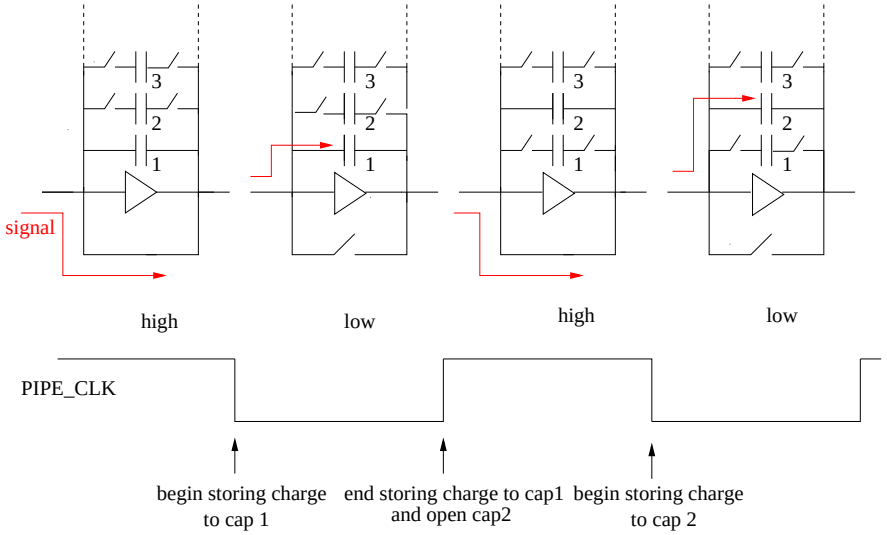

Figure 7.5: Schematic of the analog pipeline. A given cell is reset while "PIPE_CLK" is high, takes the first sample of output from the front end when the clock goes low, and takes the second sample when the clock goes back high, which also advances the pipeline to the next cell.

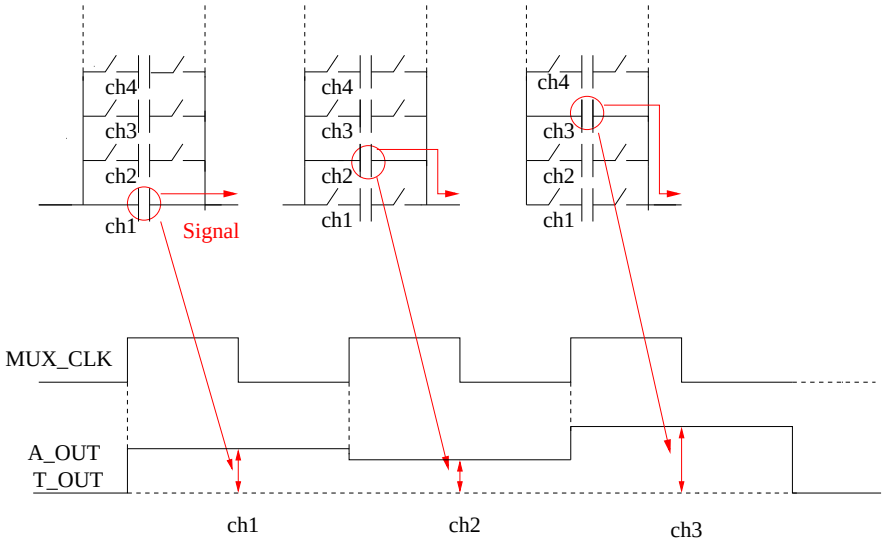

Figure 7.6: Schematic of the multiplexer. At the rising edges of "MUX_CLK", the signals stored in each pipeline cell are serialized to one channel.

7.3 Basic performance of Trip-t

We studied the basic performance of Trip-t by injecting the charge to an input of Trip-t. The setup is shown in Fig. 7.7 and the instruments for this measurement are summarized below;

- Digital wave generator : National Instruments PXI-6551

  The maximum clock rate is 100 MHz and the voltage level is adjustable from -2.0 V to 5.5 V. The number of output channels is 20.

- Attenuator : Kaizu works KN320

  The attenuation level is $0 \sim 31$ dB.

- Power supply : KIKUSUI PMM35-1.2DU

  The maximum output voltage is +35 V and the maximum output current is +2.5 A.

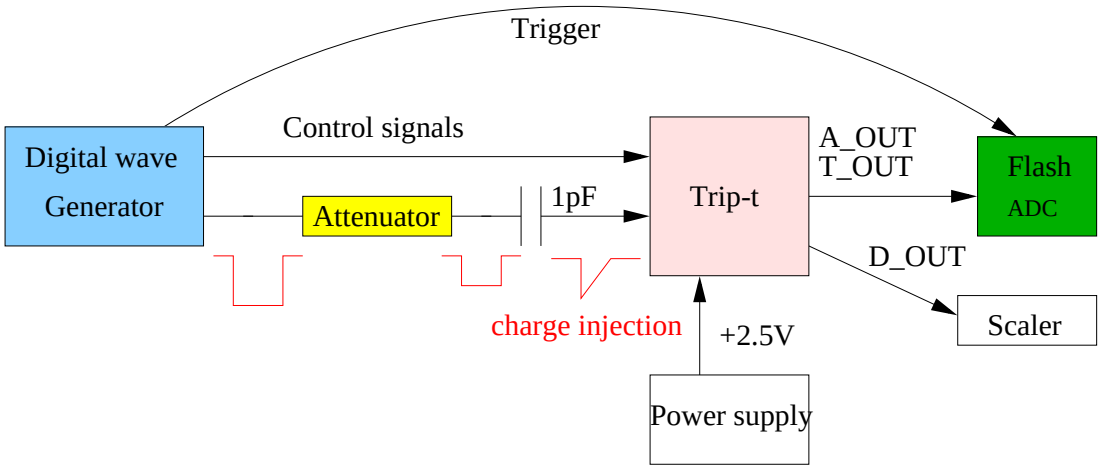

Figure 7.7: Setup for the measurement of the basic performance of Trip-t. The test charge is injected from a digital wave generator through a 1 pF capacitor. The control signals of Trip-t are also provided by the digital wave generator. The output from Trip-t is digitized by a flash ADC.

The test charge is injected from the digital wave generator through a 1 pF capacitor to an input of Trip-t. The amount of the test charge is changed by an attenuator with the attenuation level of $0 \sim 31$ dB. We also inject the control signals which are listed in Table E.1 from the digital wave generator. The timing sequence of the control signals is shown in Fig. E.1. The logic level of the control signals is 2.5 V and the frequency of the multiplexer clock is set to be 1 MHz. The output of Trip-t (A_OUT or T_OUT) is converted to the digital information by a

flash ADC. We explain the AD conversion of Trip-t output in detail in Chapter 8.

7.3.1 A_OUT (Amplitude of the input charge)

Figure 7.8 shows the A_OUT taken by an oscilloscope. A blue line is A_OUT, a sky blue line is "MUX_CLK" and a pink line is "MUX_RSTB". The charge is injected to the channel 1, which is -1.4 pC in the left figure and -0.5 pC in the right one. The gain setting is ($\times 1$, $\times 4$) corresponding to the preamp gain of 1 and the opamp gain of 4. We see A_OUT at the second "MUX_CLK" which corresponds to the channel 1 and the amplitude of A_OUT in the left figure is larger. The A_OUT has a 1.0 V DC offset. Next, we show in Fig. 7.9 the amplitude of A_OUT as a function of the injected charge with the three gain settings. The amplitude of A_OUT is taken as the mean value of the ADC distribution for 10000 events. Green points correspond to the gain setting of ($\times$ 4, $\times$ 2), red points ($\times 4$, $\times 1$) and pink points ($\times 1$, $\times 4$). The deviation from the linear extrapolation is also shown in Fig. 7.9. The linearity of the ADC is guaranteed. Here we want to mention the following three issues;

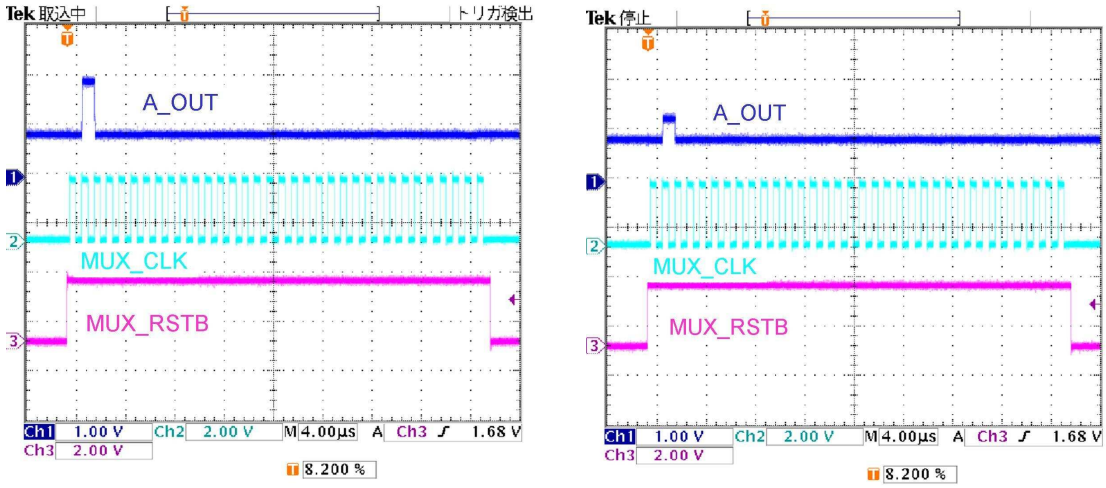

Figure 7.8: A_OUT taken by an oscilloscope. A blue line is A_OUT, a sky blue line is "MUX_CLK" and a pink line is "MUX_RSTB". The charge is injected to the channel 1, which is -1.4 pC in the left figure and -0.5 pC in the right one. The gain setting is ($\times 1$, $\times 4$).

- A_OUT saturates at the point where the ADC counts are about 3000 corresponding to about 1 V with the gain setting of ($\times 4$, $\times 2$) and ($\times 4$, $\times 1$). This is caused by the saturation of the opamp A shown in Fig. 7.4. With the gain setting of ($\times 1$, $\times 4$), we have not measured the linearity in the

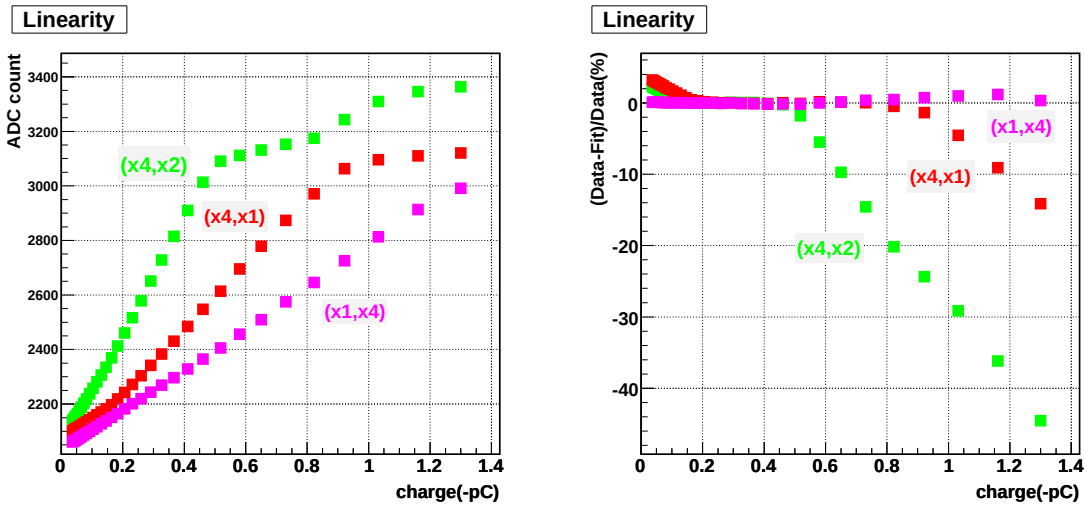

Figure 7.9: Amplitude (left) and the deviation from the linear extrapolation (right) of A_OUT as a function of the injected charge. Green points correspond to the gain setting of (×4, ×2), red points (×4, ×1) and pink points (×1, ×4).

region above the input charge of −1.3 pC because the input charge cannot be increased more with our setup.

- The gain with the setting of (×4, ×2) is twice larger than that with the setting of (×4, ×1), as expected. However the gain with the setting of (×4, ×1) is not the same as that with the setting of (×1, ×4). This is maybe because that the preamp gain of four is larger than the opamp gain of four.

- With the gain setting of (×4, ×2) and (×4, ×1) we see the nonlinearity in the low amplitude of A_OUT. This associates with this version of chip. Because of this problem, we use the gain setting of (×1, ×4) for the readout of MPPC.

The measured A_OUT gain of the channel 15, 16, 31 and 32 with the gain setting of (×1, ×4) is summarized in Table 7.2. The variation of gain is about 4% in these channels and this reflects the channel-by-channel gain variation of Trip-t.

Next we show the crosstalk of A_OUT between channels in Fig. 7.10. The gain setting is (×1, ×4), and the −1.4 pC charge is injected to the channel 15. The crosstalk in the channel i is defined as the following equation.

$$\text{crosstalk(i)} = \frac{ADC_{charge}(i) - ADC_{nocharge}(i)}{ADC_{charge}(15) - ADC_{nocharge}(15)}, \tag{7.1}$$

Channel	Gain (ADC counts/−pC)
15	730
16	710
31	735
32	732

Table 7.2: Measured A_OUT gain of each channel with the gain setting of (×1, ×4). The variation is found to be 4%.

where $ADC_{charge}(i)$ is the mean ADC counts for 1000 events in the channel i when the charge is injected and $ADC_{nocharge}(i)$ is one when the charge is not injected. The level of crosstalk is about 0.4% or less for all channels and we can neglect this level of crosstalk. We have also observed that the crosstalk decreases as the input charge to the channel 15 decreases.

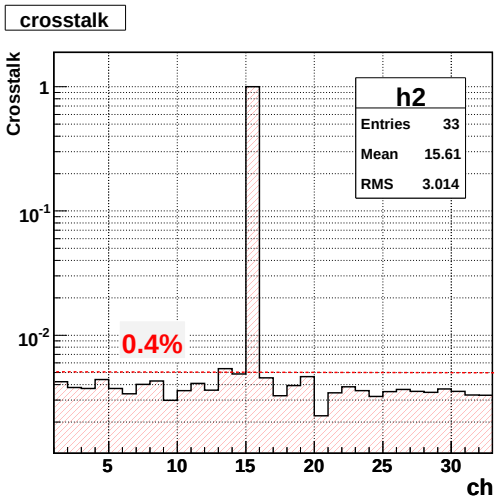

Figure 7.10: Crosstalk of A_OUT. The −1.4 pC charge is injected to the channel 15. The level of crosstalk is about 0.4%.

At last in this subsection we show in Fig. 7.11 the amplitude of A_OUT as a function of the time difference between the charge injection and the rising edge of "PIPE_CLK". Because the output from the preamp has a finite rise time, it is not properly sampled by "PIPE_CLK" if the time difference between the charge injection and the rising edge of "PIPE_CLK" is smaller than the rise time of the preamp output. In Fig. 7.11 we see the amplitude of A_OUT decreases by 4% from 200 ns to 100 ns of the time difference. However it falls quickly if the time difference becomes smaller than 100 ns. From this result we see the rising edge of "PIPE_CLK" must be more than 100 ns after the charge injection.

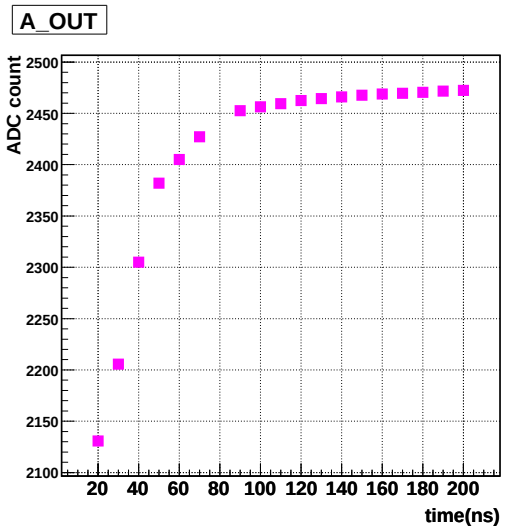

Figure 7.11: Amplitude of A_OUT as a function of the time difference between the charge injection and the rising edge of "PIPE_CLK". The injected charge is -0.6 pC and the gain setting of Trip-t is ($\times 1$, $\times 4$). We see the amplitude of A_OUT decreases by 4% from 200 ns to 100 ns of the time difference, but it falls quickly if the time difference becomes smaller than 100 ns.

7.3.2 T_OUT (Timing of the input charge)

Figure 7.12 shows the T_OUT taken by an oscilloscope. A blue line is T_OUT, a sky blue line is "MUX_CLK" and a pink line is "MUX_RSTB". The charge is injected to the channel 1 and the gain setting is ($\times 1$, $\times 4$). The time difference between the charge injection and the rising edge of "PIPE_CLK" is 200 ns in the left figure and 100 ns in the right one. We can see T_OUT at the second "MUX_CLK" which corresponds to the channel 1 and the amplitude of T_OUT in the left figure is larger. We also see the pedestal shift at the third "MUX_CLK". This is supposed to be due to the internal circuit of Trip-t, but the detail mechanism has not been understood yet.

Next, we show in Fig. 7.13 the amplitude of T_OUT (shown by ADC count) as a function of the time difference between the charge injection and the rising edge of "PIPE_CLK". We also show the deviation of T_OUT from the linear extrapolation in the same figure. The dynamic range of T_OUT is about 200 ns. Table 7.3 shows the measured T_OUT conversion factors for the channel 15, 16, 31 and 32. The unit of the T_OUT conversion factor is expressed as ADC counts/ns. The variation of the conversion factors for 4 channels is about 25% and larger than the variation of A_OUT gain.

Finally, we show in Figure 7.14 the amplitude of T_OUT as a function of the injected charge. The register V_TH is set to be 255, which is the minimum value. We can see from Fig. 7.14 the amplitude of T_OUT decreases when the

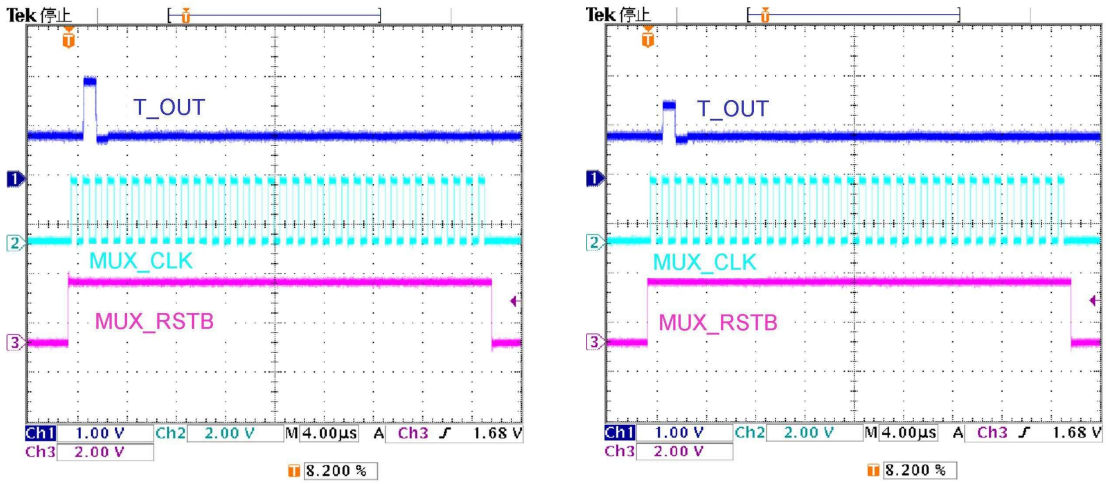

Figure 7.12: T_OUT taken by an oscilloscope. A blue line is T_OUT, a sky blue line is "MUX_CLK" and a pink line is "MUX_RSTB". The charge is injected to the channel 1 and the gain setting is (×1, ×4). The time difference between the charge injection and the rising edge of "PIPE_CLK" is 200 ns in the left figure and 100 ns in the right one.

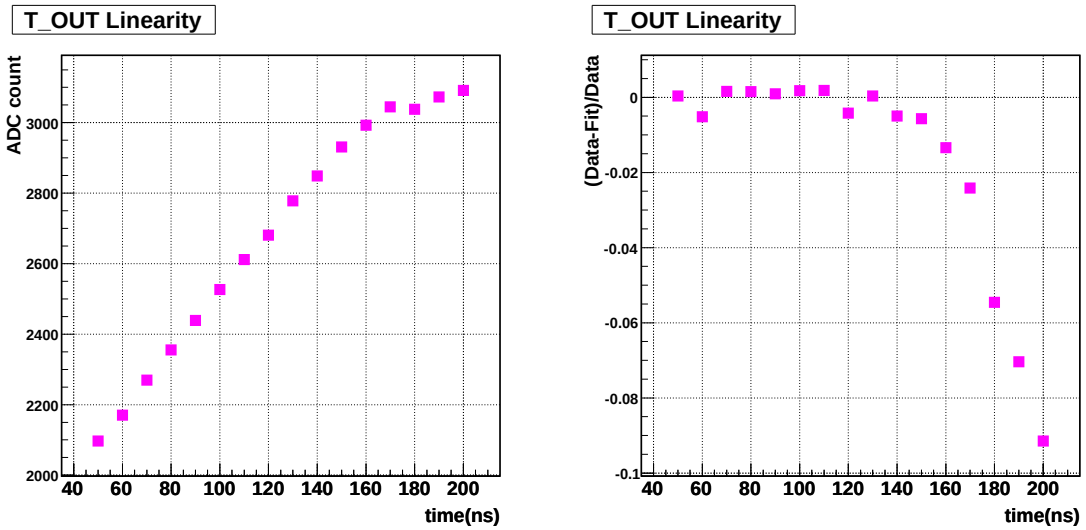

Figure 7.13: Amplitude (left) and the deviation from the linear extrapolation (right) of T_OUT as a function of the time difference between the charge injection and the rising edge of "PIPE_CLK". The dynamic range of T_OUT is found to be about 200 ns.

Channel	Conversion factor (ADC counts/ns)
15	8.52
16	8.60
31	8.00
32	9.97

Table 7.3: Measured T_OUT conversion factors for each channel. The variation is about 25%.

injected charge gets small. This is explained as follows. As the injected charge gets smaller, the time that the injected charge takes to fire the discriminator becomes longer and the time difference between the discriminator firing and the rising edge of "PIPE_CLK" becomes smaller. Hence Fig. 7.14 shows the timewalk dependence on the signal size.

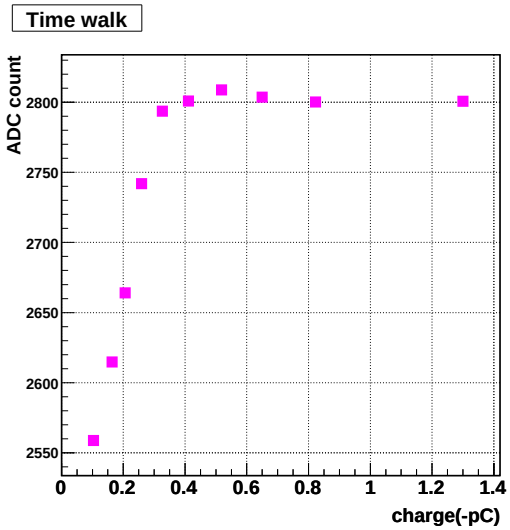

Figure 7.14: Amplitude of T_OUT as a function of injected charge. The register V_TH is set to be 255. This shows the timewalk dependence on the signal size.

7.3.3 D_OUT (Discriminated output for each channel)

Figure 7.15 shows D_OUT taken by an oscilloscope. A blue line is the charge injection signal after the attenuator shown in Fig. 7.7 and a sky blue line is D_OUT. The input charge is -0.5 pC. We see D_OUT about 10ns after the charge is injected. This is supposed to be the delay inside Trip-t because the time that the charge takes to come into Trip-t is smaller enough than 10 ns.

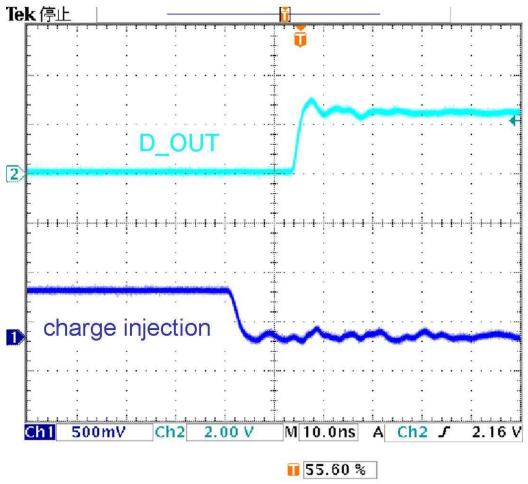

Figure 7.15: D_OUT taken by an oscilloscope. A blue line is the charge injection signal before the 1 pF capacitor shown in Fig. 7.7 and a sky blue line is D_OUT. The injected charge is -0.5 pC. We see D_OUT about 10 ns after the charge injection.

Next we show in Fig. 7.16 discriminator turn-on curves for 4 channels. We inject the -0.14 pC charge which corresponds to 1.5 p.e. of the MPPC signal with the gain of 6×10^5 to each input and count the number of times the discriminator fires for the 100 preamp integration periods with changing the threshold value (V_TH). The preamp gain of Trip-t is four. From Fig. 7.16 we see that the spread of V_TH is 3, which corresponds to 0.02 p.e. with the MPPC gain of 6×10^5. Because we cannot set the different threshold value to each input of Trip-t, this result means the threshold uncertainty is 0.02 p.e. when we set the 1.5 p.e. threshold to the inputs of Trip-t. This level of the uncertainty is not a problem for our use because the MPPC signal is quantized to multiples of 1 p.e. charge.

At last in this subsection we show in Fig 7.17 the threshold value (V_TH) where the discriminator just fires as a function of injected charge. We measure the discriminator turn-on curve for each injected charge as shown in Fig. 7.16 and find the threshold value where the probability of firing the discriminator becomes 50%. In Fig. 7.17 red points correspond to the $\times 1$ preamp gain and green ones to the $\times 4$ preamp gain. We see from this figure that V_TH where the discriminator fires depends linearly on the injected charge with both gain settings. With the high (low) gain setting, one V_TH unit corresponds to 0.65 (2.5) fC, respectively.

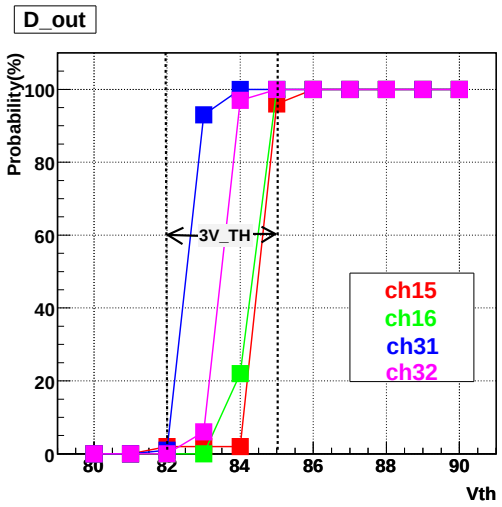

Figure 7.16: Probability of the discriminator firing as a function of V_TH for 4 channels. Different colors corresponds to the different channels. The injected charge to each channel is -0.14 pC. The spread of V_TH is found to be about 3.

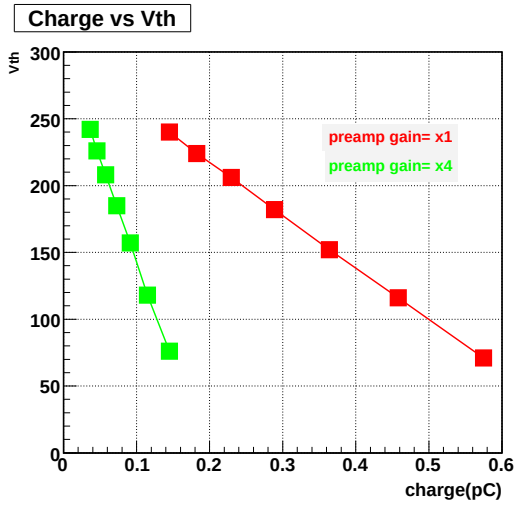

Figure 7.17: Threshold value (V_TH) where the discriminator just fires as a function of the injected charge. Red (Green) points correspond to the $\times 1$ (4) preamp gain. V_TH where the discriminator just fires depends linearly on the injected charge.

7.4 Summary

In this chapter we have shown the study of the basic performance of Trip-t. Trip-t chip is produced at Fermilab and is going to be used in T2K. We can operate Trip-t correctly and observe A_OUT, T_OUT and D_OUT with our test board. The following is the summary of basic performance of Trip-t.

- A_OUT
  - Gain variation for four channels is 4%.
  - We see the nonlinearity at the low pulse amplitude, but this will be fixed for the new venison chip.
  - Crosstalk level of A_OUT is 0.4% or less for all channels.
  - Rising edge of "PIPE_CLK" must be more than 100 ns after the charge injection.
- T_OUT
  - Dynamic range of T_OUT is $\sim$ 200 ns.
  - Variation of the conversion factors for four channels is 25%.
- D_OUT
  - We see D_OUT $\sim$ 10 ns after the charge injection.
  - Threshold uncertainty is 0.02 p.e. at the 1.5 p.e. threshold, assuming the MPPC gain of 6×10^5.
  - With the $\times 1$ (4) preamp gain setting, one V_TH unit corresponds to 0.65 (2.5) fC.

In the next chapter we show the readout of MPPC with Trip-t.

Chapter 8

READOUT OF MPPC WITH TRIP-T

In this chapter we report the readout of MPPC with Trip-t. We use the latest 100 and 400 pixel devices delivered in Oct. 2006 in this chapter. The gain setting of Trip-t is ($\times$1, $\times$4) unless we note.

8.1 SciBar DAQ board

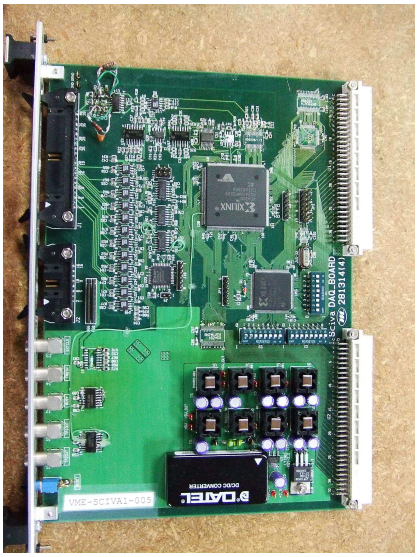

Figure 8.1: Photograph of SciBar DAQ board.

SciBar DAQ board (Fig. 8.1) is a VME standard module and was originally developed for the SciBar detector in the K2K experiment [23]. In SciBar it was used to digitize the analog signal from the VA chip [24] which serialized the

64 channel analog signals from a Multi-Anode PMT (MAPMT) and controlled the readout sequence of VA. We use the DAQ board for an analog-to-digital conversion of A_OUT from Trip-t. The receiver circuit on the DAQ board is shown in Fig. 8.2. The differential inputs, outm and outp, are amplified at the first opamp and become a single end signal by subtracting outp from outm through the second opamp. The analog output from the receiver circuit is digitized by a 12 bits flash ADC. The input range of the flash ADC is 0 $\sim$ +5 V and the maximum conversion frequency is 10 MHz. We set 2.5 V offset to the input of the flash ADC, supposing the variation of the pedestal level. Therefore the effective dynamic range of the flash ADC is 11 bits.

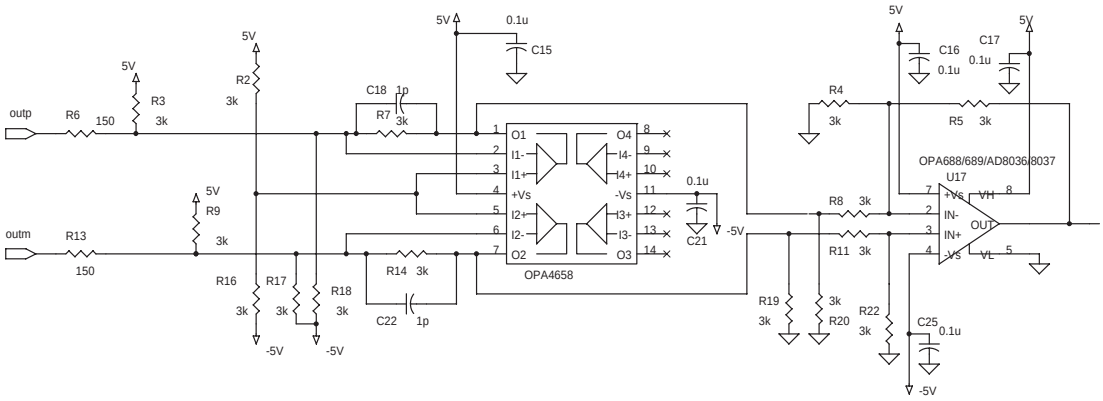

Figure 8.2: Schematic of the receiver circuit on the DAQ board.

8.2 Transmission of the Trip-t output

We planed to connect Trip-t and DAQ board with a 4 m flat cable. We put an opamp (ANALOG DEVICES AD827) just after Trip-t because the output impedance of Trip-t is $\sim$ MΩ. The opamp needs DC$\pm$5V and the gain of the opamp is 1.

8.3 Readout of MPPC with DAQ board and Trip-t

We read out MPPC with DAQ board and Trip-t, illuminating MPPC by LED. The setup is shown in Fig. 8.3 and 8.4. Several modifications are made to the DAQ board in order to adjust the readout of MPPC.

1. Since A_OUT of Trip-t has 1.0 V DC offset, we put A_OUT to outm of the DAQ board and DC+1 V to outp. By subtracting outp from outm, A_OUT has no DC offset.

2. We change the gain of the DAQ board from 20 to 1 because the gain of Trip-t is enough high.

Generally the coupling of a detector to the electronics can be performed either directly (DC coupling) or through an additional capacitor (AC coupling). For the AC coupling, the additional capacitor will contribute to the noise. On the other hand, for the DC coupling, the applied bias voltage to the detector may damage the electronics. In order to keep the electronics safe, we have chosen the AC coupling for the coupling of MPPC to Trip-t. The capacitance and the resistance for the AC coupling are 100 nF and 100 kΩ, respectively. The trigger rate is about 1 kHz, which is limited by the data acquisition rate of the DAQ board.

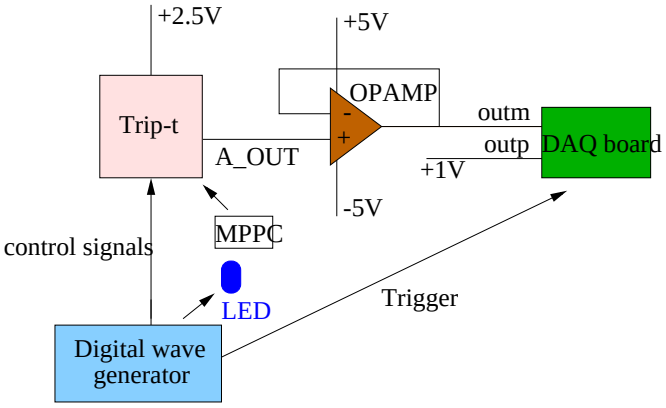

Figure 8.3: Schematic of the setup for the readout of MPPC with DAQ board and Trip-t. MPPC is illuminated by a blue LED. The output from Trip-t (A_OUT) is sent to the DAQ board through the opamp and digitized by the flash ADC on the DAQ board.

The left figure of Fig. 8.5 shows A_OUT of a 400 pixel device taken by an oscilloscope and the right figure of Fig. 8.5 shows the ADC distribution. The temperature is 20 °C and the gain of MPPC is 7.5×10^5. We can see clearly separated photopeaks in both figures. Thus we successfully read out MPPC with Trip-t and DAQ board.

Next, Figure 8.6 shows the gain of MPPC measured at 20°C with two systems. One is by the Trip-t&DAQ board and the other by the CAMAC charge sensitive ADC. Red points correspond to the Trip-t&DAQ board and green ones the CAMAC charge sensitive ADC. The left (right) figure is for a 100 (400) pixel device, respectively. The gain of MPPC measured by each system agrees well each other within a few % level for both 100 and 400 pixel devices and the gain of Trip-t can be well calibrated.

Finally we read out four MPPCs (one is a 100 pixel device and the other three are 400 pixel devices) simultaneously with Trip-t by injecting the uniform light to

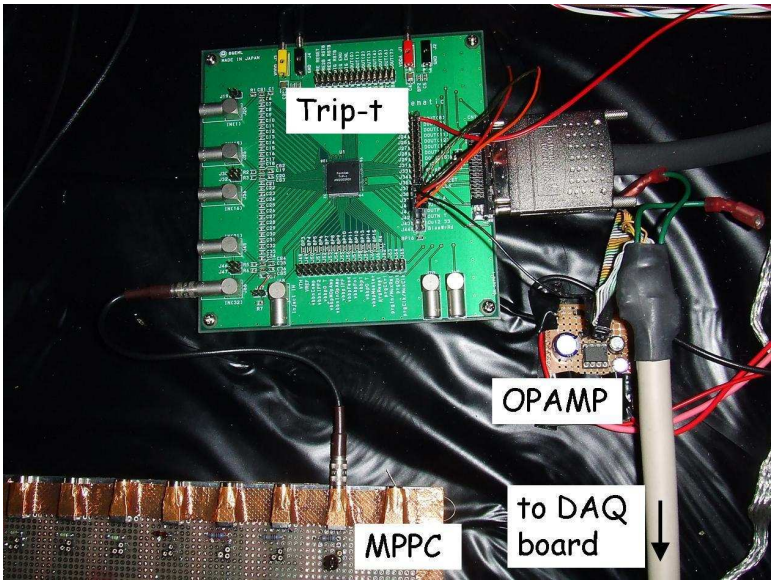

Figure 8.4: Photograph of the setup for the readout of MPPC with DAQ board and Trip-t.

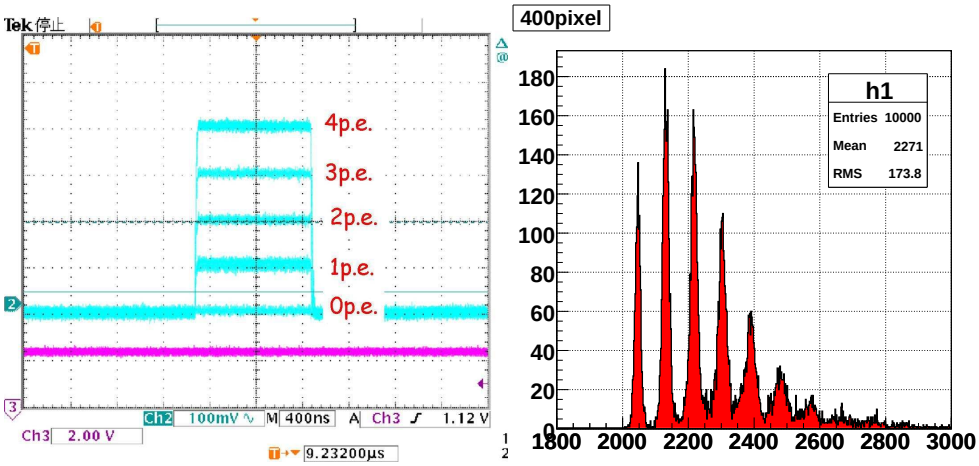

Figure 8.5: A_OUT of a 400 pixel device taken by an oscilloscope (left) and the ADC distribution (right). The temperature is 20°C and the gain of MPPC is 7.5 $\times$ 10^5. We see clearly separated photo peaks in both figures.

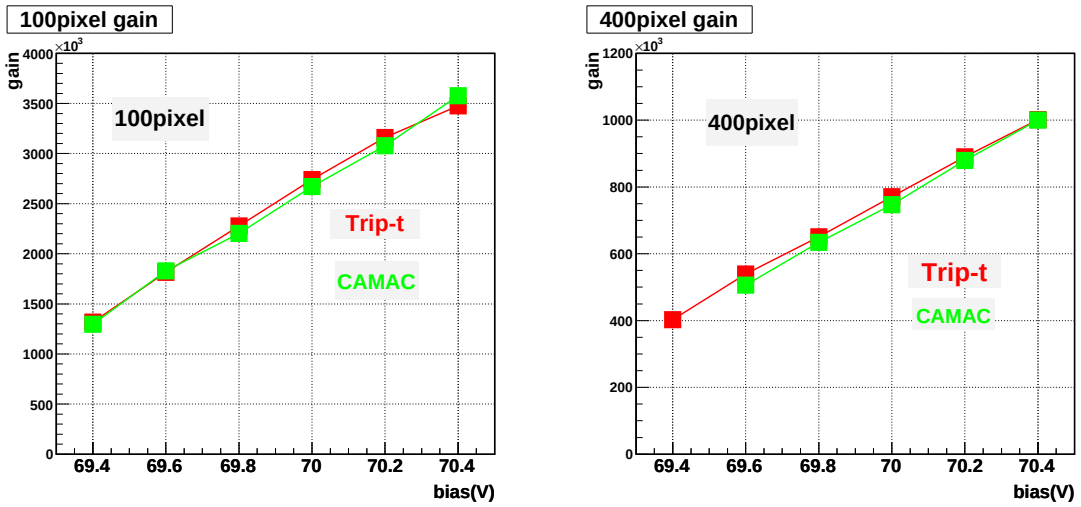

Figure 8.6: Gain of MPPC measured at 20°C with the Trip-t&DAQ board (red points) and the CAMAC charge sensitive ADC (green points). The left (right) figure is for a 100 (400) pixel device. The gain measured by each system agrees well each other for both 100 and 400 devices.

them with low intensity. Figure 8.7 shows the ADC distributions of four MPPCs. The same bias voltage, 70.0 V, is applied to all MPPCs and the temperature is 20°C. The measured gain of MPPC is summarized as follows;

- 100 pixel : 1.8 $\times 10^6$
- 400 pixel-1 : 7.4 $\times 10^5$
- 400 pixel-2 : 6.4 $\times 10^5$
- 400 pixel-3 : 1.0 $\times 10^6$,

where 400 pixel-1 corresponds to the right upper figure of Fig. 8.7, 400 pixel-2 to the left lower one and 400 pixel-3 to the right lower one.

We succeed in observing clearly separated photo peaks for all MPPCs using Trip-t. Thus we have shown that Trip-t can be used for the readout of MPPC in T2K. In the lower right figure of Fig. 8.7 we see tails of photopeaks to the direction of lower ADC counts. This also can be seen in other channels, as shown in Fig. 8.8 which is the log-scale figure of Fig. 8.7. The cause of the tails of photopeaks is supposed to be the charge up of an AC coupling capacitor. Figure 8.9 shows a schematic of the coupling part of MPPC and Trip-t. If the capacitor is charged up by the MPPC noise during the preamp reset period of Trip-t, the current that is flowing out of the capacitor through a 100 kΩ resistor will cause positive charge to be integrated by Trip-t when the preamp becomes active. This positive charge will cause the tails of photopeaks to the lower ADC counts.

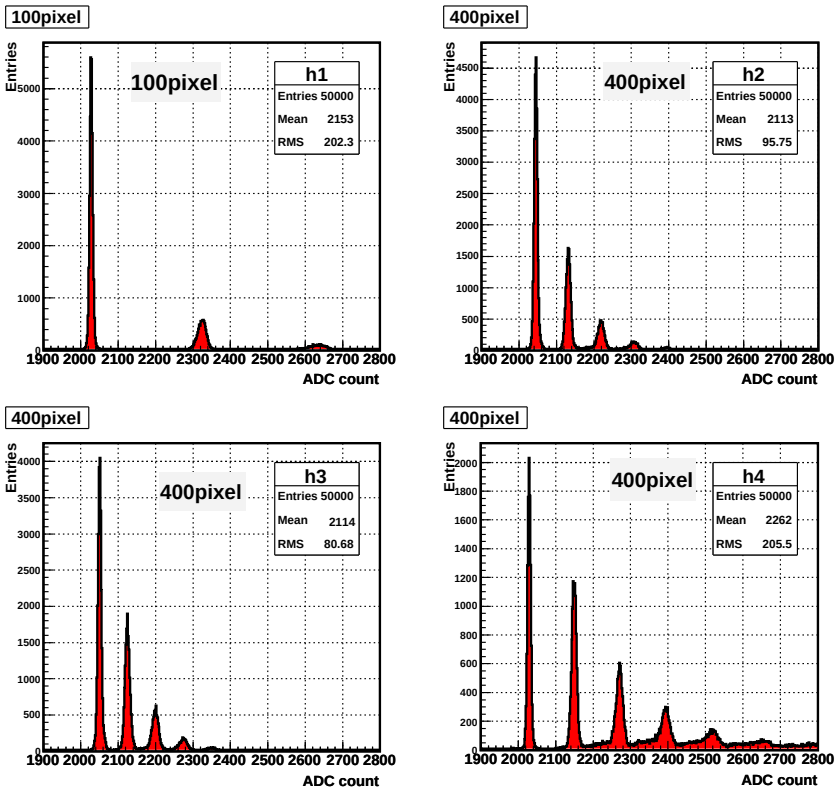

Figure 8.7: ADC distribution of four MPPCs. The left upper figure is for a 100 pixel device and the others are for 400 pixel devices. The same bias voltage, 70.0 V, is applied to all MPPCs and the temperature is 20°C.

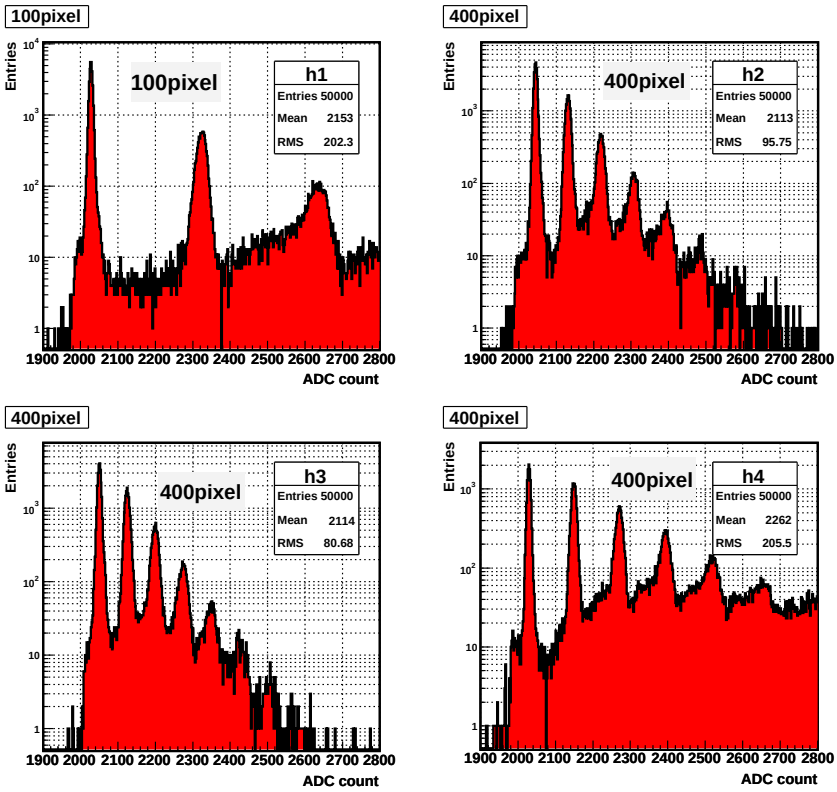

Figure 8.8: ADC distribution of four MPPCs. The vertical axis is scaled with logarithm. The left upper figure is for a 100 pixel device and the others are for 400 pixel devices. The same bias voltage, 70.0 V, is applied to all MPPCs and the temperature is 20°C.

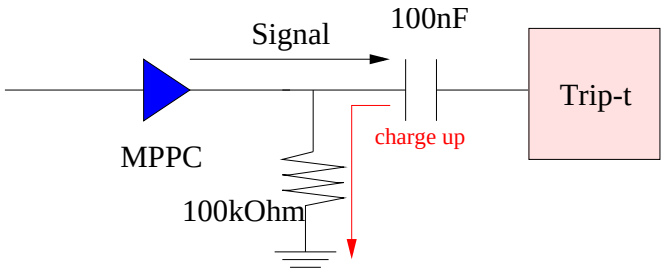

Figure 8.9: Schematic of the coupling part of MPPC and Trip-t. The MPPC is AC coupled to Trip-t with a 100 nF capacitor and a 100 kΩ resistor.

Even if we see the tail of photopeaks, the measured gain with Trip-t is found to be same as that measured with a CAMAC charge sensitive ADC. Because the gain of MPPC is measured correctly with Trip-t, this is not a problem not only for the test of the large number of MPPC samples but also the real experiment.

8.4 Evaluation of the noise level

In this section, we evaluate the noise level of our setup shown in Fig. 8.3. Generally, electric noise is divided into two kinds, normal-mode noise and common-mode noise.

- Normal-mode noise : Noise that goes to an electric circuit through a signal line and returns to a signal source through a signal ground. It is impossible to remove in offline because the direction of going noise current is opposite to that of returning noise current.
- Common-mode noise : Noise that flows in a signal line and a signal ground line with the same direction. This noise penetrates into an electric circuit through the flow capacitor between the signal line and an external ground and is observed in common to all the channels of the electric circuit. It is possible to remove in offline.

The schematic of the normal-mode noise and common-mode noise is shown in Fig. 8.10.

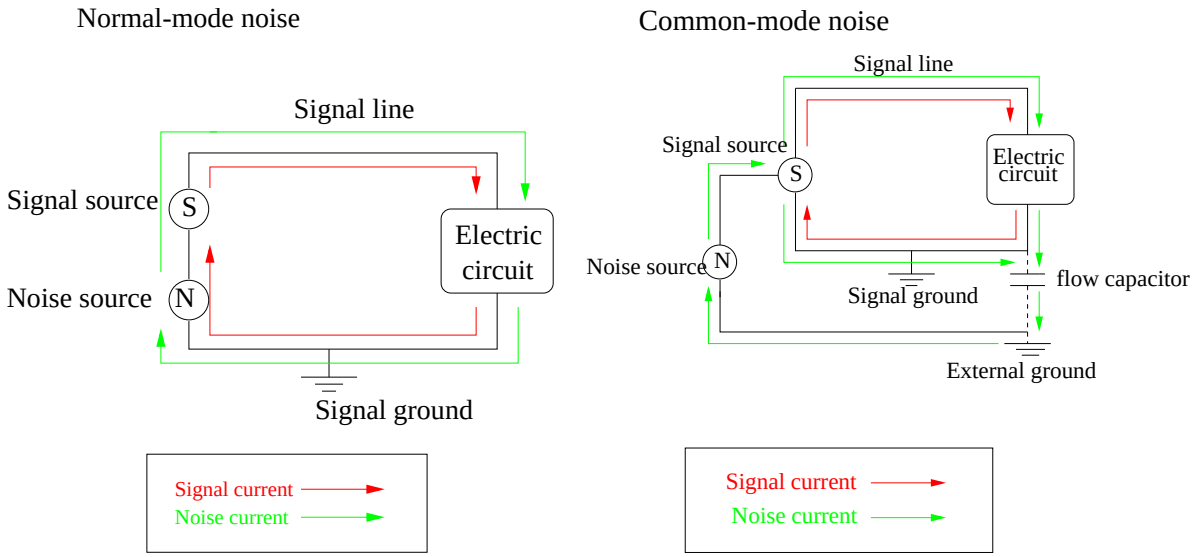

Figure 8.10: Schematic of the normal-mode noise (left) and common-mode noise (right). A red (green) line shows the signal (noise) current, respectively.

Because the readout time of Trip-t is small enough compared to the period of the common-mode, the common-mode of Trip-t at the event number of i is written as the following;

$$c(i) = \frac{1}{N_{ch}} \sum_{j=1}^{N_{ch}} a_j(i), \tag{8.1}$$

where

- c(i) : Common-mode at the event number of i
- N_{ch} : Number of input channels of Trip-t , which is 5
- a_j(i) : Pedestal ADC counts in the channel j at the event number of i.

Figure 8.11 shows the time variation of the common-mode for 1000 events. The trigger rate is about 1 kHz and the total readout time is about 1 second. One can see there are two components in the common-mode; one is the component with high frequency and large amplitude and the other is the component with low frequency. Figure 8.12 also shows a scatter plot of the pedestal ADC counts in the channel connected to MPPC and the common-mode for 1000 events. The bias voltage less than the breakdown voltage is applied to MPPC. We observe a positive correlation between these two values.

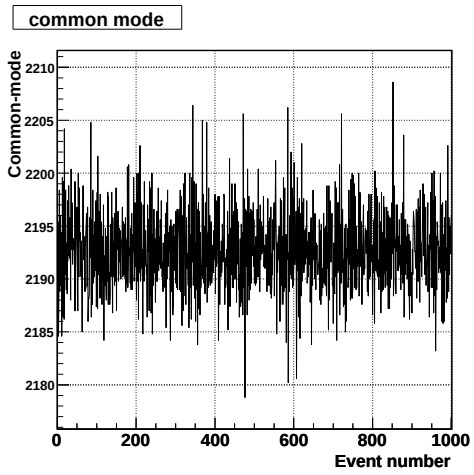

Figure 8.11: Time variation of the common-mode for the period of 1 second. One can see two components in the common-mode.

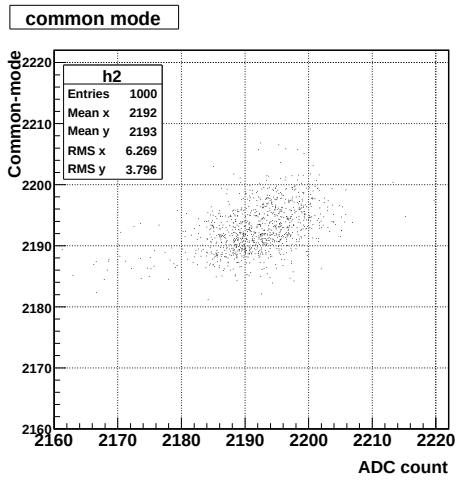

Figure 8.12: Scatter plot of the pedestal ADC count in the channel connected to MPPC and the common-mode. There is a positive correlation between two values.

Figure 8.13 shows the ADC distributions of the pedestal for 1000 events in the channel connected to MPPC before (black) and after (red) subtracting the

common-mode. The center value of each histogram is set to be zero. The RMS of the ADC distribution is 7.6 (6.6) before (after) subtracting the common mode. From this figure we conclude that there is common-mode noise in this channel.

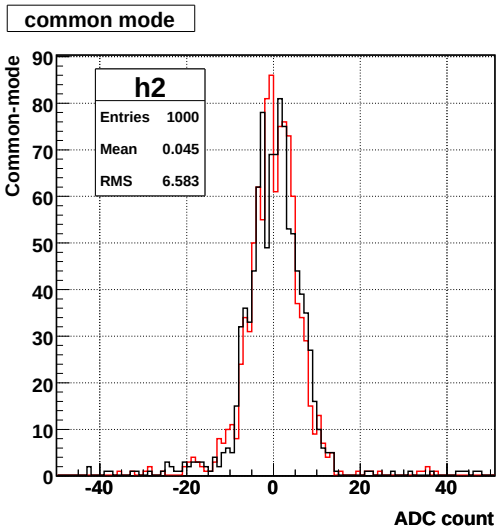

Figure 8.13: ADC distributions of the pedestal in the channel connected to MPPC before (black) and after (red) subtracting the common mode for 1000 events. The RMS of the ADC distribution is 7.6 (6.6) before (after) subtracting the common mode.

Next we show in Table 8.1 the RMS of the pedestal in the channel connected to MPPC after subtracting the common mode with each gain setting of Trip-t. We set the preamp gain to be one and only change the opamp gain. The RMS of the pedestal does not almost change even if the opamp gain increases. This result means that the noise level of our setup is determined by the electronics after Trip-t. This noise level corresponds to about 0.1 p.e. with the MPPC gain of 7.5 $\times$ 10^5 and is suppressed to be small enough for the test of basic performance of MPPC. This noise level is also satisfactory for T2K because the light yield for MIP is $\sim$ 20 p.e.

Opamp gain	RMS
$\times$1	6.0
$\times$2	5.9
$\times$4	6.6
$\times$8	6.6

Table 8.1: RMS of the pedestal in the channel connected to MPPC after subtracting the common mode with each gain setting.

8.5 Discussion

In this section we discuss the dynamic range of Trip-t and mention the real type electronics in T2K. In Fig. 7.9 we observe the saturation of Trip-t for the the amount of charge ($Q_{saturation}$) with each gain setting. The dynamic range of Trip-t with each gain setting is defined as;

$$\text{dynamic range} = \frac{Q_{saturation}}{(\text{MPPC gain}) \times \text{e}}, \tag{8.2}$$

where MPPC gain is set to be 7.5×10^5 and e is the elementary charge. We set the preamp gain to be one and only change the opamp gain. Table 8.2 shows the dynamic ranges of Trip-t and the signal-to-noise ratio (S/N) with the opamp gain of $\times 1$, $\times 2$, and $\times 4$. The S/N is defined as the following equation.

$$\text{S/N} = \frac{M_{1p.e.} - M_{ped}}{\sigma_{ped}}, \tag{8.3}$$

where $M_{1p.e.}$ is the mean ADC counts for the 1 p.e. peak, M_{ped} is the mean ADC counts for the pedestal peak and σ_{ped} is the ADC counts for the sigma of the pedestal peak.

Opamp gain	Dynamic range (p.e.)	S/N
$\times 1$	~ 40	3
$\times 2$	~ 20	10
$\times 4$	~ 10	20

Table 8.2: Dynamic range and signal-to-noise ratio (S/N) of Trip-t with the opamp gain of $\times 1$, $\times 2$ and $\times 4$. We assume the gain of MPPC is 7.5×10^5.

Even with the $\times 1$ opamp gain (the least gain) the dynamic range of Trip-t is ~ 40 p.e. For the view of the test of large number of samples, this small dynamic range is OK because we only need to see several photopeaks. However in T2K we need the dynamic range up to ~ 400 p.e. In order to obtain this dynamic range, there is a plan to divide the signal of MPPC to the high-gain channel and the low-gain channel with two capacitors for the real type electronics in T2K, as shown in Fig. 8.15. The high gain channel is used to set a discriminator with sufficient resolution and determine the gain of MPPC with photopeaks. The low-gain channel is used to accommodate the large signal up to ~ 400 p.e. Assuming the ratio of the capacitance in the high gain channel to that in the low gain channel is 10, the gain setting of Trip-t must be the lowest in order to obtain the dynamic range up to ~ 400 p.e. Figure 8.14 shows the ADC distribution of 400 pixel MPPC with the lowest gain setting of Trip-t. The MPPC gain is 7.7×10^5. We can see photopeaks even with this gain setting. Hence it will be possible to

obtain the large dynamic range with Trip-t with the high gain/low gain method, but more detailed study is also necessary.

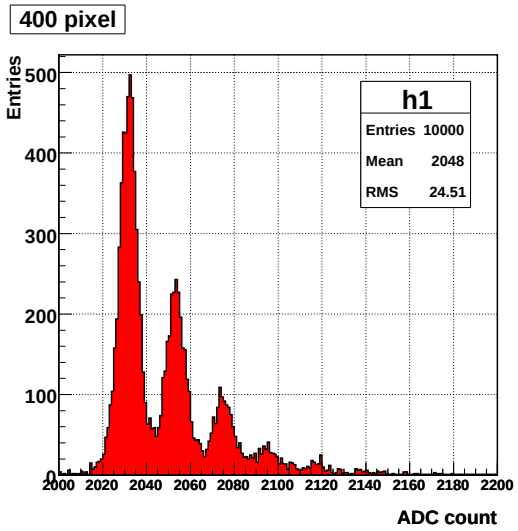

Figure 8.14: ADC distribution of 400 pixel MPPC with the lowest gain setting of Trip-t. The MPPC gain is 7.7×10^5. We can see photopeaks with this gain setting.

Moreover, for the real type electronics, the following improvements are considered;

- Four Trip-t chips and two ADCs are mounted on the same board. The total number of the readout channels per board is 64 with 16 high/16 low gain channels per chip.
- Control of Trip-t chips and ADCs are performed by one FPGA (Field Programmable Gate Arrays)[1] on the board.
- Bias voltage applied to each MPPC can be trimmed by variable resistors, supposing the device-by-device variation of the breakdown voltage.
- Gain calibration of each Trip-t channel is possible by injecting a programmable calibration voltage through a capacitor.
- Temperature monitoring around MPPC can be done.

The current design of the real type front-end electronics is shown in Fig. 8.16. Such a real type electronics is now mainly developed by the English group in T2K.

[1] FPGA is one of the programmable logic ICs. It realizes the logic by loading the configuration data into the interior memory cells.

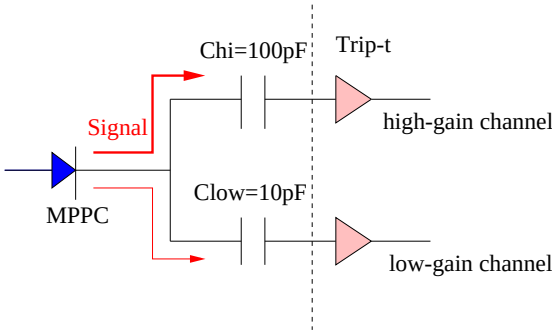

Figure 8.15: Diagram of the MPPC and Trip-t connection. The MPPC signal is divided to the high-gain channel and the low-gain channel with two different capacitors.

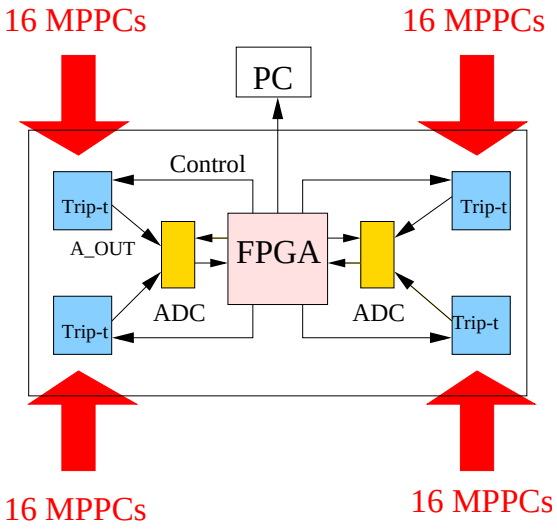

Figure 8.16: Current design of the real type front-end electronics for T2K. Four Trip-t chips and two ADCs are mounted on the board. The control of the Trip-t chips and ADCs are performed by one FPGA.

8.6 Summary and future plans

In this chapter we have shown the readout of MPPC with Trip-t and DAQ board used in the K2K SciBar detector. We have observed clearly separated photopeaks of four MPPCs with the prototype board that has four inputs. The measured gain of MPPC with Trip-t agrees well that with the CAMAC charge sensitive ADC and the gain of Trip-t is well calibrated. The noise level of our setup is 0.1 p.e. with the MPPC gain of 7.5×10^5 and small enough compared to the MPPC signal. The dynamic range of Trip-t is ~ 40 p.e. even with the lowest gain setting, but in T2K there is a plan to divide the MPPC signal to the high-gain channel and the low gain channel with two capacitors in order to accommodate the large signal up to ~ 400 p.e. Thus we could show that Trip-t can be used for the readout of MPPC in T2K. This is also an important milestone in the development of MPPC itself. Our future development of the readout electronics includes;

- Trip-t board with the 32 channels
- control of Trip-t chip with Field Programmable Gate Array (FPGA)

The test of the large number of MPPCs which will be delivered in Feb. 2007 will be performed with the next 32 channels Trip-t board.

Chapter 9

CONCLUSION

In this thesis we study Multi-Pixel Photon Counter (MPPC) and the readout electronics. MPPC is a new photodetector manufactured by Hamamatsu Photonics. It consists of many small avalanche photodiodes typically in an area of 1 mm $\times$ 1 mm. Each pixel works in the Geiger mode and the output from MPPC is total summation of the output from all APD pixels. Because of the compact size, tolerance to magnetic field and high photon detection efficiency, it is going to be used for the T2K experiment starting in April 2009.

At first we tested various features of the latest MPPC samples. At the room temperature the gain of $\sim 10^6$ is achieved with the noise rate less than 500 kHz at the 0.5 p.e. threshold. The photon detection efficiency for green light is two to three times larger than that of a photomultiplier tube. The cross-talk rate is typically 20% and less than 40%. The nonlinearity is about 20% at the 40 (120) injected photoelectrons for a 100 (400) pixel device. The recovery time is less than 100 ns. The basic performance of MPPC is satisfactory for the T2K experiment. The cross-talk rate has been increased from the previous samples, but Hamamatsu Photonics is now working to reduce the cross-talk rate for the next samples. It is also shown that the the uniformity within one pixel and pixel-to-pixel uniformity are both about 3%, using the laser injection system of KEK Detector Technology Project. This is useful information for the product development. The response of MPPC has a temperature dependence, but we have demonstrated it can be corrected within about 3% level by two independent correction methods even if the temperature changes by 5 °C.

In T2K we need the compact and multi-channel readout electronics of MPPC in order to handle the large number of readout channels. Moreover the establishment of the test system for mass production of MPPC is also necessary. For these purposes we have developed the readout electronics of MPPC with the Trip-t chip which was produced at Fermilab. We have observed clearly separated photopeaks of MPPC with the Trip-t test board that has four input channels. The measured gain of MPPC with Trip-t agrees well the gain measured with a CAMAC charge sensitive ADC and the gain of Trip-t is well calibrated. The noise level of our

system is about 0.1 p.e. with the MPPC gain of 7.5×10^5 and small enough compared to the MPPC signal. The dynamic range of Trip-t is about 40 p.e. even with the lowest gain setting, but in T2K there is a plan to divide the MPPC signal to the high-gain and low-gain channels with two different capacitors in order to accommodate the large signal up to 400 p.e. Thus we have shown that Trip-t can be used for the readout of MPPC in T2K and succeeded in establishing the multi-channel readout system of MPPC. We are now developing the Trip-t board with 32 channel inputs and the test of the large number of MPPCs which will be delivered in Feb. 2007 will be performed by using this new board. Our study is an important step not only for the T2K experiment but also the wide use of MPPC.

ACKNOWLEDGEMENT

This thesis would not have been realized without many supports from everyone around me.

First of all, I would like to express my best thanks to my supervisor Prof. Tsuyoshi Nakaya, for giving me the opportunity to work for the T2K experiment and for guiding me to the right way when I was in trouble throughout this two years. His attitude to physics always stimulated me. I also express my gratitude to Dr. Masashi Yokoyama, who is a leader of the photosensor group for T2K. Discussions with him always brought me up to the next step. It was a great experience for me to take part in such an excellent photodetector, MPPC. He also works for the leader of Karaoke club in High Energy Group. I also would like to send my appreciation to Prof. Koichiro Nishikawa, who is the spokesperson of T2K and the supervisor during my first year of graduate school.

I express my thanks to Prof. M. Tanaka, for supporting the development of electronics. When I was not familiar with electronics, he taught me many things kindly though he was very busy. Without his help, I could not have finished my research. I also thanks to Mr. T. Murakami for supporting the development of electronics, especially the production of the prototype board. I also send my thanks to Mr. P. Rubinov for teaching me about Trip-t kindly when I visited Fermilab.

I spent almost one year in KEK. I want to express my warm gratitude to Dr. Ken Sakashita, for taking care of me kindly. Without him (his car), I could not have "survived" in KEK. I also thanks to Dr. M. Hasegawa and Ms. N. Taniguchi. The talk with them was always very enjoyable for me.

I also thanks to Prof. K. Yoshimura and Dr. T. Nakadaira, who are the leaders of the photonsensor group of KEK Detector Technology Project. They always helped me when I was performing a laser test in KEK.

I also express my thanks to the members of High Energy Group of Kyoto University. I was very happy to work for T2K with Mr. K. Matsuoka, who is the same grade as me. Please achieve T2K with your MUMON.

Dr. H. Tanaka, Mr. K. Hiraide, Mr. Y. Kurimoto and Mr. Y. Nakajima

helped me as the seniors of neutrino group especially when I was the first year of graduate school. I wish the SciBooNE experiment will be successful. I also express my thanks to Mr. H. Kawamuko, Mr. H. Kubo and Mr. S. Gomi.

Kawamuko-kun, your sleeping face always makes me relaxed.

Kubo-kun, leave your passport in your hotel when you go to sea in abroad.

Gomi-kun, sorry for interrupting your work by removing a CAMAC device driver from your PC by my mistake.

I would like to express my thanks to all the other members of High Energy Group of Kyoto University equally.

Finally, I would like to send my best thanks to my family and friends.

Appendix A

COMPARISON OF LATEST AND OLD MPPC SAMPLES

In this chapter we show the comparison of latest MPPC samples to old ones. The latest samples were delivered in Oct. 2006 and the old ones were delivered in Jan. 2006. The method of each measurement is the same as that described in Chapter 3.

A.1 Gain

Figure A.1 shows the measured gain of 100 (left) and 400 (right) pixel devices as a function of ΔV. Green points correspond to the latest sample and red points the old one. The capacitance of the latest (old) 100 pixel sample is found to be 356 fF (223 fF) by fitting the gain-voltage relation with Eq. 3.1. The new 100 pixel sample has the larger capacitance than that of the old 100 pixel one and results in larger gain at the same ΔV. The capacitance of the new (old) 400 pixel sample is also found to be 92 fF (86 fF), respectively. The new 400 pixel sample has the same capacitance as that of the old 400 pixel one.

A.2 Noise rate

Figure A.2 shows the 0.5 p.e. threshold noise rate of 100 (left) and 400 (right) pixel devices as a function of ΔV. Green points correspond to the latest sample and red points the old one. The measured noise rate of the latest sample is much smaller than that of the old one especially for the 400 pixel device.

A.3 PDE

Figure A.3 shows the measured PDE of 100 (left) and 400 (right) pixel devices as a function of ΔV. The PDE is for green light and expressed as the relative value

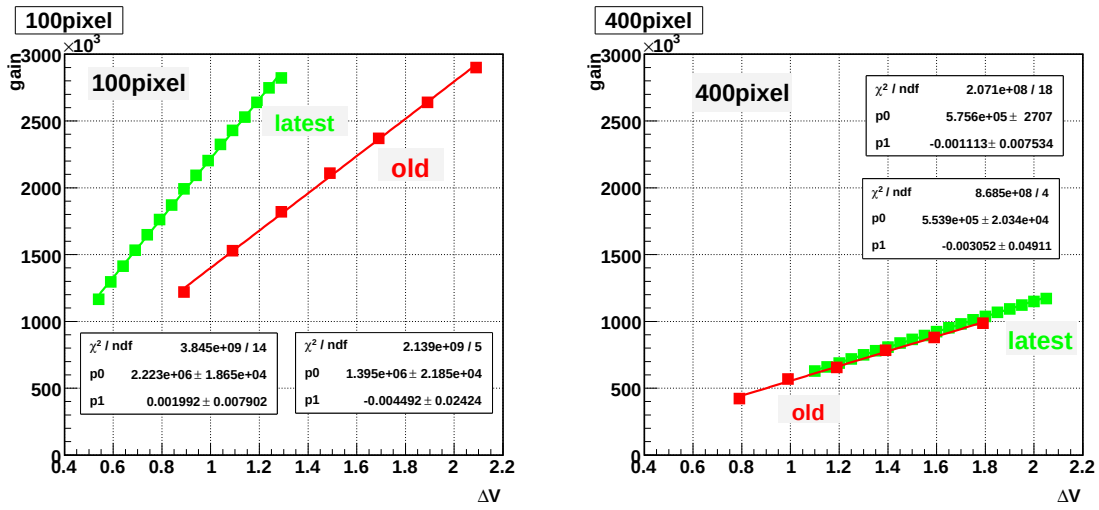

Figure A.1: Measured gain of 100 (left) and 400 (right) pixel devices as a function of ΔV. Green points correspond to the latest sample and red points the old one. The measurement was done at 20°C.

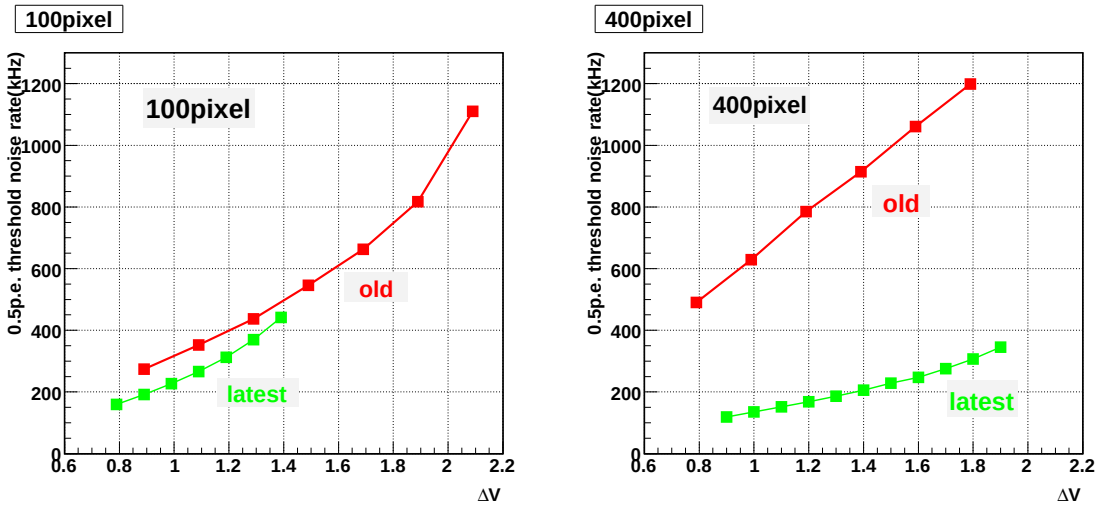

Figure A.2: Measured 0.5 p.e. threshold noise rate of 100 pixel (left) and 400 pixel (right) devices as a function of ΔV. Green points correspond to the latest sample and red points the old one. The measurement was done at 20°C.

to QE of a PMT. Green points correspond to the latest sample and red points the old one. The measured PDE of the latest sample is much higher than that of the old sample especially for the 100 pixel one. The PDE for the 100 pixel sample has been increased by a factor of about 1.6. The geometrical efficiency for the 100 pixel sample is found to be also increased by a factor of 1.6, as described in Subsection 5.3. Therefore the improvement of PDE for the latest sample is due to the increase of the geometrical efficiency, as shown in Fig. A.4.

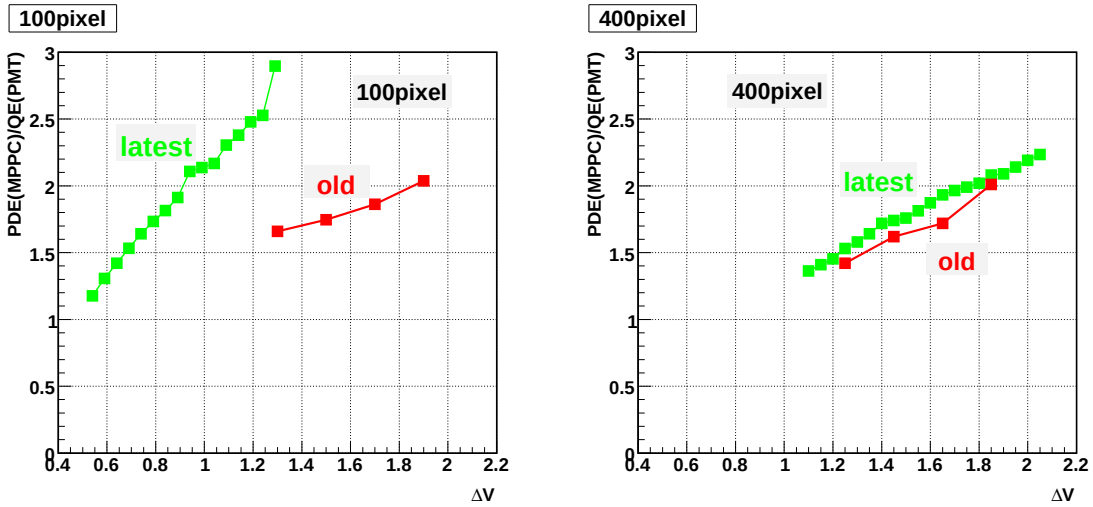

Figure A.3: Measured PDE of 100 pixel (left) and 400 pixel (right) devices as a function of ΔV. The PDE is relative value to QE of a PMT. Green points correspond to the latest sample and red points the old one. The measurement was done at 20°C.

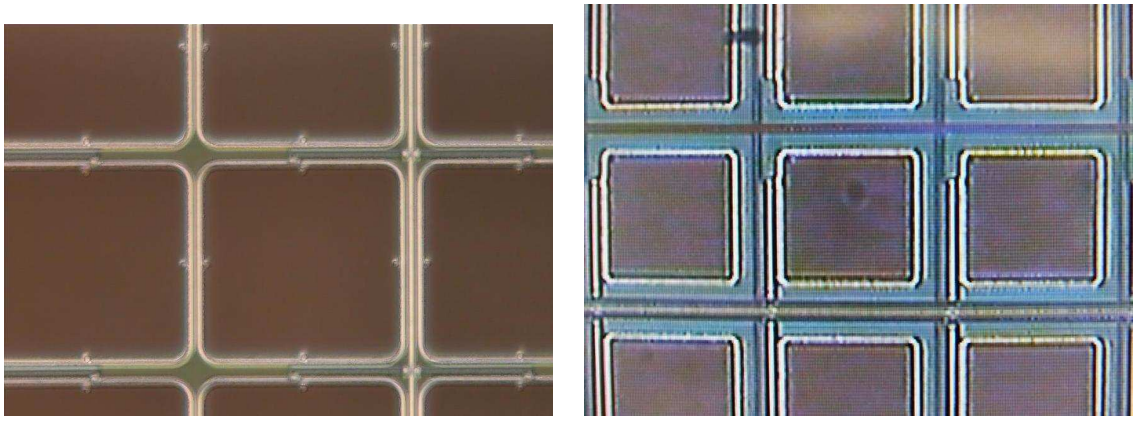

Figure A.4: Photograph of latest (left) and old (right) 100 pixel devices. The latest sample has larger geometrical efficiency than that of the old one.

A.4 Cross-talk rate

Figure A.5 shows the measured cross-talk rate of 100 pixel (left) and 400 pixel (right) devices as a function of ΔV. Green points correspond to the latest sample and red points the old one. The measured cross-talk rate of the latest sample is higher than that of the old sample. This is because that the geometrical efficiency of the latest sample is increased and the distance between neighbouring pixels become small.

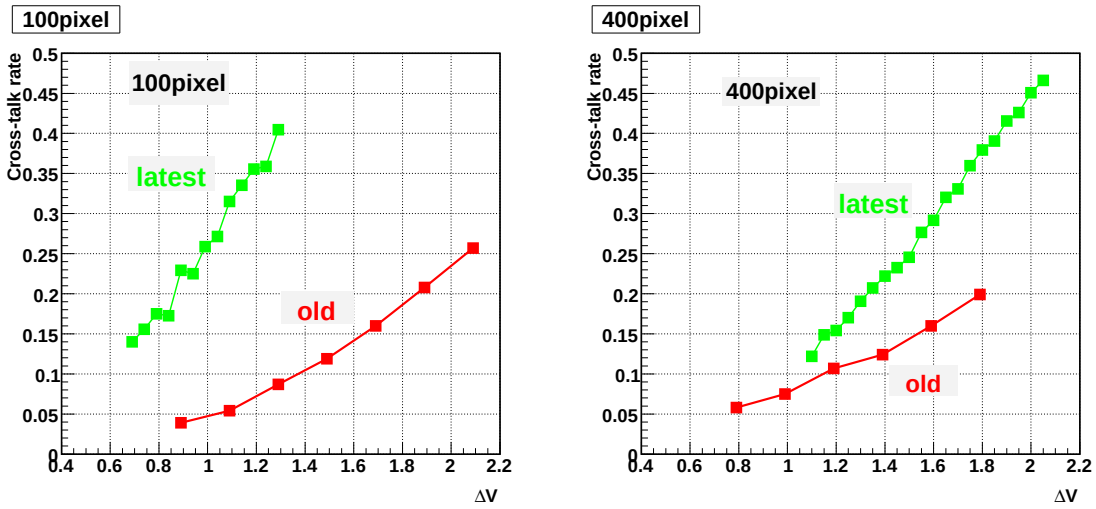

Figure A.5: Measured cross-talk rate of 100 pixel (left) and 400 pixel (right) samples as a function of ΔV. Green points correspond to the latest sample and red points the old one. The measurement was done at 20°C.

A.5 Summary

The new samples delivered in Oct. 2006 have much better points than the old ones at noise rate and PDE. However the cross-talk rate becomes higher due to the improvement of the geometrical efficiency. HPK is now working to reduce cross-talk rate for the next samples.

Appendix B

DEVICE-BY-DEVICE VARIATION OF OLD 100 PIXEL SAMPLES

In this chapter we show the device-by-device variation of three old 100 pixel samples which was delivered in Jan. 2006. The test items are gain, noise rate and PDE. The device-by-device variation is evaluated with the same method described in Chapter 4. All the measurements were done at 15°C.

B.1 Gain

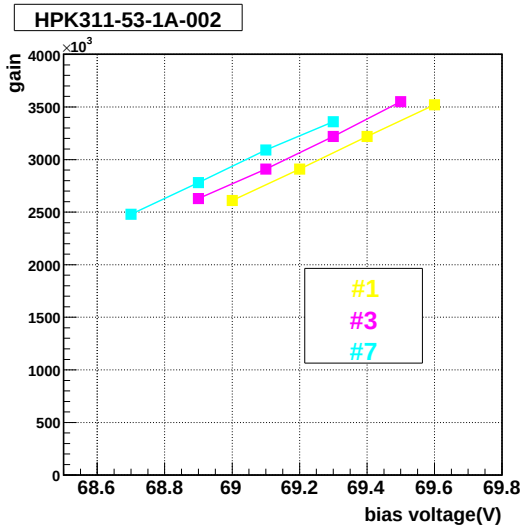

Figure B.1: Device-by-device gain variation as a function of the applied voltage. Different colors correspond to the different samples of the same type of MPPC.

Figure B.1 shows the device-by-device variation as a function of the applied voltage. Different colors correspond to the different samples of the same type of MPPC. The device-by-device gain variation at the same applied voltage is about 10%.

B.2 Noise rate

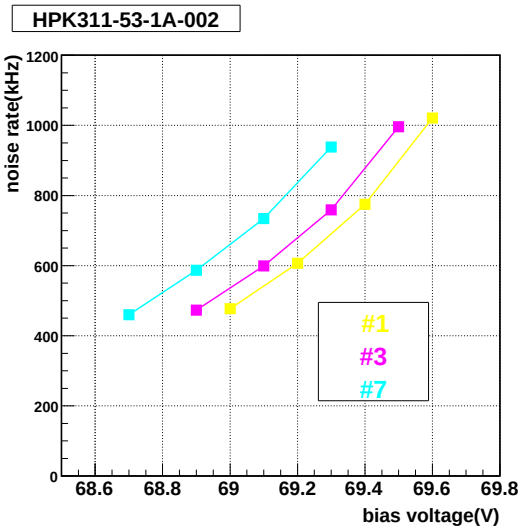

Figure B.2: Device-by-device variation of the noise rate at the 0.5 p.e. threshold as a function of the applied voltage. Different colors correspond to the different samples of the same type of MPPC.

Figure B.2 shows the device-by-device variation of the noise rate at the 0.5 p.e. threshold as a function of the applied voltage. Different colors correspond to the different samples of the same type of MPPC. The device-by-device variation at the same voltage is about 13%.

B.3 PDE

Figure B.3 shows the device-by-device variation of PDE as a function of the applied voltage. The PDE is shown as the relative value to QE of a PMT. Different colors correspond to the different samples of the same type of MPPC. The device-by-device variation at the same voltage is about 10%.

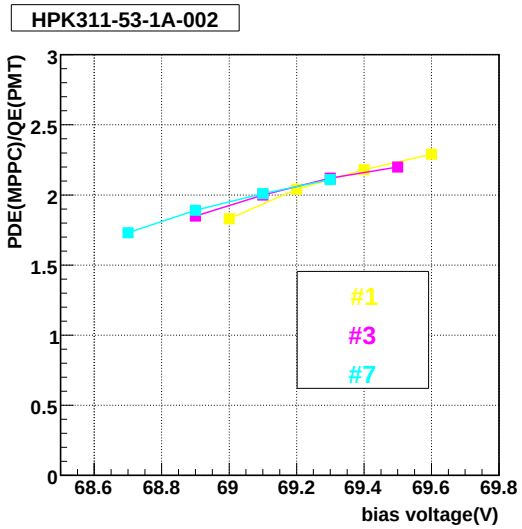

Figure B.3: Device-by-device variation of PDE at as a function of the applied voltage. Different colors correspond to the different samples of the same type of MPPC.

Appendix C

EXPECTED CURVE OF MPPC TO THE LARGE AMOUNT OF LIGHT

In this chapter we explain the derivation of Eq. 4.10 which shows the expected curve of MPPC to the large amount of light. We want to determine the number of fired pixels depending on the number of incoming photons. Let us call f(q) the number of fired pixels when q photons enter and P(event) the probability of an event. Then, f(q+1) = f(q) + P(the new incoming photon enters the active area within a pixel) × P(the pixel has not been yet fired) × P(the photon is absorbed) × P(the created photoelectrons trigger an avalanche) × P(cross-talk).

$$f(q+1) = f(q) + \epsilon_{geom} \times (1 - \frac{f(q)}{N_0}) \times \mathrm{QE} \times \epsilon_{Geiger} \times (1 + \mathrm{c}), \tag{C.1}$$

where

- N_0 : Number of pixels
- ϵ_{geom} : Fraction of the active area to the total area
- QE : Quantum efficiency of an avalanche photodiode
- ϵ_{Geiger} : Probability of triggering an avalanche
- c : Cross-talk rate.

Calculating Eq. C.1, we obtain

$$f(q) = N_0 \times (1 - (1 - \frac{\mathrm{PDE} \times (1 + \mathrm{c})}{N_0})^{q+1}), \tag{C.2}$$

where PDE = ϵ_{geom} × QE × ϵ_{Geiger}. We now have to consider the poissonian fluctuations of q around the mean value of N. The distribution around N is given by $\pi_N(q) = \mathrm{e}^{-\mathrm{N}}\frac{\mathrm{N^q}}{\mathrm{q!}}$ with q ∈ N. Then, the expected value of f(q) which is shown as N_{fired} is given by :

$$N_{fired} = \sum_q (\pi_N(q)) \times f(q) \tag{C.3}$$

$$= N_0 \times (1 - \exp(\frac{\mathrm{N} \times \mathrm{PDE} \times (1 + \mathrm{c})}{N_0}) \tag{C.4}$$

$$= N_0 \times (1 - \exp(\frac{\mathrm{x}(1 + \mathrm{c})}{N_0}), \tag{C.5}$$

where x = PDE × N, which is the number of injected photoelectrons. Thus we obtain Eq. 4.10.

Appendix D

TEST WITH AN INFRARED CAMERA

Some MPPC samples emit the noise with the large pulse height($\sim$ 10 p.e.) when the applied voltage increases. These are early samples and different from those described in this thesis. In order to study whether this large noise localizes or not, we took the picture of one of those samples by an infrared camera, with bias voltage applied. The result is shown in Fig. D.1. The applied bias voltage is 75.0 V and measured dark current is 8 μA. The large current flows in the red area of this picture. From this picture we can see the noise with the large pulse height localizes in the edge of a pixel. This is because a large electric field is made in the edge of the pixel.

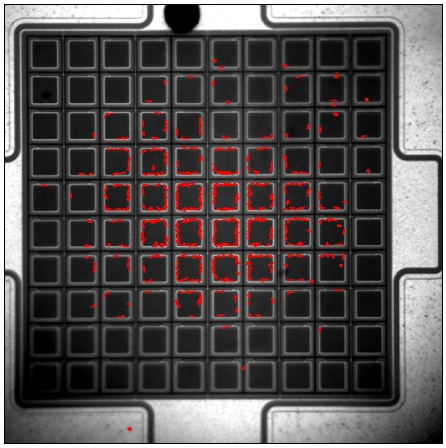

Figure D.1: Picture of the sample which emit the noise with the large pulse height taken by an infrared camera. The large current flows in the red area of this picture.

Appendix E

OPERATION OF TRIP-T

In this chapter we explain the operation of Trip-t in detail.

E.1 Control signals

We must put fifteen control signals in order to operate Trip-t. Table E.1 shows the list of the control signals.

We explain each control signal in more detail.

- PRE_RST, PRE2A_RSTB, PRE2B_RSTB : These are signals to switch on/off the preamp, opamp A and opamp B, respectively. When "PRE_RST" is low, the switch of the preamp is turned on. When "PRE2A(B)_RSTB" is high, the switch of the opamp A(B) is turned on. Usually "PRE2A_RSTA" and "PRE2B_RSTB" are set to be the invert signals of "PRE_RST".

- PIPE_CLK : At the rising and falling edges of "PIPE_CLK", the output from the front-end is sampled.

- PIPE_RST : When this is high, the contents of pipelines are reset.

- SKIPB : When this is low at the low period of "PIPE_CLK", the address of the pipeline which is specified by the programmed pipeline latency is loaded into FIFO (First In First Out[1]).

- PR1 : When this is high at the low to high transition of "PIPE_CLK", this accesses FIFO in order to get the triggered pipeline content.

- MOVEDATA : When this is high at the low to high transition of "PIPE_CLK", this removes FIFO which was loaded previously.

[1]This expression describes the behavior that what comes in first is handled first and what comes in next waits until the first is finished.

Name of control signal	Explanation
PRE_RST	Determine the reset and integrate period of the preamp
PRE2A_RSTB	Determine the reset and integrate period of the opamp A
PRE2B_RSTB	Determine the reset and integrate period of the opamp B
PIPE_CLK	Control a pipeline
PIPE_RST	Reset a pipeline
SKIPB	Load the address of a pipeline into FIFO
PR1	Trigger the pipeline readout
MOVEDATA	Remove FIFO previously loaded
PRG_RST	Reset all registers to the default values
PRG_CTRL	When high, make the programming interface active. When low, the multiplexer function is possible.
PRGIN (MUX_RSTB)	When PRG_CTRL is high, program interface. When PRG_CTRL is low, set the multiplexer on.
PRG_CLK (MUX_CLK)	When PRG_CTRL is high, the program interface clock. When PRG_CTRL is low, the multiplexer clock.
DIG_ENU	Enable lower half of the D_OUT lines (17 to 32)
DIG_ENL	Enable upper half of the D_OUT lines (1 to 16)
DIG_RSTB	Reset all discriminators

Table E.1: List of the control signals for the operation of Trip-t.

- PRG_RST : When this is high, all the registers are reset to the default values. This must be set at first when the power of Trip-t is turned on.
- PRG_CTRL : When this is high, the programming of registers is possible as shown in Fig. E.2. During the readout of Trip-t this must be set low.
- PRG_IN (MUX_RSTB) : When "PRG_CTRL" is high, this is used to program registers as shown in Fig. E.2. During the readout of Trip-t, this must be set high.
- PRG_CLK (MUX_CLK) : When "PRG_CTRL" is high, this is the clock for programming of registers, as shown in Fig. E.2. During the readout of Trip-t this is the multiplexer clock.
- DIG_ENU (DIG_ENL) : When "DIG_ENU" ("DIG_ENL") is high, D_OUT of the channel $17 \sim 32$ ($1 \sim 16$) can be seen.
- DIG_RSTB : When this is low, all discriminators are reset.

E.2 Readout principle of Trip-t

In this section we explain the readout principle of Trip-t using Figure E.1. The meaning of each control signal is explained in Table E.1.

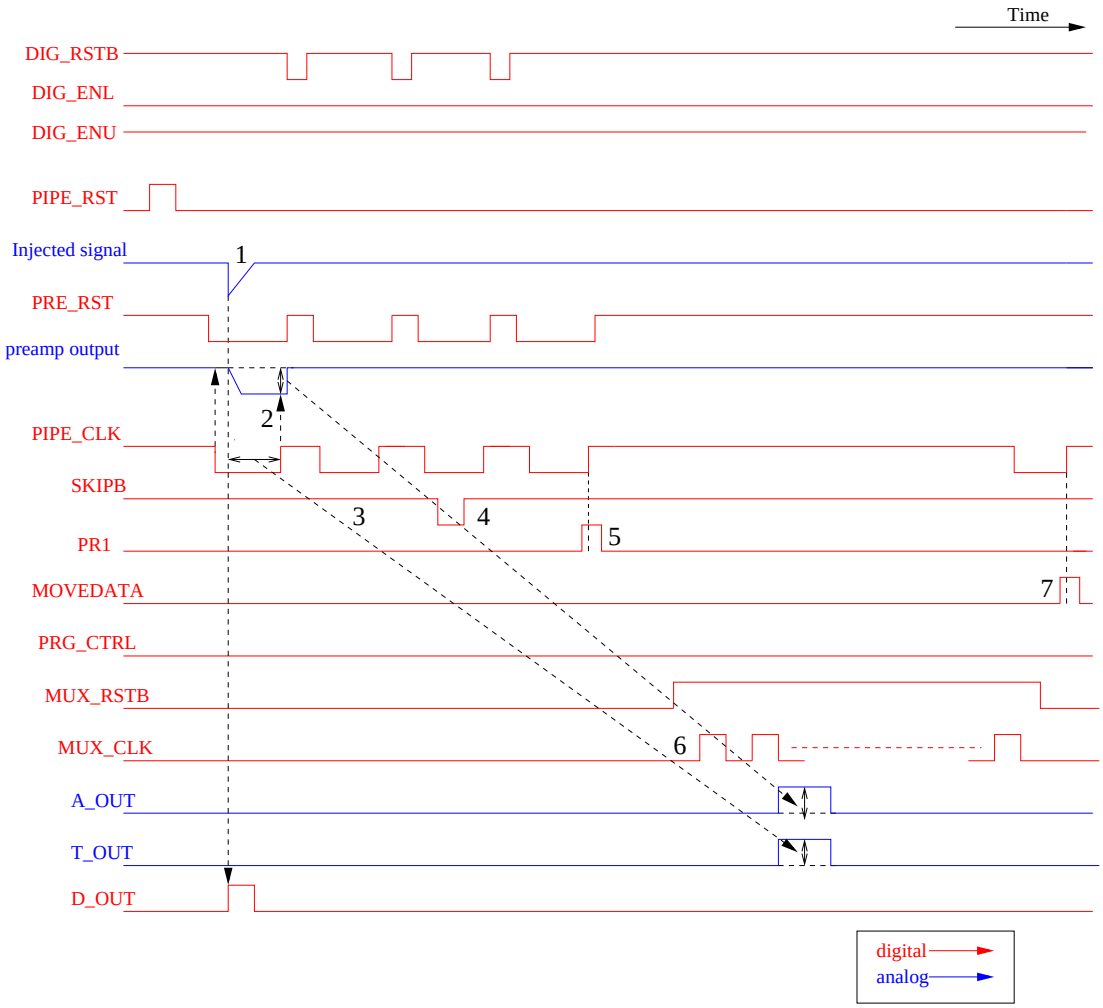

Figure E.1: Readout sequence of Trip-t. A blue line shows an analog signal, and red one shows a digital signal. "PRE2A_RSTB" and "PRE2B_RSTB" are not shown in this figure, but they are the invert signals of "PRE_RST".

1. Inject a signal during the preamp integrate period.

2. At the falling and rising edges of "PIPE_CLK", the preamp output is sampled.

3. Wait for the programmed pipeline depth to elapse (2 in this figure)

4. Send "SKIPB" when "PIPE_CLK" is low. The address of the pipeline cell where the signal is stored is loaded into FIFO.

5. Send "PR1" at the low to high transition of "PIPE_CLK" in order to access the FIFO.

6. Run the output multiplexer.

7. Send "MOVEDATA" at the low to high transition of "PIPE_CLK". The previously loaded FIFO is removed.

Above is the rough flow of the readout sequence. We set the preamp integrate period to be 300 ns and the reset period 50 ns. In order to read out the signal stored in the specific pipeline cell, we must set the pipeline latency before the readout sequence. This is done by programming the register 11, which is shown in Table E.2. The frequency of "MUX_CLK" must be from $\sim$ 100 Hz to $\sim$ 10 MHz.

E.3 Register

The register is a digital circuit that holds data using circuit elements such as flip-flops. It records the pattern of several input pulses (e.g., the bits of a binary word) and stores this pattern in a buffer where it can be read by an external device. In Trip-t the recorded pattern is expressed as voltage or current for the preamp, opamp and comparator. Table E.2 shows the list of register names, their default values and explanations. The registers except for PIPEDELAY and GAIN are set to be default for the test of the basic performance of Trip-t, while PIPEDELAY is set to be six and the various values are tested for GAIN.

Figure E.2 shows the programming sequence of a register. The chip ID is always 01010. The register number is written MSB[2] first, but the register value is written LSB[3] first. The possible instructions are shown in Table E.3. By the read instruction we can see the currently set value of the register from the PRG_OUT line on the board. Figure. E.3 shows the default value of the register 11 seen from the PRG_OUT line.

The registers colored red in Table E.2 are important ones to operate Trip-t correctly.

- IBP : Preamp doesn't work correctly if this is set too small.

- IFF : Width of the preamp output becomes small and "PIPE_CLK" cannot sample the voltage in proportional to the injected charge if this is set too large.

[2]Most Significant Bit
[3]Least Significant Bit

Register	Name	Default value	Explanation
1	IBP	130	Preamp drive current
2	IBBNFoll	120	Preamp feedback control
3	IFF	0	Preamp feedback control
4	IBPIFF1REF	160	Preamp reset strength
5	IBOPAMP	138	Opamp drive current
6	IB_T	64	Time circuit current source
7	IFFP2	0	Opamp feedback control
8	IBCOMP	87	Comparator drive current
9	V_REF	200	Ref voltage for opamps A and B
10	V_TH	0	Ref voltage for comparator
11[5:0]	PIPEDELAY	31	Pipeline depth
11[9:6]	GAIN	1110	Gain of preamp and opamp A
12	IRWSEL	238	Drive current for pipeline read/write
13	LUCKB	0	Do not use
14	INJECT	–	Which channels to test-pulse

Table E.2: List of the registers. The default value means the values after we put "PRG_RST". All registers except for the register 11 and 14 are 8 bits long, but the register 11 is 10 bits long and the register 14 is 34 bits long. In the register 11, bit 9 is the switch of the preamp gain (1 is low gain and 0 is high gain). Bits 8:6 are the opamp gain with 111 being the highest gain and 000 being the lowest gain. Bits 5:0 set the depth of pipeline. We cannot know the default value of the register 14.

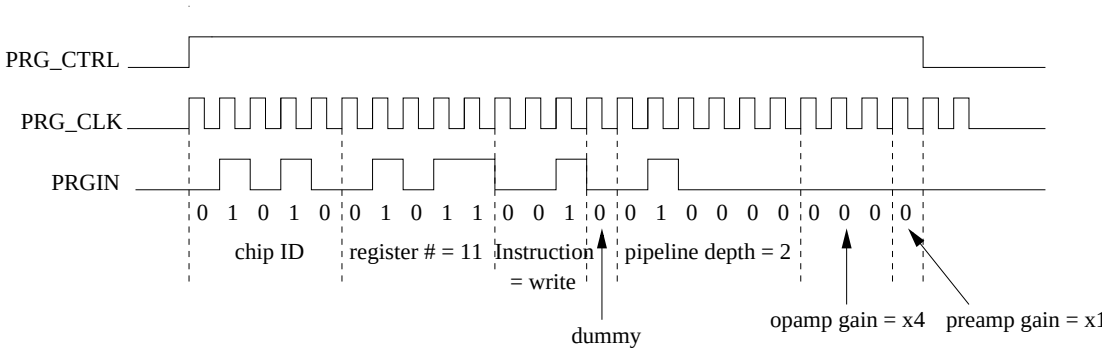

Figure E.2: Programming sequence of a register. In this figure we set the depth of pipeline to be 010000 (2 in binary digit system) and the gain of 0000 (×4, ×1).

- IBOPAMP : Opamps do not work correctly if this is set too small.
- PIPEDELAY : This must be set before running the readout sequence.

Instruction	Value	Explanation
Read	100	read the currently set value of the register from PRG_OUT
Write	001	write a value to the register
Set	010	set 255 to all registers
Reset	101	set 0 to all registers
Default	110	set the default values to all registers

Table E.3: List of the instructions for programming a register.

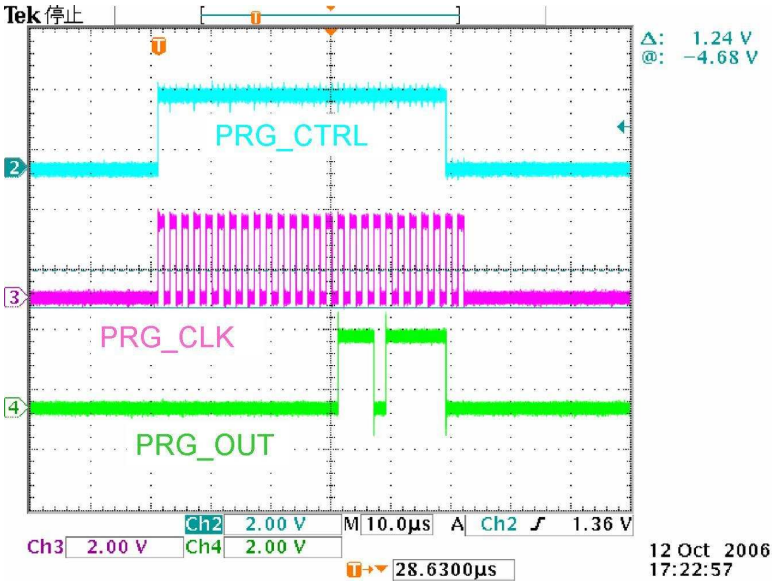

Figure E.3: Default value of the register 11 seen from the PRG_OUT line. A sky blue line is "PRG_CTRL", a pink line is "PRG_CLK" and a green line is PRG_OUT. Since we see the register value with MSB first on PRG_OUT, we read that PIPE_DELAY is 111110 (31 in binary digit system) and the gain is 1110 (×1, ×4).

Appendix F

READOUT OF MPPC WITH VA CHIP

As we have described in Chapter 8, the VA chip was used in the K2K SciBar detector to serialize 64 channel analog signals from a MAPMT. We report the study of the readout of MPPC with the VA chip in this chapter.

F.1 VA chip

The VA chip is an ASIC (Application Specific Integrated Circuit) which is constructed by CMOS[1] circuit. It has a charge sensitive preamplifier, a slow shaper and a sample&hold circuit for each input. The injected charge to each input is finally serialized to one channel by a multiplexer. The ancestor of VA is AMPLEX chip and Viking chip which were developed for the silicon detector at CERN (European Organization for Nuclear Research). The function of VA is similar to that of Trip-t, but there are following differences between VA and Trip-t.

1. VA does not have an analog pipeline.
2. VA itself cannot issue discriminated outputs.
3. Gain of VA cannot be changed.

In SciBar the VA chip is packaged into "VA32_HDR11+TA32CG" with the TA chip which has a fast triggering function. This VA/TA package has 32 inputs, and two packages are put on a Front-End Board (FEB). The photograph of the FEB is shown in Fig. F.1. Using the FEB we read out 64 channel analog signals from one MAPMT. The specification of VA is summarized in Table F.1.

[1]Complementary-symmetry Metal-Oxide-Semiconductor. The words "complementary-symmetry" refer to the fact that the typical digital design style with CMOS uses complementary and symmetry pairs of p-type and n-type MOSFETs for logic functions.

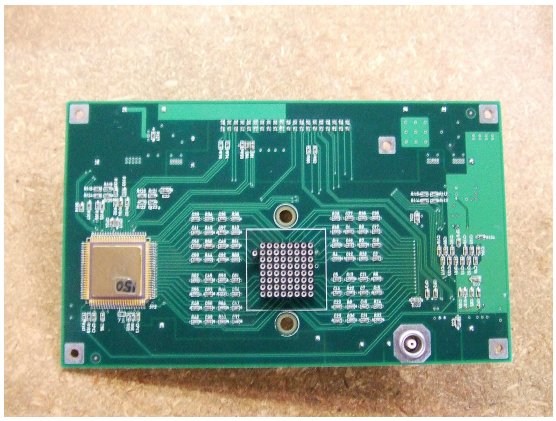

Figure F.1: Photograph of the Front-End Board (FEB). Two VA/TA packages are mounted on the FEB.

Process	1.2 μm N-well CMOS, double-poly, double-metal
Power supplies	$V_{dd} = +2.5$ V, $V_{ss} = -2.5$ V
Gain	$\sim$ 5.8 mV/pC
Dynamic range	-35 pC $\sim +25$ pC
Power consumption	2.3 mW per channel
Size	6.18 mm $\times$ 4.51 mm

Table F.1: Specification of VA.

The schematic of one channel in VA is shown in Fig. F.2. The injected analog signal is amplified by the preamplifier. The feedback resistor of the preamplifier is changed by the bias parameter "pre_bias". The output from the preamplifier is shaped with ~ 1 μs peaking time through the shaper-amplifier. The peaking time is changed by the bias parameters "Vfs" and "sha_bias". The peaking voltage of the output from the shaper-amplifier is held by the sample&hold circuit. Next we show the schematic of the serialization of 32 input signals in Fig. F.3. The 32 channel analog signals are serialized to one channel by the analog multiplexer and become the differential outputs, outp and outm.

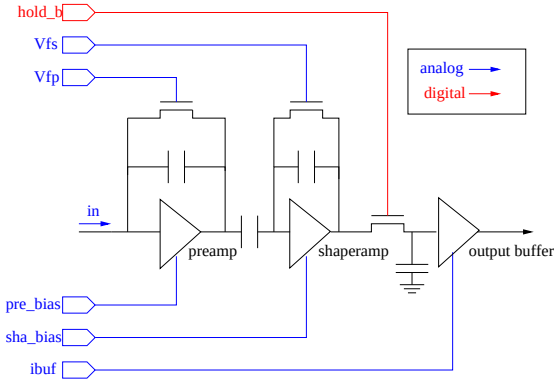

Figure F.2: Schematic of one channel in VA. A blue line shows an analog signal and a red line shows a digital signal. There are a charge sensitive preamplifier, a slow shaper and a sample&hold circuit for each channel.

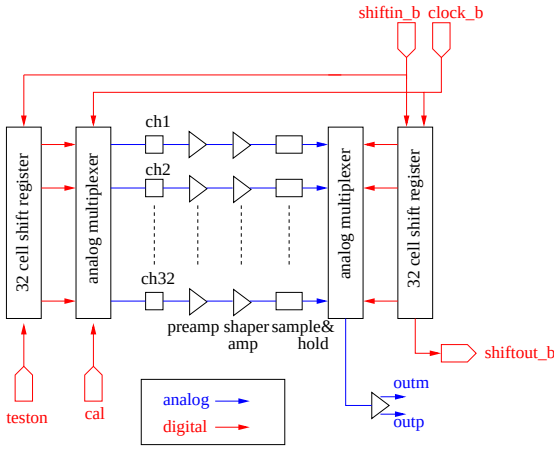

Figure F.3: Schematic of the serialization of 32 input signals. A blue line shows an analog signal and red line shows a digital signal. The outputs from each channel are serialized to one channel by an analog multiplexer.

F.2 Readout principle of VA chip

In this section we explain the readout principle of the VA chip. Table F.2 shows the list of the control signals of VA and Fig. F.4 shows the timing diagram of the control signals. The readout sequence is the following;

1. Charge injection.
2. Output from the shaper-amplifier is held at the falling edge of "hold_b".
3. Send "shift_in_b" and start the readout sequence.
4. Send the multiplexer clock. The held voltages at the sample&hold circuit are serialized at the falling edges of the multiplexer clock.
5. "Shift_out_b" is issued.

The logic circuit of VA is initialized by the external "dreset" signal.

Name of control signal	Explanation
hold_b	Hold signal for the sample&hold circuit
dreset	Reset signal for the VA digital circuit
shift_in_b	Start signal of the readout of VA
clock_b	Multiplexer clock
shift_out_b	Stop signal of the readout of VA
test_on	Signal for the change to the test injection line
cal	Test injection line

Table F.2: List of the control signals for the operation of VA.

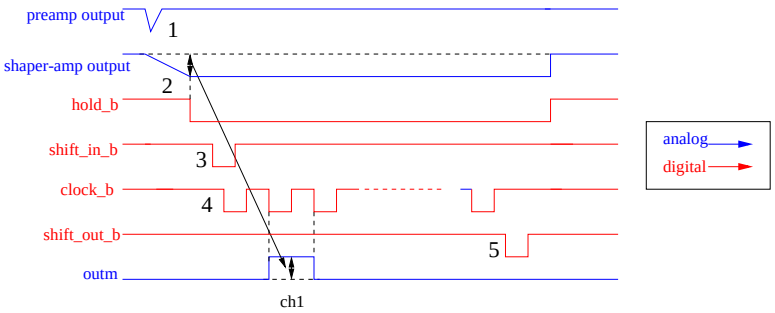

Figure F.4: Timing sequence of VA. A red line shows a digital signal and a blue line shows a analog signal. The charge is injected to the channel 1.

F.3 Readout of MPPC with VA

In this section we show the readout of MPPC with the VA chip. The serialized analog outputs from VA are sent to the DAQ board which is described in Chapter 8 through a 4 m flat cable and digitized by the flash ADC on the DAQ board. The control signals for VA are also provided by the DAQ board. We connect MPPC to one channel of VA via an AC coupling with a 100 pF capacitor and a 100 kΩ resistor and check if we can observe photopeaks of MPPC. The setup schematic is shown in Fig. F.5. The triggers to LED and DAQ board are both issued by a clock generator. Figure F.6 shows the ADC distribution of a 100 pixel device, illuminating MPPC by LED with low intensity. The measured noise rate at the 0.5 p.e. threshold is 240 kHz and the temperature is 20°C. From this figure we have found

$$\begin{aligned} M_{1p.e.} &= 2039 \\ M_{ped} &= 2013 \\ \sigma_{ped} &= 13.6, \end{aligned}$$

where $M_{1p.e.}$ is the mean ADC counts for the 1 p.e. peak, M_{ped} is the mean ADC counts for the pedestal peak and σ_{ped} is the ADC counts for the sigma of the pedestal peak. From these results the MPPC gain measured with VA is found to be about 2.7×10^6 using the VA gain of 67 counts/pC. This is consistent with the gain measured with a CAMAC charge sensitive ADC.

The signal-to-noise ratio is 1.7 while it is 60 in the case of the readout with Trip-t. This is supposed to be due to pileups of the MPPC noise. Figure F.7 shows the output from MPPC through the shaper-amplifier without external light. We can see many pileups of the MPPC noise. In VA, the preamplifier is always active and the MPPC noise which has ~ 1 μs peaking time through the shaper-amplifier piles up easily when the noise rate becomes high. Because an excellent photon counting capability is one of the attractive features of MPPC, we conclude that it is difficult to use the VA chip for the readout MPPC.

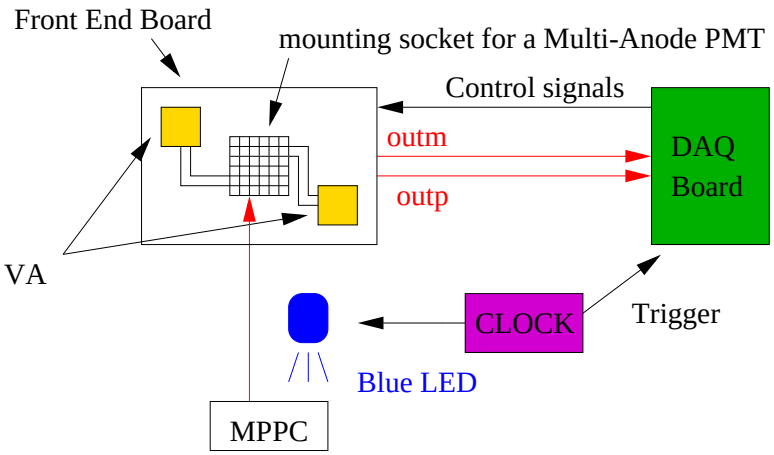

Figure F.5: Setup schematic for the readout of MPPC with VA. MPPC is illuminated by a blue LED. The outputs from VA are sent to the DAQ board and digitized by the flash ADC. The control signals for VA are also provided by the DAQ board.

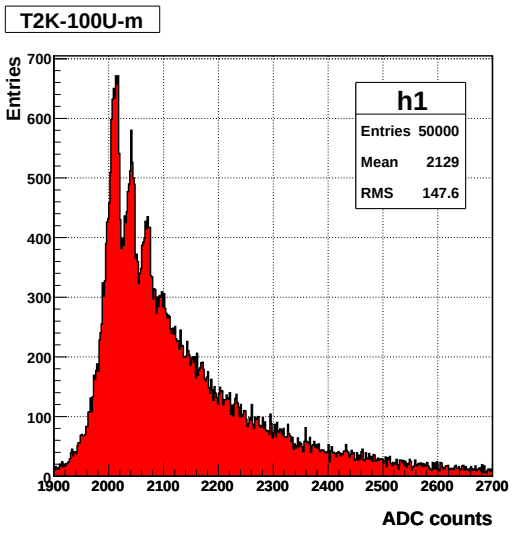

Figure F.6: ADC distribution of a latest 100 pixel device taken by DAQ board. The measured gain is 2.7×10^6 and measured noise rate at the 0.5 p.e. threshold is 240 kHz.

Figure F.7: Output of MPPC through the shaper-amplifier of VA without external light. A pink line shows the MPPC signal and a green line shows "hold_b". We can see many pileups of the MPPC noise.

Bibliography

[1] Y. Ashie et al. [Super-Kamiokande Collaboration], "Evidence for an oscillatory signature in atmospheric neutrino oscillation," Phys. Rev. Lett. 93, 101801 (2004).

[2] M. H. Ahn et al. [K2K Collaboration], "Measurement of Neutrino Oscillation by the K2K Experiment," Phys. Rev. D. 74, 072003 (2006).

[3] D. G. Michael et al. [MINOS Collaboration], "Observation of Muon Neutrino Disappearance with the MINOS Detectors in the NUMI Neutrino Beam," Phys. Rev. Lett. 97, 191801 (2006).

[4] J. Hosaka et al. [Super-Kamiokande Collaboration], "Solar neutrino measurements in Super-Kamiokande-I," Phys. Rev. D. 74, 032002 (2006).

[5] S. N. Ahmed et al. [SNO Collaboration], " Measurement of the total active B-8 solar neutrino flux at the Sudbury Neutrino Observatory with enhanced neutral current sensitivity," Phys. Rev. Lett. 92, 181301 (2004).

[6] T. Araki et al. [KamLAND Collaboration], "Measurement of neutrino oscillation with KamLAND: Evidence of Spectral distortion," Phys. Rev. Lett. 94, 081801 (2005).

[7] M. Apollonio et al. "Search for neutrino oscillations on a long base-line at the CHOOZ nuclear power station," Eur. Phys. J. C 27, 331 (2003).

[8] Y. Itow et al., "The JHF-Kamioka neutrino project," arXiv:hep-ex/0106019, http://neutrino.kek.jp/jhfnu/.

[9] K. Matsuoka, Master's thesis, Kyoto University (2006).

[10] Y. Kurimoto, Master's thesis, Kyoto University (2005).

[11] B. Dolgoshein et al., "Status report on silicon photomultiplier development and its applications," Nucl. Instrum. Meth. A 563, 368 (2006).

[12] GLD Concept Study Group, "GLD Detector Outline Document," available online from http://ilcphys.kek.jp/gld/documents/dod/glddod/pdf/.

[13] N. Otte et al., "The SiPM -A new Photon Detector for PET," Nucl. Phys. B (Proc Suppl.) 150, 417 (2006).

[14] A. L. Lacaita et al., "On the Bremsstrahlung Origin of Hot-Carrier-Induced Photons in Silicon Devices," IEEE Transactions on electron devices, vol 40, n°, 577 (1993).

[15] H. Kressel, "Semiconductor devices for optical communication," Topics in applied physics vol.39, Springer (1982).

[16] O. Mineev et al., "Scintillator counters with multi-pixel avalanche photodiode readout for the ND280 detector of the T2K experiment," arXiv:physics/0606037/.

[17] Report at the KEK Detector Technology Project meeting.

[18] KEK Detector Technology Project, http://rd.kek.jp/.

[19] T. Nobuhara, Master's thesis, Kyoto University (2005).

[20] K. Nitta et al., "The K2K SciBar detector," Nucl. Instrum. Meth. A 535, 147 (2004).

[21] J. Estrada et al., "D0 note" 4009 (2002).

[22] The MINERνA Collaboration, "The MINERνA Technical Design Report," available online from http://minerva-docdb.fnal.gov/0007/000700/028/TDR_v1.3.pdf/.

[23] S. Yamamoto, Master's thesis, Kyoto University (2002).

[24] The VA1' Specifications v09.2, Ideas ASA, http://www.ideas.no/.

List of Figures

List of Tables